2018

Compact Antenna with Artificial Magnetic Conductor for Noninvasive Continuous Blood Glucose Monitoring

Meenakshy Iyer
mai2407@rit.edu

Compact Antenna with Artificial Magnetic Conductor for Noninvasive Continuous Blood Glucose Monitoring

By

Meenakshy Iyer

A Thesis Submitted in Partial Fulfillment of the
Requirements of the Degree of

MASTER OF SCIENCE
in
Electrical Engineering

Approved by:

Professor: _____
(Dr. Jayanti Venkataraman - Advisor)

Professor: _____
(Dr. Gill Tsouri - Committee Member)

Professor: _____
(Dr. Panos P. Markopoulos - Committee Member)

Professor: _____
(Dr. Sohail A. Dianat – Department Head)

Department of Electrical and Microelectronic Engineering
Kate Gleason College of Engineering (KGCOE)
Rochester Institute of Technology
Rochester, New York

To my mother, Raji

Acknowledgements

Foremost, I would like to express my sincere and heartfelt gratitude to my adviser Dr. Jayanti Venkataraman, for her continuous support throughout my time at RIT, for her patience, motivation enthusiasm, and immense knowledge and experience. Her hard work and dedication has set an example of excellence as a researcher, mentor, instructor and a role model.

I am also very thankful to the committee members Dr. Gill Tsouri and Dr. Panos Markopoulos for their insightful comments, feedbacks and encouragement. I would also like to extend my gratitude towards the staff of Electrical Engineering, Ken, Jim, Patty, Florence, for all their hard work and constant support.

I thank my fellow lab mates at EM lab: Rounak, Pratheik, Nic, Romiou, and Brian for the stimulating discussions, for the sleepless nights working together before deadlines, and for all the fun we have had in the 2 years. Also I thank my dear friends who have been there for me from my first day at RIT- Aadeesh, Raghu, Vignesh, Vishaal Ananth, Yeshwanth, Ramesh, Jui, and Varun for all the amazing time and memories that is etched in my heart forever.

Last but not the least, I would like to thank my mother, for her tremendous support, love and blessings to achieve what I am today. I owe all my success and accomplishments to her. My sister, Konzee, for being the stress buster and make me laugh whenever possible. I am very thankful to Saurabh for constantly being around, understanding me, guiding me to the right path, and imparting a positive environment throughout.

Awards

First Place: KGCOE 3-minute MS Thesis Presentation, March 23, 2018

Second Place: RIT 3-minute MS Thesis Presentation, April 18, 2018

Abstract

A non-invasive technique for real-time continuous monitoring of blood glucose has been under development by Venkatarman's research group in the ETA lab at RIT [16]-[18]. The methodology involves placing an antenna on the arm and monitoring changes in the resonant frequency, which is attributed to changes in the blood glucose level. This is because the blood's permittivity depends on the glucose levels, and in turn, affects the antenna's resonant frequency. In order to correlate the antenna's resonant frequency shift with the real-time blood glucose change, glucose estimation was also modeled using the antenna's input impedance. The antennas designed could successfully track the rise and fall of blood glucose using the glucose estimation model for both diabetic and non-diabetic patients.

However, the antennas being used in this research are too large in size and not flexible. Additionally, the antenna's radiation pattern was omnidirectional as it is a monopole antenna where the radiation is into the arm as well as away from the arm (back radiation). As a result, during the test procedure, the arm must be in a steady position throughout the time of the resonant frequency measurement. While it worked very well to prove the feasibility of continuous glucose monitoring, a better antenna is required for the next phase of research that involves clinical testing in a hospital environment.

My goal in this thesis is to take the research further by designing antennas that are unidirectional, flexible and small in size. The unidirectional property can be achieved by using PEC (Perfect Electric Conductors) or PMC (Perfect Magnetic Conductors) over the antenna that can suppress the back radiation. Unlike the presence of infinite electric charges on an electric conductor, magnetic charges don't exist. Therefore magnetic conductors are modeled artificially to achieve

magnetic properties commonly known as Artificial Magnetic Conductors (AMC). The antenna used in this thesis is a monopole antenna with AMC as a ground plane. The advantage of using AMC over a perfect metal conductor as a ground plane to the antenna is that the AMC reflects the incident wave in phase and not out of phase like a regular metal conductor. Moreover, AMC layers not only suppresses the back radiation but also enhances the gain of the antenna into the arm. Using the AMC layer as the ground plane has also helped in miniaturizing the antenna. The different artificial magnetic conductors designed in this thesis are Rectangular Patch, Rectangular Ring, I-shaped, and Jerusalem Cross. The antennas were fabricated and tested in the unlicensed ISM band (2.4GHz – 2.5GHz) and are within the SAR standards laid out by FCC.

The fabricated antenna was strapped to the arm and measurements of resonant frequency similar to those made previously were conducted with respect to time [16]-[18]. Two types of measurements were compared, that is, when the arm was held steady and when the arm had some movement. No significant change or fluctuations in the resonant frequency was observed with arm movement. Whereas the same type of measurements conducted on the monopole antenna in [18] showed significant fluctuations in the resonant frequency with arm movement. This experiment shows the significant advantage of the antenna with AMC layer as compared to the monopole antenna. Also demonstrated in the present work, is the ability of the designed antenna in tracking the increase and decrease of glucose level with changes in the resonant frequency, similar to [16]. This has been demonstrated with two non-diabetic subjects. Further, no back radiation was noted, when a hand above the setup is moved. Additionally, the effect of creeping waves was negligible. The antenna designed in this work will conform well to clinical studies of the ETA Lab research.

Table of Contents

List of Figures

List of Tables

List of Abbreviations and Symbols

ADA	American Diabetes Association
AMC	Artificial Magnetic Conductors
ANT	Antenna
CGM	Continuous Glucose Monitoring
CPW	Co-planar Waveguide
DM	Diabetes Mellitus
EBC	Exhaled breath condensate
EBG	Electromagnetic Band-Gap
ETA	Electromagnetic Theory and Applications Lab
FCC	Federal Communications Commission
FDA	Food and Drug Administration
GND	Ground
HFSS	High Frequency Structure Simulator
ICNIRP	International Commission of Non Ionization Radiation Protection
IEEE	Institute of Electrical and Electronics Engineers
IMDs	Implantable Medical Devices
ISM	Industrial, Scientific and Medical
KGCOE	Kate Gleason College of Engineering
MICS	Medical Implant Communication Service
NIR	Near-infrared
PCB	Printed Circuit Board
PEC	Perfect Electric Conductor
PIFA	Planar Inverted F antenna
PMC	Perfect Magnetic Conductor
PNA	Programmable Network Analyzer
RF	Radio Frequency

RFIC	Radio Frequency Integrated Circuit
RIT	Rochester Institute of Technology
SAR	Specific Absorption Rate
SMBG	Self-monitoring blood glucose
UWB	Ultra-Wide Band
WLAN	Wide local area network
σ	Conductivity
ω	Angular Frequency
β	Phase constant
λ	Wavelength
c	Speed of Light
γ	Propagation constant
ϵ''	Imaginary part of Complex Permittivity
ϵ'	Real part of Complex Permittivity
ϵ_r	Relative permittivity
μ	Permeability
δ_p	Penetration depth
ϵ_{eff}	Effective relative permittivity
ϵ_0	Permittivity of Free Space
$\bar{E}$	Electric Field
$\bar{H}$	Magnetic Field
α	Attenuation constant
ϵ	Permittivity
ρ	Tissue density [kg/m^3]

1. Introduction

1.1. Diabetes and need for CGM

Diabetes was first documented by the Egyptians and is characterized by weight loss and polyuria. However, it was the Greek physician Aertaeus who coined the term diabetes mellitus (DM). In Greek, diabetes means "to pass through" and mellitus is the Latin word for honey (referring to sweetness). Diabetes is an important cause of prolonged ill health and premature mortality, and claims more lives per year than HIV-AIDS with nearly 1 death every 10 seconds [1].

All types of diabetes mellitus have something in common. Normally, our body breaks down the sugars and carbohydrates we eat into special sugar called Glucose. Glucose fuels the cells in our body. On the other hand, the cells need insulin, a hormone, in our blood stream in order to take in glucose and use it for energy. With diabetes mellitus, either our body does not produce enough insulin, or it cannot use the insulin that it produces, or a combination of both. Since the cells cannot take in the glucose, it builds up in one's blood. High levels of blood glucose can damage tiny blood vessels in our kidneys, heart, eyes or nervous system. Therefore, if diabetes is left untreated, it will eventually lead to heart disease, stroke, kidney dysfunction, blindness and nerve damage [2],[3].

Normally, for healthy adults, the blood glucose level lies between 80-120mg/dl and should be less than 140mg/dl after a meal. However, patients with diabetes experience much higher blood glucose levels if not controlled. Glucose level can be measured using conventional monitoring systems for home use which require a drop of blood to be applied onto a test strip which is than inserted into the measurement device for a reading [4]. There are certain things that everyone who has diabetes,

whether type 1 or type 2, needs to do to be healthy. They need to have a meal (eating) plan**.** They need to pay attention to how much physical activity they engage in, because physical activity can help the body use insulin better so it can convert glucose into energy for cells. Everyone with type 1 diabetes, and some people with type 2 diabetes, also need to take insulin injections**.** Some people with type 2 diabetes take pills called "oral agents" which help their bodies produce more insulin and/or use the insulin it is producing better. Some people with type 2 diabetes can manage their disease without medication by appropriate meal planning and adequate physical activity [5].

Most of the diabetic patients get routine checkup at least once every six months by a diabetes specialist (an endocrinologist or a diabetologist). He or she should also be seen periodically by other members of a diabetes treatment team, including a diabetes nurse educator, and a dietitian who will help develop a meal plan for the individual. Ideally, one should also see an exercise physiologist for help in developing a physical activity plan, and, perhaps, a social worker, psychologist or other mental health professional for help with the stresses and challenges of living with a chronic disease. Everyone who has diabetes should have regular eye exams (once a year) by an ophthalmologist to make sure that any eye problems associated with diabetes are caught early and treated before they become serious [5].

Wearable biosensors are smart electronic devices that can be worn on the body as implants or accessories. Recent advances in microelectronics, telecommunications, and sensor manufacturing have opened up possibilities for using wearable biosensors to continuously monitor an individual’s body status without interrupting or limiting the user’s motions [6]–[13]. However, while many commercially available wearable electronics can track users’ physical activities, devices that can provide an insightful view of user’s health status at the molecular level need more development.

On the other hand, although some commercial hand-held analyzers enable glucose or lactate detection, most of these devices rely on blood samples [14]. Neither finger-prick nor invasive sensors (such as a needle embedded under the skin) are desired for wearable biomedical applications.

The main purpose of developing a non-invasive glucose measuring device is to make strict glycemic control more achievable for all diabetic patients. Assisting patients to properly dose their insulin or otherwise maintain their blood glucose levels will significantly lower the medical complication rate associated with diabetes and reduce the overall healthcare costs rooted in diabetes. The top three reasons cited from a patient survey monitor blood glucose less frequently than recommended: testing my blood sugar as often as recommended would be expensive, painful, and unpleasant [15]. Hence this thesis focuses on designing microstrip antennas to help monitor blood glucose that will enhance the ongoing research [16]–[18].

1.2. Blood Glucose Monitoring Methods

1.2.1. Single reading self-monitoring blood glucose devices (minimally invasive)

Figure 1-1 Conventional SMBG device

Self-monitoring blood glucose (SMBG) device is the glucose meter that is most widely accepted and universally used and it is the standard of SMBG for the American Diabetes Association (ADA) [19]. The glucose meter has undergone much improvement since its release in 1970 including miniaturization, disposable sensors, smaller sampling volume, and shorter measuring time [20], [21]. Despite how far these devices have come, device accuracy remains an issue [22] and there is a large disconnect

between commercial product and academic research [23]. Glucose meters typically operate via blood sampling. Patients sample capillary blood by using a lancet to prick their fingers and then apply a drop of blood to the sensor of the device [19]. The two primary methods of glucose quantification in most SMBG devices use electrochemistry or photometry to measure the oxidation of glucose through either glucose dehydrogenase or glucose oxidase [24]. Typical patients may have to measure their blood glucose levels three or more times a day, though blood glucose sample frequency will vary between individuals [25].

1.2.2. Continuous blood glucose monitoring (minimally invasive)

Continuous glucose monitoring (CGM), where a device monitors fluctuations of blood glucose in near real time, may be an achievable method of alleviating high glucose measurement frequency of some patients. Unfortunately, CGM systems are unavoidably at least minimally invasive. They range from implantable devices, which are fully invasive, to trans-dermal, which can be minimally invasive [22]. Additionally, CGM devices cannot entirely rid the patient of SMBG finger pricks as most of these devices will intermittently require calibration with a SMBG device, such as a glucose meter [26]. There are a number of CGM devices commercially available, and there is significant research in the field of a closed loop CGM device [26]. A closed loop CGM device involves combining the device with an insulin pump and a controller, allowing the device to dose insulin as needed if the blood glucose level becomes elevated. The system would effectively allow the patient strict glycemic control with little device interaction. Current limitations of CGM devices include accuracy, durability, reliability, and lag time [26]. The perfection of such a device would in essence be the creation of an artificial pancreas, and this is the focus of much diabetic research [27]. Much progress has been made on the path to an artificial pancreas on the CGM,

insulin pump, and controller fronts, but it is still far from being commercially available [28]. However, when it does become commercially available, the closed loop system has the possibility to take out patient error and negligence out of glycemic control.

1.2.3. Measurement through exhaled breath (Non-invasive)

The exhaled breath condensate (EBC) sampling and analysis has been performed since the 1980s [29] and it has since expanded into a thriving and promising non-invasive testing method [30]–[32] and minimal perceived inconvenience to the patient. Breath acetone, for example, has been used to in diabetes diagnostics and has been investigated as a biomarker for glucose metabolism [33], [34]. Specifically, this work investigates glucose in EBC. Glucose has been detected in EBC samples [35]. EBC is not practical for continuous real time monitoring, as the device will cause discomfort to the person using it throughout the day.

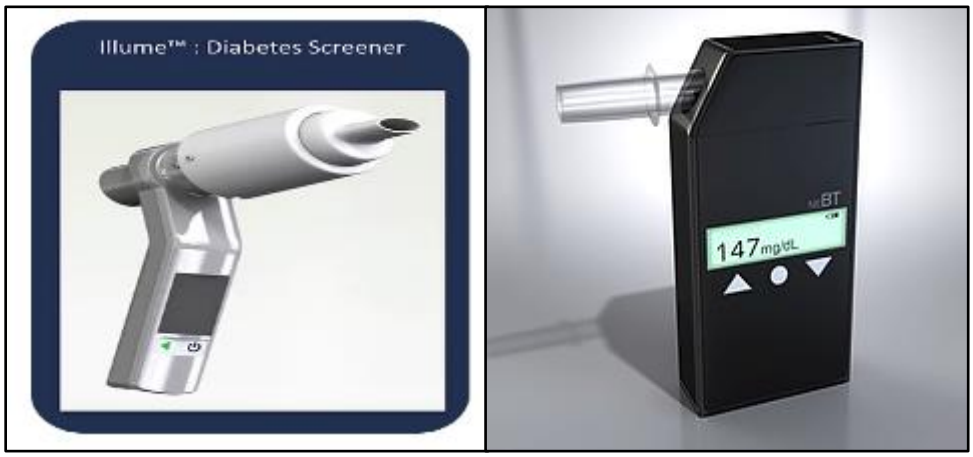

Figure 1-2 Illume™ Diabetes Screener and GLUCAIR™ Diabetes Monitor manufactured by [36] are based on glucose measurement through exhaled breath.

1.2.4. Measurements through body fluids (Non-invasive)

Although blood is by far the most understood sample for diagnosis, other biological fluids such as sweat, tears, and saliva also contain tremendous biochemical analysts that can provide valuable

information and are more readily accessible compared to blood [37], [38]. Recent studies suggest a diagnosis system based on the glucose concentration in body fluids to estimate blood glucose levels [39]–[41] However, many challenges still exist for the accurate glucose sensing in body fluids [42], [43]. For example, the glucose levels in body fluids are much lower than that in blood [44]. The sensing results can be affected by ambient temperature changes, mechanical deformation caused by body motion, and the sample collection procedure.

1.2.5. Transdermal glucose extraction (Non-invasive)

A well-known technology for noninvasive glucose monitoring using transdermal glucose extraction is reverse iontophoresis. A low electric current applied on the skin 4 between cathode and anode allows charged and uncharged molecular species to permeate across the skin [45]. Due to the convection flow, glucose is extracted from interstitial fluid and collected at cathode [46] and the amount of glucose is analyzed. The Cygnus Glucowatch™ was the first device based on this technology that was approved by the FDA [45]. However, it was withdrawn from the market for the following reasons: low sensitivity, poor accuracy for hypoglycemia levels, skin irritations, and long warm-up period [47], [48].

1.2.6. Raman Spectroscopy (Non-invasive)

Raman spectroscopy is based on the use of a laser light to induce oscillation and rotation in human fluids containing glucose. Because the emission of scattered light is influenced by molecular vibration, it is possible to estimate glucose concentration in human fluids [49]. This effect depends on the concentration of the glucose molecules. This technique can measure very weak signals,

even in human fluids. The wavelength range of Raman spectrum is considered to be 200 cm^{-1} to 2,000 cm^{-1} [50]. Raman spectrum of glucose can be differentiated from those of other compounds in this band.

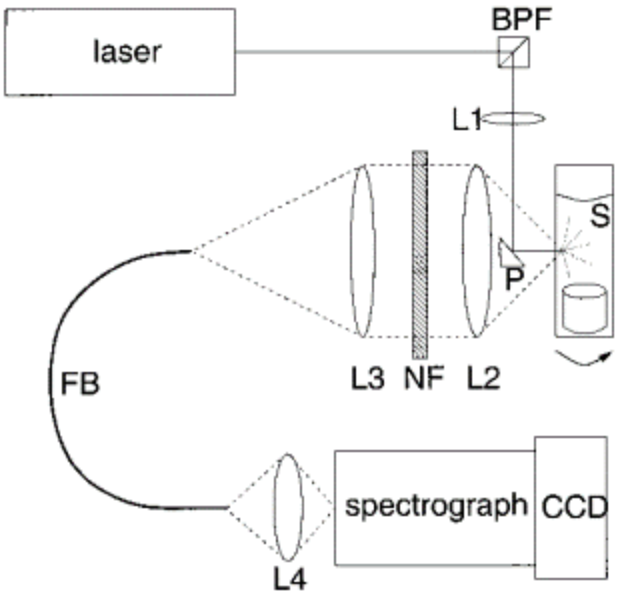

Figure 1-3: Experimental setup for acquisition of Raman spectra from blood samples: BPF, bandpass filter; P, prism; S, blood sample; L1-L4, lenses; NF, notch filter; FB, fiber bundle [49].

Raman spectroscopy usually provides sharper and less overlapped spectra compared to NIR spectroscopy. The intensity of spectral features is proportional to the concentration of the particular species, and the spectra are less sensitive to temperature changes. Moreover, it is comparatively less sensitive to water, and the interference from luminescence and fluorescence phenomena is only modest. The main limitations are related to instability of the laser wavelength and intensity, and long spectral acquisition times. In addition, as the power of the light source must be kept low to prevent injury, the signal-to-noise ratio is significantly reduced. Moreover, as with NIR spectroscopy, interference from other compounds remains a problem.

1.3. Previous Work and Challenges

Before designing antennas, the challenges and suggestions from previous work by Dr. Venkataraman's research group in ETA lab at RIT were discussed [16]-[18]. The antennas previously designed were successfully tracking the blood glucose increase/decrease by continuously noting the shift in antenna's resonant frequency. Some drawbacks in those designs were as follows:

1) They were large in size when compared to current on body sensors.
2) Patients who volunteered for testing antennas were required to keep their arm in a steady position, as the monopole antenna is omnidirectional which caused back radiation (radiation away from the body).
3) Bending effects of the antenna were not studied.

In order to overcome these challenges, various papers were reviewed. Keeping the back radiation in mind, complete ground plane antenna was our first choice. As seen from image theory, complete ground plane antennas helps in getting rid of the back radiation but unfortunately also give rise to destructive interference, which completely deteriorates the antenna efficiency. Next step was to improve the efficiency and also have zero back radiation.

Let us keep the substrate of thickness λ/4 to obtain a constructive interference (discussed later in this chapter) with the impinging wave. For example, we use a substrate which has an effective permittivity $\epsilon_{eff} = 3$ with respect to air. The wavelength inside the substrate can be calculated as:

$$\lambda = \frac{c}{f\sqrt{\epsilon_{eff}}} \qquad \text{Eq. (1.1)}$$

where c is the velocity of the waves in free space, and f is the desired operating frequency. Considering we want to operate the antenna at 2.45 GHz, and using the free space velocity as 3×10^8 m/s, the quarter wavelength of the waves inside the substrate turns out to be 17.6mm. This is a very thick substrate that can be used on body. Even if we use a substrate with higher dielectric constant, the thickness doesn't reduce much. For example, for a substrate with $\epsilon_{eff} = 10$, the quarter wavelength turns out to be ~1cm which is again thick to incorporate the design into wearables or on body sensors. High dielectric substrates are best suited for implants [52]–[55]. Whereas our goal is to attain non-invasive antennas. Another drawback of a thick substrate is that is give rise to surface waves.

Additionally, the proposed antenna designs are operated at higher frequency compared to the previously designed antennas. The goal then was to see if the antenna was able to track the blood glucose change, hence designing antenna at a lower frequency was a good decision. Now a days, with growing on body sensors and necessity for smaller antennas, designing antennas at lower frequency is out of question. Next step was to identify the frequency band that is higher than the frequency of operation of previous designs and also whether it lies within the Cole-Cole model bands of frequency, which will allow good penetration.

Artificial magnetic conductor was considered over complete ground planes due to it's in phase reflection property, which also helps in gain enhancement. The research being new in this area, most of the AMC were designed to increased bandwidth, or reducing the SAR on body for wireless telemetry and also to reduce the effect of lossy nature of body on the antenna's performance. Whereas, in this thesis, AMC will be used to focus the radiation in to the body. This thesis has covered most of the challenges expressed above.

1.4. Organization of the Thesis

1.4.1. Frequency dependence of biological tissue and Cole-Cole model

Conventionally antenna parameters, such as impedance bandwidth and efficiency are defined for the antenna located in free space. This thesis focuses on antennas that are used in environments comprising the free space and lossy medium, which is typically human tissue. For this reason, it is important to discuss parameters that describe wave behavior in lossy medium. As lossy dielectrics, the body's tissues display a complex permittivity. When an electric field is applied to a dielectric, the material will take a finite amount of time to polarize [56].

If the field is time varying, this lag (or "relaxation time") will cause the polarization of the dielectric to be out of phase with the field, with components both in phase with and in quadrature with the applied field. The permittivity will then be complex. The complex permittivity ε of the medium is defined as

$$\epsilon^* = \epsilon' - \mathrm{j}\epsilon'' = \epsilon' - \mathrm{j}\frac{\sigma}{\omega\epsilon_0} \qquad \text{Eq. (1.1)}$$

where ϵ' is the real part of the permittivity representing the polarization in line with the field and the imaginary part ϵ'' of the permittivity representing the component of the polarization in quadrature with the field. The phase difference between the field and the polarization will cause losses, attenuating the wave as it travels through the dielectric due to damping of vibrating dipole moments. Separating real and imaginary parts gives:

$$\epsilon_\mathrm{r} = \epsilon', \sigma = \epsilon''\epsilon_0\omega \qquad \text{Eq. (1.2)}$$

where $\epsilon_0 = 8.854 \times 10^{-12}$ F/m.

Since the complex permittivity of a medium is a frequency-dependent property and the properties of blood will change with respect to the glucose content in the blood, the dielectric properties of biological tissues can be expressed through the Debye model Eq. (1.3). This model represents a wideband frequency-dependent dielectric spectrum through a compact and analytical representation. One of the most commonly used models is a modified version of the Debye expression, named as Cole-Cole model Eq. (1.4).

$$\epsilon^*(\omega) = \epsilon'(\omega) - j\epsilon''(\omega) = \epsilon_\infty + \sum_{m=1}^{n} \frac{\Delta\epsilon_m}{1 + (j\omega\tau_m)} + \frac{\sigma_s}{j\omega\epsilon_0} \qquad \text{Eq. (1.3)}$$

$$\epsilon^*(\omega) = \epsilon_\infty + \sum_{m=1}^{n} \frac{\Delta\epsilon_m}{1 + (j\omega\tau_m)^{(1-\alpha_m)}} + \frac{\sigma_s}{j\omega\epsilon_0} \qquad \text{Eq. (1.4)}$$

where $\epsilon^*(\omega)$ is the frequency dependent complex dielectric constant, $\Delta\epsilon$ is the strength or magnitude of the dispersion, τ is the relaxation time, ϵ_∞ is the dielectric constant at infinite frequency, σ_s is the static conductivity $1 - \alpha$ is called the Cole-Cole model exponent which describes the broadness of the relaxation time distribution.

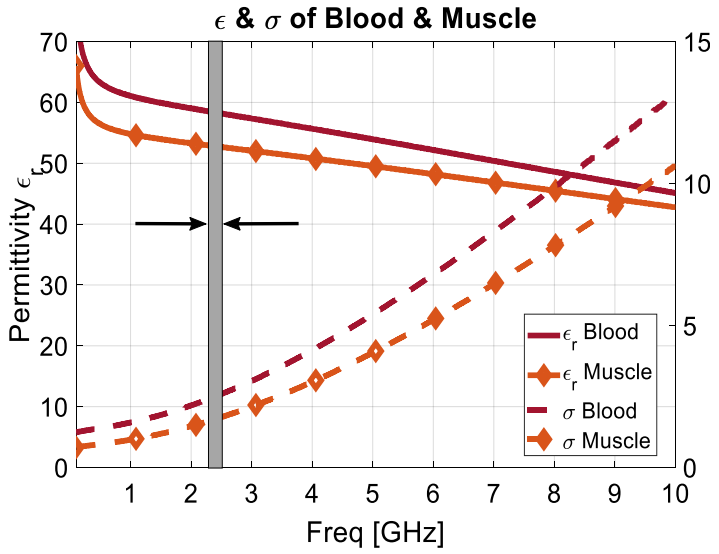

Figure 1-4: Permittivity and conductivity for blood and muscle. [80]–[82]

Figure 1-4, shows a trend in permittivity and conductivity, for blood and muscle over a frequency range. The permittivity of blood in the lower frequency band goes through a sharp change. Even though lower frequency has a good penetration depth, at low frequencies, to operate in a band lower that 1 GHz is not advisable as the permittivity of the blood will be changing drastically. As we go towards higher frequency in the range above 10GHz, the trend in permittivity becomes flatter but the penetration depth decreases. In order to have a good penetration depth as well as a flatter permittivity, a band of unlicensed ISM (2.4GHz -2.5GHz) was selected as an operating frequency for all the antennas designed in this thesis. Medical frequency laid out by FCC will be discussed in detail in the following sections.

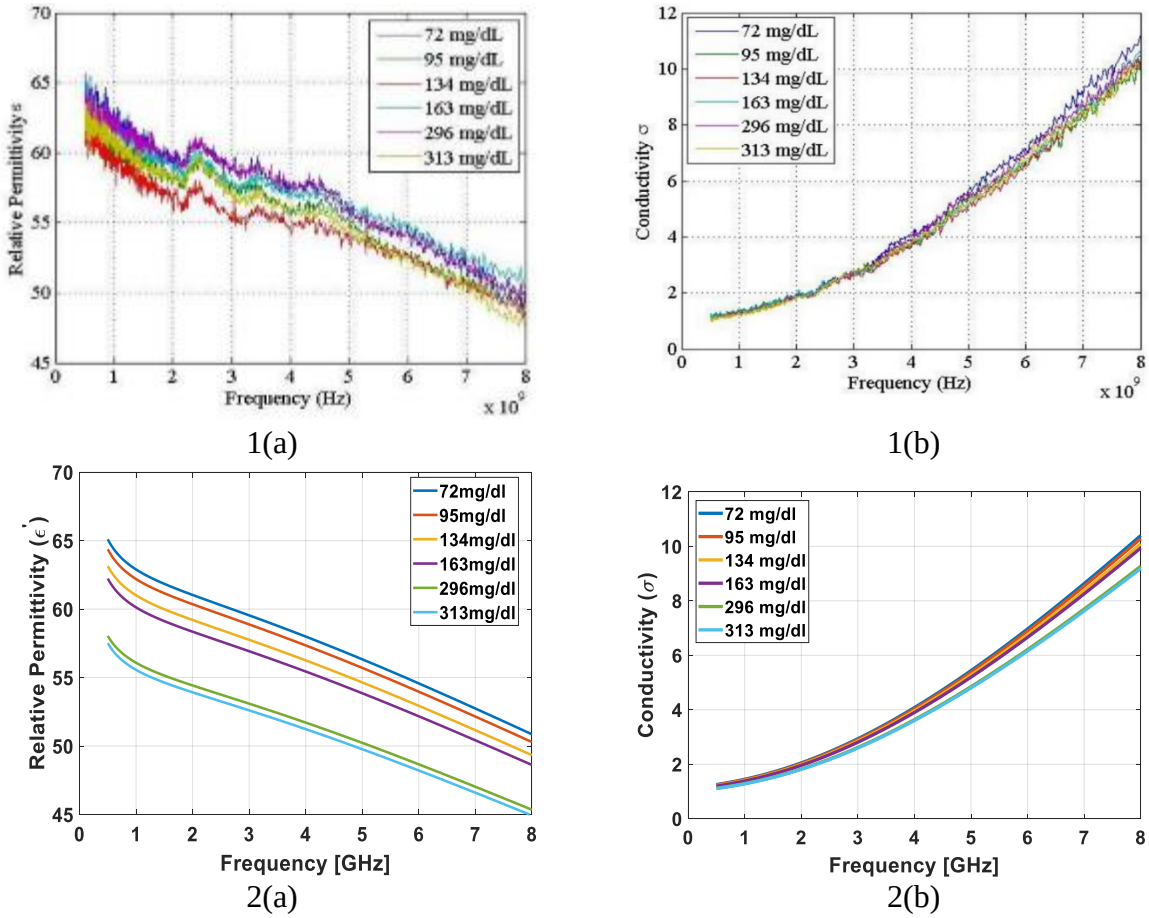

Figure 1-5: 1(a) and 1(b) Relative permittivity of in vitro experiment and modified Cole-Cole model. 2(a) and 2(b) Conductivity of in vitro experiment and modified Cole-Cole model

Now since the Cole-Cole model only shows the permittivity dependency with respect to the wideband frequency for biological tissue, a model with changing blood glucose must be included in blood's Cole-Cole model.

Dr. Venkataraman's research group in the ETA lab at RIT already remodeled the Cole-Cole equation in Eq. (1.4), for blood glucose. They performed in-vitro analysis to very this modified model [51] as,

$$\epsilon(\omega) = \epsilon_\infty + \left[\frac{\sigma_s}{j\omega\epsilon_0} + \sum_{m=1}^{2} \frac{\Delta\epsilon_m}{1 + (j\omega\tau_m)^{(1-\alpha_m)}}\right][0.001445g - 1.145882] \qquad \text{Eq. (1.5)}$$

However, the in-vitro measurements were not accurate, as they multiple blood glucose sample were not taken from a single subject. Since the glucose factor was modeled with respect to the in-vitro measurements, the Cole-Cole model also remains inaccurate. Therefore, multiple in-vitro measurement should to taken from blood sample from single subject and then following the same for other subjects in order to come up with a model that can track the exact glucose value from antenna's resonant frequency shift.

1.4.2. Selecting Frequency bands operating in Medical devices

Over the years with an increase in body worn devices, and with the vacant spectrums that are untouched due to interference issues for long distance communication, unlicensed bands were let out by FCC. Unlicensed frequency bands are mainly used to operate lower power devices over a short distance (see Table 1-2). The ITU-R Recommendation SA.1346 [57] outlined the use of the 402.0–405.0 MHz frequency band for medical implant communication services (MICS). The latest contribution in the field is the Institute of Electrical and Electronics Engineers (IEEE) 802.15.6

standard (IEEE 2012) which deals with short-range, wireless communications on or in, the human body. The standard refers to existing industrial, scientific, and medical (ISM) bands and frequency bands accepted by national medical and/or regulatory specialist as well. This standard mentions that, an implantable medical devices (IMD) shall be able to assist transmission and reception in not less than one of the following frequency bands: 402.0–405.0, 420.0–450.0, 863.0–870.0, 902.0–928.0, 950.0–958.0, 2,360.0–2,400.0, and 2,400.0–2,483.5MHz. Ultra wide band (UWB) IMDs which implement low band (3.494–4.492 GHz) or high band (6.489–9.984 GHz) channels are also supported. For instance, Table 1-1 outlines recent literature on implantable antennas operating within various frequency bands. The ISM band of 2,400.0–2,500.0 MHz [57] is appearing as one of the most favorable solutions. This is because it is already well developed in terms of technology (Bluetooth, WiFi, and WLAN), antennas, integrated circuits, and embedded systems.

Moreover, higher operation frequencies permit the use of smaller-sized antennas and components. It is for this reason that implantable antennas used at higher frequencies (e.g., 5.85 and 31.5 GHz) have also been reported in the literature (see Table 1-1). However, a high number of operating services are collocated in the previously mentioned bands. To deal with interference issues, the 402.0–405.0 MHz band mainly focusing on IMDs, which has been purely allocated for medical implant communication services (MICS). The United States Federal Communications Commission (FCC) and the European Radio communications Committee (ERC) currently regulate the MICS band. Its spectrum of 3 MHz allows for 10 channels (bandwidth of 300 KHz each) to operate simultaneously (i.e., multiple IMDs in the same area). It also limits potential interferences from the collocated Meteorological Aids Service band (401–406 MHz). The MICS band is available globally and reasonable with low power circuits, falls within a pretty low noise portion

of the spectrum, and allows for acceptable propagation through human tissue. The effect of operation frequency upon the performance of IMDs has been addressed in the literature. [58] and [59] has been presented to show increased power absorption, higher net body losses, and reduced penetration depths with increasing frequency. In order to work with antennas on body that requires into the body radiation, along with small size antennas under unlicensed medical band, this thesis is proposed to work in the unlicensed ISM band of 2.4GHz-2.5GHz, adhering to Cole-Cole model.

Frequency	References for Implantable Medical Devices
402 MHz	Scalp implant, implants with different digital phantoms, Implantable antennas at various human positions, Implantable microstrip antenna, Implantable Microstrip antenna using Genetic Algorithm, Transmission of RF signals between antenna in Free space and in human head, Implantable antenna in WTMS [53], [59]–[68]
433 MHz	Scalp implant, Effects of human body on implants, , Implantable antennas at various human positions, RF coupling for an artificial hip [67]–[70]
868 MHz	Scalp implant, implants with different digital phantoms [53], [59], [70]
915 MHz	Scalp implant, [53], [58], [67]
1575 MHz	Inverted F antenna implant for GPS application [71]
2400 MHz	Design of an implantable slot dipole, Cavity slot antenna embedded in human arm, Implantable antenna in WTMS, Effects of human body on implants [64]–[67], [72], [73]
31.5 GHz	Patch antenna design for medical implants [74]

Table 1-1: Resonant Frequencies of implantable antennas reported in the literature

		Frequency band	General Usage
Medical Radio Communication service (MedRadio) (MICS also operates in this band)	Authorized under Part 95, Subpart I	401-406 MHz	Medical devices for transmitting data containing operational diagnostics and therapeutic information associated with a medical implant device or medical body worn devices.
Medical Micro power Networks (MMNs)	Authorized under Part 95, Subpart I	413-419 MHz 426-432 MHz 432-444 MHz 451-457 MHz	Wireless medical devices that can be used to restore functions to paralyzed limbs
Medical body Area Networks (MBANs)	Authorized under Part 95, Subpart I	2360-2400 MHz	Networks of Body-worn sensors that transmit patient data to a health care provider
Wireless Medical Telemetry Services (WMTS)	Authorized under Part 95, Subpart H	608-614 MHz 1395-1400 MHz 1427-1429.5 MHz (location specific) 1429-1431.5 MHz (location specific)	A short distance data communication service for transmitting patient medical information to a central monitoring location in a medical facility.
Unlicensed ISM (Industrial Scientific and Medical)	Authorized under Part 15	13553-13567 kHz, 26957-27283 kHz, 40.66-40.70 MHz, 902-928 MHz **2400-2500 MHz** 5725-5875 MHz 24-24.25 GHz	License-exempt or unlicensed spectrum is free from centralized control in which anyone can transmit without a license while complying with rules that are designed to limit/avoid interference.

Table 1-2: Alloted Medical Frequency bands by FCC [75]

1.4.3. Specific Absorption Rate and Penetration Power

Electromagnetic radiation consists of waves of electric and magnetic energy moving together (radiating) in free space at the speed of light. Taken together all forms of electromagnetic energy are referred to as electromagnetic spectrum. Radio waves and microwaves emitted by transmitting antennas are one form of electromagnetic energy. They are collectively referred to as "radiofrequency" or RF energy or radiation. The RF waves emanating from an antenna are generated by the movement of electrical charges in the antenna. Ionization is a process by which electrons are stripped from atoms and molecules. This process can cause molecular changes that can lead to damage in biological tissue, including effects on DNA, the genetic material of living organisms. This process requires high levels of electromagnetic energy. The energy levels associated with RF and microwave radiation are not good enough to cause ionization of atoms and molecules.

It has been known for many years that exposure to very high levels of RF radiation can be harmful due to the ability of RF energy to heat biological tissue rapidly. Exposure to a very high RF intensities can result in heating of biological tissue and an increase in body temperature. Tissue damage in humans could occur during exposure to high RF levels because of the body's inability to cope with or dissipate the excessive heat that could be generated.

The exposure limits used by the FCC are expressed in terms of SAR, electric and magnetic field strength and power density for transmitters operating at frequencies from 100 kHz to 100GHz. The applicable limits depend upon the type of sources. (e.g., cellphones, wearables, broadcast transmitting antenna). The FCC's exposure guidelines specify limits for human body exposure to RF emissions in terms of Specific Absorption Rate (SAR), a measure of rate of absorption of RF energy by the body. The safe exposure limit is presented in Table 1-3.

From Table 1-3 we fathom that the tolerated exposure or the absorption rate is 1.6 W/kg over 1g of tissue when antenna is used against the head and 4W/kg averaged over 10g of tissue when positioned on the wrist.

SAR	Whole Body[1]	Partial Body[2]	Hands, Wrist, Feet and Ankles [3]
Occupational/Controlled Exposure Limits (W/kg)	0.4	8	20
General Population/Uncontrolled Exposure Limits (W/kg)	0.08	1.6	4

Table 1-3: SAR limits listed by Federal Communications Commission (FCC) [76]–[78]

[1]Whole body SAR is averaged over the entire body

[2] Partial Body SAR is averaged over any 1g of tissue in the shape of a cube

[3] SAR for hands, wrists, feet and ankles is averaged over 10g of tissue in the shape if a cube

In short, the electromagnetic power originated from an antenna and absorbed by human tissue is described by SAR values. SAR is defined as the power absorbed by the tissue per unit of mass and is related with the electric field

$$\mathrm{SAR} = \frac{\sigma}{\rho}|\bar{\mathrm{E}}|^2 \qquad \text{Eq. (1.6)}$$

where ρ is the tissue density [kg/m^3] and $|\bar{\mathrm{E}}|$ refers to the rms electric field value [79].

1.4.4. Antenna Miniaturization Techniques

Dimensions of the traditional half-wavelength (λ/2) or quarter wavelength (λ/4) antennas at the frequency bands allocated for medical implants and especially at the low-frequency MICS band make them useless for implantable applications. As an example, the free-space wavelength at 402, 433, 868, and 915 MHz can be computed as 74.6, 69.3, 34.6, and 32.8 cm, respectively. Therefore, miniaturization becomes one of the greatest challenges in implantable antenna design. Fortunately, human tissues in which implantable antennas are intended to operate exhibit high permittivity (e.g., the permittivity of skin at 402 MHz is 46.7 [80]–[82]) or, equivalently, reduced wave propagation velocity. This, in turn, increases the effective dielectric constant of the antenna and works to advantageously miniaturize its physical size.

Miniaturization methods that have been proposed in the literature for implantable antennas include:

1. **Use of high-permittivity dielectric materials**: High-permittivity dielectrics are selected for implantable antennas (e.g., ceramic alumina (ϵ_r = 9.4) [83] or Rogers RO3210 (ϵ_r = 10.2)[53]) because they shorten the effective wavelength and result in lower resonance frequencies, thus assisting in antenna miniaturization.
2. **Lengthening of the current flow path on the antenna surface**: Longer effective current flow paths excited on the antenna can reduce the resonance frequency and achieve a more compact size for the implantable antenna. For this purpose, meandered [84], spiral [84], waffle type [62], and hook-slotted [85] shaped implantable antennas have been suggested.[53]
3. **Addition of shorting pins**: In the case of implantable patch antennas, inserting a shorting pin between the ground and patch planes increases the effective size of the antenna. This, in turn, reduces the required physical dimensions, given a specific operation frequency scenario. The

technique works in much the same way a ground plane doubles the height of a monopole antenna, i.e., it typically produces a planar inverted-F antenna (PIFA) with the same resonance performance as a double-sized antenna without the shorting pin [61].

4. **Patch stacking**: In the case of implantable patch antennas, vertically stacking two radiating patches reduces antenna size by increasing (nearly doubling) the length of the current flow path [53], [83].

1.4.5. Artificial Magnetic Conductors and its Applications

The good property of an electric metal is that it is an excellent reflector. But the drawback that comes with it is they also reverse the phase of the reflecting wave compared to the incoming wave. Good conductors restrict internal electric fields. They also maintain continuity across the metal/air boundary forces the tangential electric field at the surface to zero. When an electromagnetic wave impinges on a conductor, the reflected wave experiences a phase reversal to ensure that the electric field has a node at the surface[86]. Image theory states that a PEC ground plane causes the antenna's current and its image to cancel each other which is responsible for dropping the real part of the impedance towards zero, while the imaginary part approaches infinity. Hence, a significant amount of the electromagnetic energy is trapped between the antenna and the ground plane which in turn leads to a significant reduction in the antenna's efficiency [86].

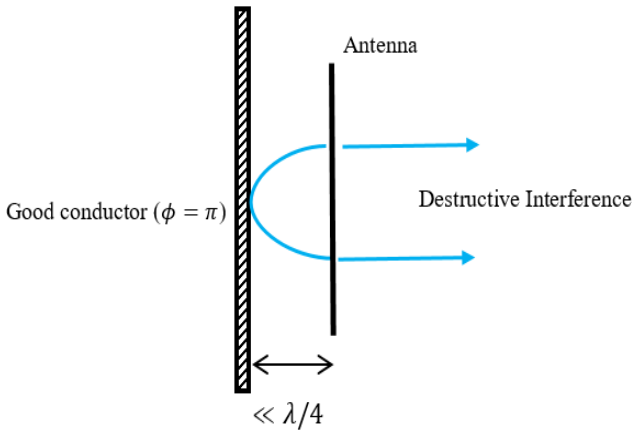

Figure 1-6 Antenna placed on a metal conductor at a distance very less than λ/4

Likewise, the magnetic field has an antinode at the surface. As it is well known from literature, many antennas are designed using a flat metal conductor to utilize it reflection property. As seen in Figure 1-7, the presence of a ground plane redirects half of the radiation into the opposite direction, improving the antenna gain by 3dB, and partially shielding objects on the other side. But if the antenna is too close to the metallic surface, the phase of the incoming wave is reversed upon reflection, resulting in destructive interference with the wave emitted in the other direction.

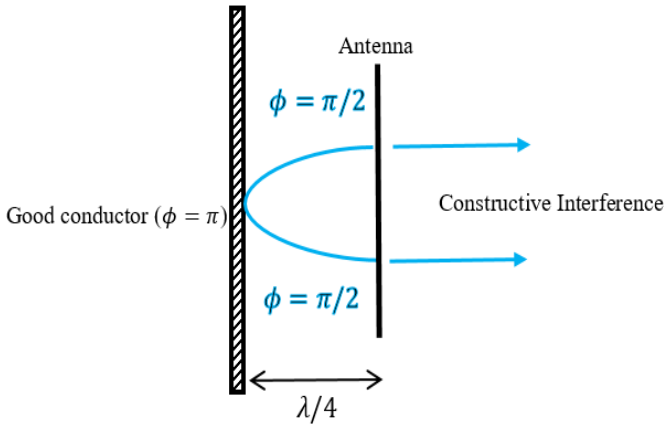

Figure 1-7: Antenna placed on a metal conductor at a distance of λ/4

This results in poor radiation efficiency. Figure 1-6 depicts an antenna in close proximity with a flat, conducting slab. The antenna is effectively shorted out by the metal surface, and negligible radiation is emitted. This problem is solved by including a one-quarter wavelength space between the radiating element and the ground plane, as shown in Figure 1-7. The total round trip phase shift from the antenna, to the surface, and back to the antenna, equals one complete cycle, and the waves add constructively. The antenna radiates efficiently, but the entire structure requires a minimum thickness of λ/4. Another property of metals is that they support surface waves. [3, 4] AMC ground plane (which emulates a PMC in a specific frequency band) is used instead of PEC due to its in-phase reflection characteristics. Similar to the concept explained for the metal conductor, magnetic

conductors have a property of reflecting the wave in phase compared to the incoming wave. Hence as the PMC layer reflects all of the power just like a metal sheet, but it reflects in-phase, rather than out-of-phase, allowing the radiating element (antenna) to be directly adjacent to the surface, shown in Figure 1-8. Thus, utilizing an AMC as a ground plane significantly enhances the gain of dipole/monopole antennas [87].

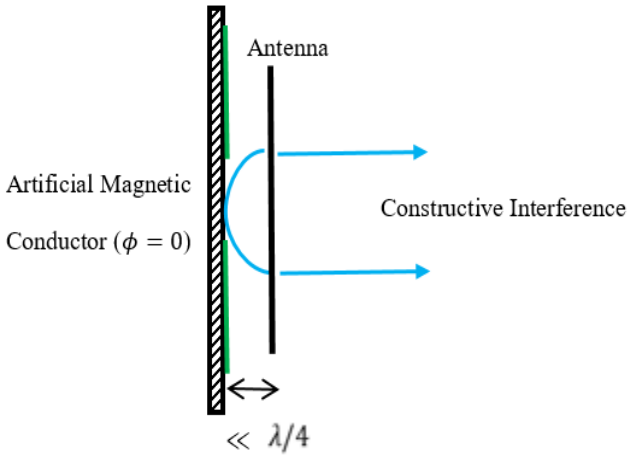

Figure 1-8: Antenna place on AMC surface at a distance very less than λ/4

In the application [87]–[89], the AMC ground plane is used to isolate the user's body from undesired exposure to electromagnetic radiation in addition to eliminating the antenna's impedance mismatch caused by the proximity to human tissues. The main drawback of using unilayer FSSs over a metallic ground plane is the very narrow AMC operation bandwidth [90].

1.4.6. Review of Integrated Antenna on Body

One major challenge for antenna design in WBANs (wearable body area networks) is related to alterations in the antenna topology based on the shape of the human body, which specifies the need for flexible and textile antennas. However, these types of antennas are not easily adjustable to body

dynamics as they are mainly built on top of substrates with little deformation capability [91]. One other major challenge is due to the electromagnetic interaction between the human body and the antenna. The human body is considered as a large inhomogeneous object with high loss and permittivity, which affects the properties of an antenna being placed in its close proximity. Existing antennas in WBANs may be classified into two groups [92]:

1) Magnetic antennas: Magnetic antennas, such as loop antennas, generate an E-field that is mostly tangential to the body tissue and, therefore are not capable of coupling as strongly as the electric antennas. Consequently, body fat does not heat up. Some partially similar antennas to the magnetic antennas are the helical-coil antennas, which have the same heating characteristics as the electrical antennas. Tissue heating is mainly a result of the strong Electric Field (E-field) existing between the coils [92]. Additionally, the Specific Absorption Rate (SAR) of the far field-transmitting antenna is mainly related to the E-field, whereas the SAR of the near field-transmitting antenna is related to the Magnetic Field (H-field) [92].

2) Electric antennas: Electric antennas such as dipole antennas form a large amount of E-field perpendicular to the body that is absorbed and increases the temperature of the human tissue. This is because the boundary requirement of the E-field is discontinuous by the ratio of its permittivities at the E-field. Since muscle has higher permittivity than fat, the E-field of the fat tissue is generally higher [92]. The human body is not considered as an ideal medium for electromagnetic wave transmission at radio frequencies. Consequently, based on the utilized frequency, high path loss occurs in the human body due to central frequency shift, power absorption and alterations in the radiation pattern. Additionally, absorption effects differ in

magnitude based on the characteristics of the tissue and the frequency of the applied field [92]. In general, propagation throughout the body is affected in numerous ways due to the electrical properties of the body, which are as follows:

- Body tissue is semi-conductive and therefore capable of absorbing some of the signal.
- Body tissue can react as a parasitic radiator.
- The electrical length of the electric field antennas like dipoles increase as dielectric constant increases.

The antennas designed for WBANs are classified into two groups based on their location to be either placed on the body or in the body. A brief explanation of these classifications is provided as follows:

In-body Antenna Design – As for the antennas being implanted in the body, only specific types of materials such as titanium or platinum can be used due to their biocompatible and non-corrosive chemistry, whilst a copper antenna has better performance [93]. The MICS band, which is from 402-405 MHz, is allocated for in-body communication. The wavelength of this frequency is 744mm and the half wave dipole is 372mm. However, an antenna with such dimensions is not applicable to in-body operation and therefore these constraints lead to a much smaller size than the optimum.

On-body Antenna Design – Two key requirements for on body communication of antennas are the antenna radiation pattern and the sensitivity of antennas to the human body. In [94], a comparison of antenna combinations for on-body communication is provided. Various antennas

have been designed and constructed in the 2.5 GHz and ISM band, such as loop antennas, patch antennas, patch array antennas and monopole antennas. Amongst which, the monopole and monopole combinations provide the least link loss and the highest path gain (path gain interprets as the product of all transfer functions along a path) [94]. Whereas, patch antennas that do not require additional space are capable of reducing the spread of the path gain and therefore eliminate multi-path fading [95]. Some other existing antennas such as the spiral, the bow tie, the trailing wire, the Planar Inverted-F Antenna (PIFA) and the loaded PIFA are also applicable in different scenarios.

Thesis Design review

In this thesis we will be working with antennas over the AMC layer (together regarded as an integrated antenna). Usually the antenna that is placed over the AMC layer must resonate at the frequency where the AMC has a reflection phase of 0°, in order to achieve an enhanced broadside gain (or constructive interference). The operating frequency that we chose is 2.4-2.5GHz, where the antenna size will be large to be tested on arm. In order to make the antenna smaller it needs to operate at a higher frequency to keep the antenna design simple without fabrication complexities. The integrated antenna designed in [88] explains the integrated antenna model by designing the antenna at a frequency higher than the operating frequency, making the antenna small in size compared to the conventional antenna. When this antenna was placed over the AMC layer, the whole setup resonates at the frequency where the reflection phase of the AMC is +90°, making it an inductive surface. This concludes that since the antenna alone operates at a frequency below its fundamental resonant mode, its input impedance is capacitive. Hence when the monopole is loaded by the inductive surface which stores more magnetic energy, the reactance of the integrated

antenna is suppressed, thus achieving a good impedance match. Maximum coupling occurs placing the antenna at the center of the AMC, which has gaps that separates the metal conductors. Those gaps acts as a magnetic current slots and store more magnetic energy, which makes the AMC layer inductive. Hence positioning of the antenna with respect to the AMC is important.

Thesis Layout:

- In the beginning of chapter 2, different unit cell designs are discussed in detail with it equivalent circuit model, moving on to monopole antenna design.
- Chapter 3 discusses a step by step analysis of designing both antenna and one of the AMC together in free space and on arm. Later antenna when placed on other AMCs are discussed.
- Fabrication and measured results are discussed in Chapter 4 along with testing the antenna with AMC on arm of 2 non-diabetic subjects.
- The Antennas were also tested for moving arm, antenna's back radiation, and creeping waves.
- Finally the thesis was concluded and future work is suggested.

2. Design Analysis of AMC and Antenna

As this thesis focusses on designing better reflective ground planes, in this section a descriptive analysis how an AMC array is laid out by designing its individual unit cells is given. The HFSS model and the equivalent design circuits are discussed for the unit cells. 4 unit cell designs and 2 monopole designs are discussed.

2.1. Unit cells

As the name suggests, a unit cell represents a single cell on an array of cells, as shown in Figure 2-1. Simulation of a unit cell is given in Appendix A. Several unit cells were analyzed, from which 4 unit cells are discussed in this thesis, out of which 3 of them were fabricated and test later. When analyzing the unit cell, substrate material was not modified. The substrate used throughout this thesis is Rogers RT/duroid 5880™ with the dielectric permittivity, ϵ_r = 2.2 and $\tan(\delta)$ = 0.0009, with a thickness, h = 31 mils (or 0.7874 mm). Additionally half ounce copper is used (thickness of 18μm).

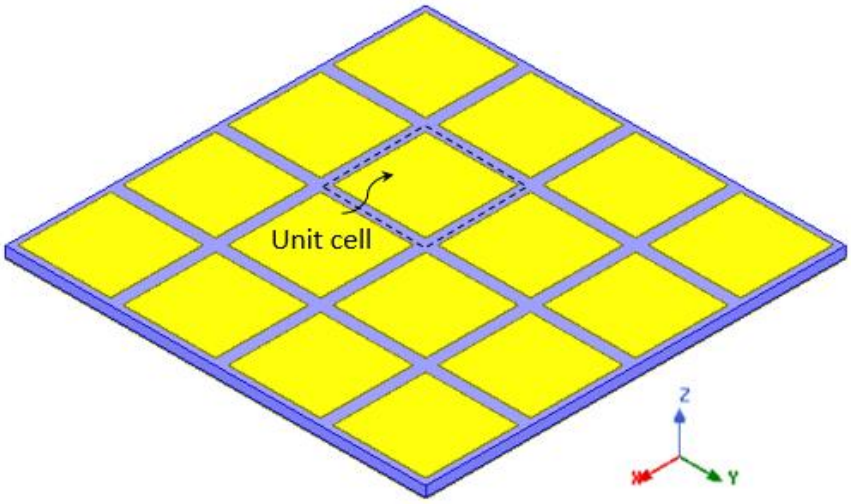

Figure 2-1: Unit cell in a 4×4 AMC array

Equivalent circuit analysis approach:

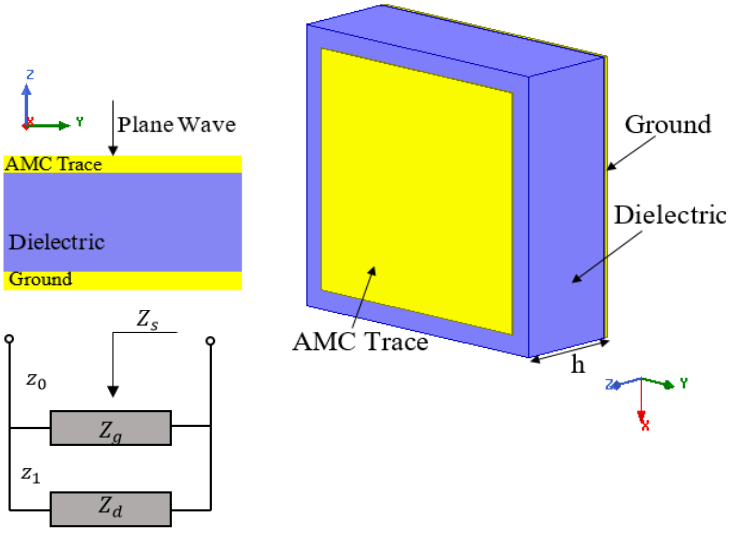

Figure 2-2: Unit cell and equivalent circuit model

Unit cells are modelled using LC equivalent circuits. Various approaches are documented in literature [96]–[100]. For the AMC structures, the surface impedance (Z_s) plays an important role to determine the resonant frequency and the phase of reflection coefficient. The surface impedance, in terms of the transmission-line approach can be expressed as a parallel connection of AMC trace impedance (Z_g) and the surface impedance of a grounded dielectric slab (Z_d) [96], [101]. Even though the model for all the unit cell explained below have the same structure of the equivalent model, the values of Z_g and Z_d will be different depending on the dimensions and design of the AMC layer. For any AMC unit cell, the model for Z_g narrows down to LC resonant circuit.

Analyzing equivalent circuit for a unit cell.

For AMC structures, the surface impedances (Z_s) can be expressed as a parallel connection of FSS impedance (AMC trace alone) (Z_g) and the surface impedance of a grounded dielectric slab (Z_d)

$$Z_s(\omega) = Z_g \;||\; Z_d \qquad \text{Eq. (2.1)}$$

Before we calculate the respective capacitance and inductance of a unit cell, let us look at the closed-form formula of characteristic impedance (Z_0) and effective permittivity ϵ_{eff} are used which have been reported by Wheeler and Schneider. Where Z_0 is expressed by,

$$Z_0 = \begin{cases} \dfrac{\eta_0}{2\pi\sqrt{\epsilon_{eff}}} \ln\left\{\dfrac{8h}{w} + 0.25\dfrac{w}{h}\right\} & ,\dfrac{w}{h} \le 1 \\ \dfrac{\eta_0}{\sqrt{\epsilon_{eff}}}\left\{\dfrac{w}{h} + 1.393 + \ln\left(\dfrac{w}{h} + 1.444\right)\right\}^{-1} & ,\dfrac{w}{h} \ge 1 \end{cases} \qquad \text{Eq. (2.2)}$$

Where η_0 the impedance of free space, h is the thickness of the dielectric slab, w is the width of the microstrip line that can be calculated using the effective dielectric constant,

$$\epsilon_{eff} = \frac{\epsilon_r + 1}{2} + \frac{\epsilon_r - 1}{2} F\left(\frac{w}{h}\right) \qquad \text{Eq. (2.3)}$$

where,

$$F\left(\frac{w}{h}\right) = \begin{cases} \left(1 + \dfrac{12h}{w}\right)^{-\frac{1}{2}} + 0.041\left(1 - \dfrac{w}{h}\right)^2 & ,\dfrac{w}{h} \le 1 \\ \left(1 + \dfrac{12h}{w}\right)^{-\frac{1}{2}} & ,\dfrac{w}{h} \ge 1 \end{cases} \qquad \text{Eq. (2.4)}$$

In order to calculate the capacitances and the inductances of the equivalent circuit model, we decompose every unit cell into capacitive components and inductive components. Let us assume a relatable model that is used in this thesis to explain how is capacitances and inductance calculated.

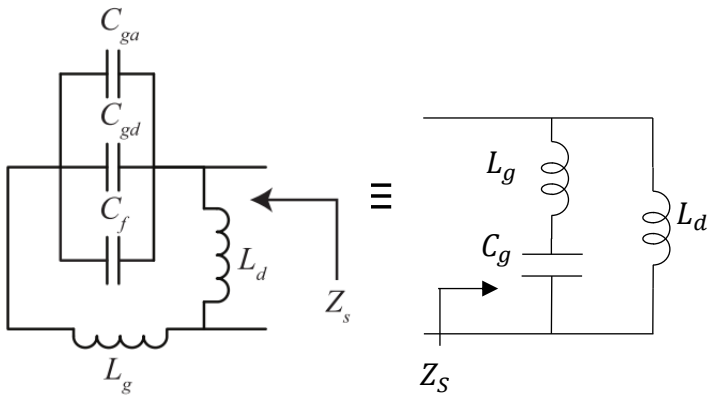

Figure 2-3: Equivalent circuit

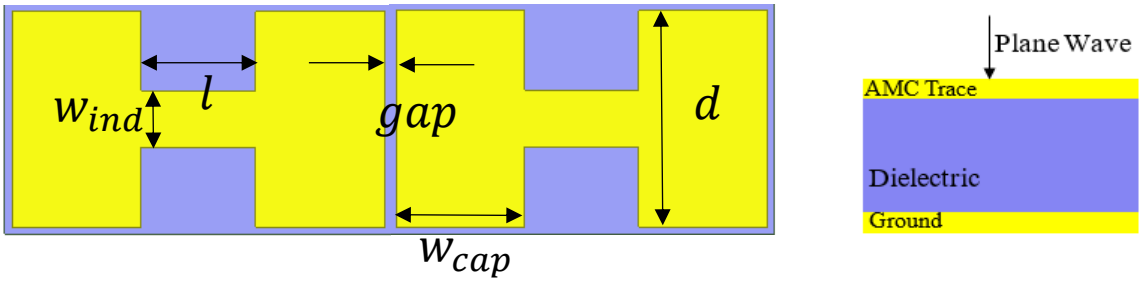

Figure 2-4: Geometry and dimensions of I shaped unit cell.

Grid Capacitances:

Capacitance due to gap between the adjacent unit cells. This capacitance depends on the length d and width w_{cap}. The combination of two parallel capacitive components with the gap distance gap at the surface of metal backed dielectric slab is similar to coupled microstrip lines. Let us define this capacitance as C_{ga}, which is the gap capacitance in air and can be calculated as,

$$C_{ga} = 2\epsilon_0\epsilon_{eff}\frac{K(k)}{K'(k)}d \qquad \text{Eq. (2.5)}$$

Where ϵ_0 is the permittivity of free space,

$$\frac{K(k)}{K'(k)} = \begin{cases} \frac{1}{\pi}\ln\left\{2\frac{1+\sqrt{k}}{1-\sqrt{k}}\right\} & ,0.707 \leq k \leq 1 \\ \frac{\pi}{\ln\left\{2\frac{1+\sqrt{k'}}{1-\sqrt{k'}}\right\}} & ,0 \leq k \leq 0.707 \end{cases} \quad \text{Eq. (2.6)}$$

$$k = \tan^2\left(\frac{a\pi}{4b}\right), \qquad a = \frac{w_{cap}}{2}, \qquad b = \frac{w_{cap} + gap}{2}, \qquad k' = \sqrt{1-k^2} \quad \text{Eq. (2.7)}$$

The effective permittivity can be calculated by Eq. (2.3) where w is replaced by w_{cap}. The second capacitance C_f is the fringe capacitance at the outer edge of the unit cell and can be obtained as,

$$C_f = \frac{1}{2}\left(\frac{\sqrt{\epsilon_{eff}}}{cZ_0} - \frac{\epsilon_0\epsilon_r w_{cap}}{h}\right) \quad \text{Eq. (2.8)}$$

Where c it the velocity of light in free space and Z_0 is obtained from Eq. (2.2) for a strip of width w_{cap}. The parameters holds to be within 3% of error for the ranges,

$$0.1 \leq \frac{w_{cap}}{h} \leq 10, \qquad 0.1 \leq \frac{gap}{h} \leq 5, \qquad 1 \leq \epsilon_r \leq 18 \quad \text{Eq. (2.9)}$$

The last capacitance C_{gd} represents the capacitance value due to the electric flux in the dielectric region. C_{gd} can be obtained from C_f by,

$$C_{gd} = \frac{\epsilon_0\epsilon_r}{\pi}\ln\coth\left(\frac{\pi gap}{4h}\right) + 0.65C_f\left\{\frac{0.02h\sqrt{\epsilon_r}}{gap} + \left(1 - \frac{1}{\epsilon_r^2}\right)\right\} \quad \text{Eq. (2.10)}$$

Using Eq. (2.5), Eq. (2.8) and Eq. (2.10) we can predict accurate values for capacitive components of a unit cell.

Grid Inductances:

The inductive component L_g can be calculated by using the length l and width w_{ind} using microstrip line theory,

$$L_g = \frac{Z_0\sqrt{\epsilon_{eff}}}{c} l \qquad \text{Eq. (2.11)}$$

Where Z_0 and ϵ_{eff} can be obtained by Eq. (2.2) and Eq. (2.3) when the width of the strips is replaced by w_{ind}. Eq. (2.11) is valid only when l is much smaller than the operating wavelength.

Inductance of the grounded metallic slab:

An AMC structure composed of a periodic array on a PEC-backed dielectric substrate with thickness h and permittivity ϵ_r is introduced. The resulting structure can be modeled using a transmission line as shown in Figure 2-5. The square patch acts as a shunt capacitor placed at a distance h from a short circuited dielectric loaded transmission line. This transmission line can be modeled by a lumped shunt inductor parallel to a capacitor [102]. The parallel LC circuit is inductive below resonant frequency and capacitive above resonant frequency. At frequencies much below than the resonant frequency the impedance approaches to zero and the structure behaves like a PEC surface.

The impedance can be simply obtained as [101],

$$Z_d = \left(\frac{j\eta_0}{\sqrt{\epsilon_r}}\right)\tan(kh) \qquad \text{Eq. (2.12)}$$

Since Z_d has been modeled by an inductance (L_d), we have $Z_d = j\omega L_d$. Therefore Eq. (2.12) now becomes,

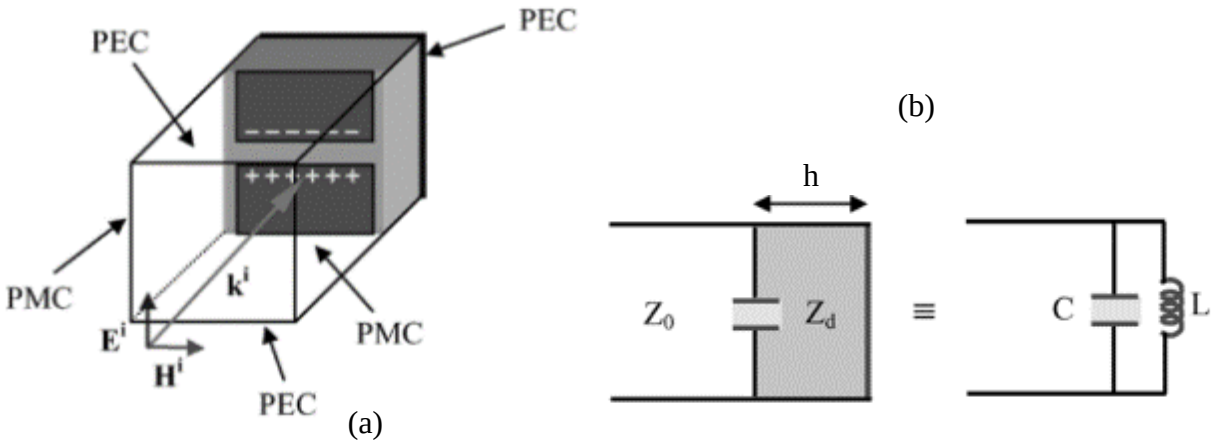

Figure 2-5: Unit cell of AMC bounded to the PMC-PEC walls in the y-z directions and illuminated by the normal incident plane wave. (b) Parallel LC equivalent model. Notice that the backside PEC after the distance h presents the inductive property [102].

$$L_d = \left(\frac{\eta_0}{\sqrt{\epsilon_r}}\right)\frac{\tan(kh)}{\omega} \qquad \text{Eq. (2.13)}$$

Where $k = \omega\sqrt{\epsilon_r\epsilon_0\mu_0}$ is the refracted wave number and $\eta_0 = \sqrt{\mu_0/\epsilon_0}$ is the impedance of free space and ϵ_r is the relative permittivity of the dielectric slab. From Eq. (2.13) it is observed that, the inductance is frequency dependent. For this model if all the dimensions including the thickness of the substrate are much smaller than the wavelength of interest ($k.h \ll 1$) then Eq. (2.13) can be turned into frequency independent equation[101],

$$L_d = \mu_0 h \qquad \text{Eq. (2.14)}$$

For the unit cell in Figure 2-4, the equivalent circuit can be modeled as shown in Figure 2-3. The parallel capacitances can be added where, $C_g = C_{ga} + C_{gd} + C_f$ and the circuit now narrows down to $L_g$and C_g in parallel with the ground inductance L_d.

Eq. (2.1) now becomes,

$$Z_s(\omega) = Z_g \,||\, Z_d = \frac{j\omega L_d\left(1-\omega^2 L_g C_g\right)}{1-\omega^2\left(C_g\left(L_g+L_d\right)\right)} \qquad \text{Eq. (2.15)}$$

At the resonant frequency the surface impedance is very high and the reflection phase coefficient is zero. Therefore, when the denominator of equals to zero, we get the resonant frequency as,

$$f_r = \frac{1}{2\pi\sqrt{\left(C_g\left(L_g+L_d\right)\right)}} \qquad \text{Eq. (2.16)}$$

The above equations can be used to design the equivalent circuits for the unit cell analytically.

Suggestion for synthesis of Equivalent circuit of a unit cell:

The equations for equivalent circuits if the unit cells above were performed in the analysis mode. If the design is to be done in the synthesis mode, for a known or required resonant frequency, the ground inductance (L_d) will remain constant for a given height of dielectric material that will be used. Assuming an impedance value for the grid inductance (L_g), the width and length for the grid inductance can be calculated using Eq. (2.11). Using the effective inductance the effective grid capacitance can be found using Eq. (2.16)

For example: We want to design the unit cell for 2.5GHz, L_d can be found using Eq. (2.14). For a dielectric material with height of 31mil. $L_d = 0.989nH$. The parameters that we know at this stage are, relative permittivity of the dielectric, ϵ_r the height of the substrate, h, resonant frequency, f_r and the inductance, L_d. Assuming the impedance Z_0 for inductance of the unit cell trace, L_g, let

us say, 20ohms, the corresponding width can be calculated using Eq. (2.2). The width turns to be, 8.08mm and the length of 11.7mm for an electric length of 50deg. For the required impedance the inductance of the unit cell trace, L_g, can be calculated using Eq. (2.11) which turns out to be 1.1nH. Using this value we can calculate the effective capacitance C_g. With all the mentioned values and using Eq. (2.16) $C_g = 1.94pF$. In order to find individual capacitances, further assumptions for impedances to calculate the width and lengths can be made. This is just a gist of how the equivalent circuit can be designed. Lot more work is required to get the exact length and width of the unit cell.

2.1.1. Rectangular Patch (AMC1)

Rectangular Patch AMC is one of the basic type derived from square patch. Since the antenna to be used over the AMC is linearly polarized, it will excite the AMC in a single direction. Hence the dimension of the AMC, L_p is varied to obtain resonance at the desired frequency. A plane wave is excited on the surface of the unit cell and the reflection phase is observed. The equivalent circuit was designed by modifying the circuit model derived in [96]. The length L_p gives rise to the inductance L_g and changes as L_p varies. The gap between the inductive AMC trace and the next AMC trace in an array of unit cell will give rise to capacitance C_g, less the gap more will be the capacitance. Finally, the ground plane will have its own inductance L_d. According to assumption for the effective surface impedance model all of the dimensions including the thickness of substrate are much smaller than wavelength of interest, L_d can be turned to the frequency-independent [96]. This results in constant L_d if the substrate height remains constant. Figure 2-7 shows variation in

reflection phase when each dimension of the unit cell is changed keeping the substrate material and the height of the material constant.

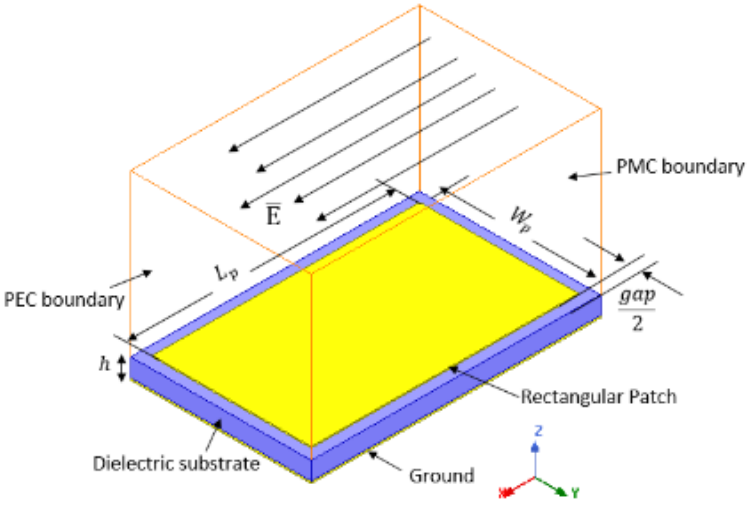

Figure 2-6: Rectangular patch type AMC unit cell and equivalent circuit.

Now in order to calculate the parameters for the equivalent circuit, from the design we observe that the patch acts as both inductive layer and conductor for the capacitive gaps. To solve the inductance L_g, the l in Eq. (2.11), is L_p and the width for calculating Z_0 is W_p, the inductance L_g turns out to be 1.503nH. For the gap capacitance C_{ga}, we use Eq. (2.5), here the d is W_p and the width for Z_0 is L_p. Substituting these values in Eq. (2.5) we get the value of C_{ga} as 1.099pF. Similarly the fringing capacitance C_f and the capacitance due to the conducting materials (AMC trace and the ground) C_{gd} can be calculated using Eq. (2.8) and Eq. (2.10), whose values are 0.355pF and 0.18pF respectively. Now adding all these capacitances gives the overall value of C_g as 1.6436pF. Now once we have all the values to the circuit. The resonant frequency where zero phase occurs can be calculated from Eq. (2.18) as 2.56GHz. Figure 2-8 shows that equivalent circuit model agrees with the HFSS simulation for a given dimensions of the unit cell.

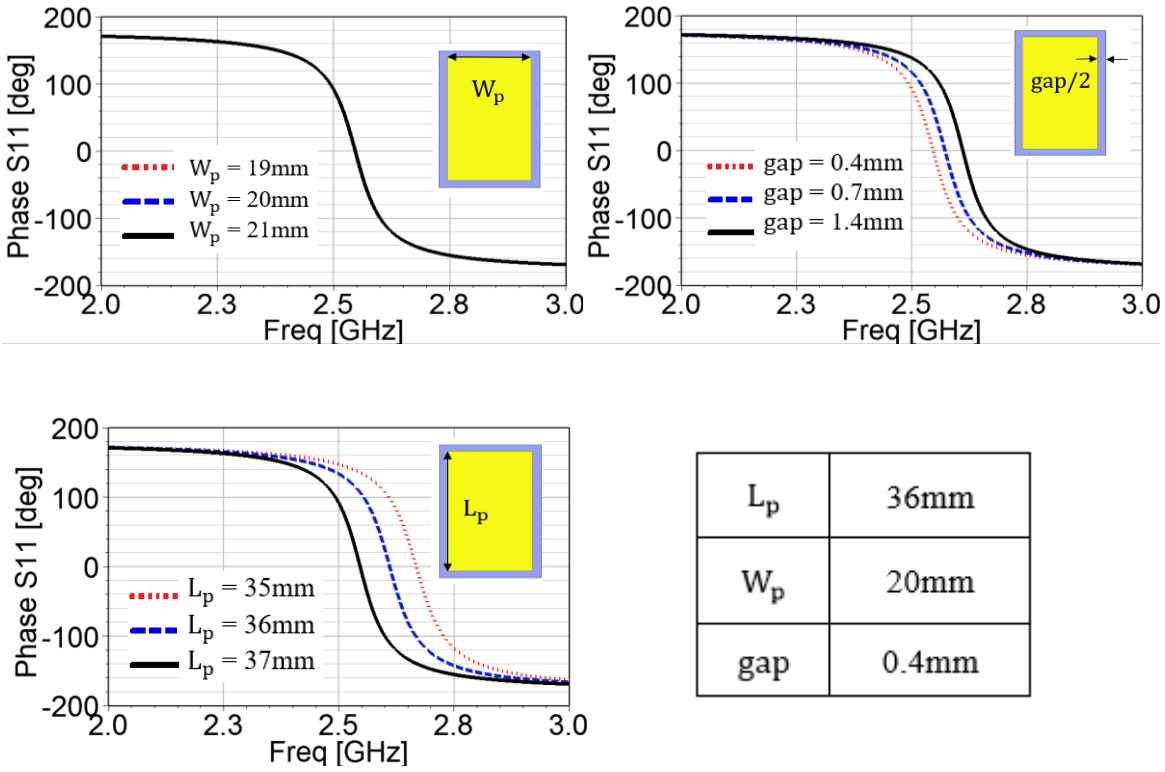

L_p	36mm
W_p	20mm
gap	0.4mm

Figure 2-7: S11 Phase in degrees with varying dimensions for Rectangular Patch AMC when keeping the other dimensions constant as listed in the table.

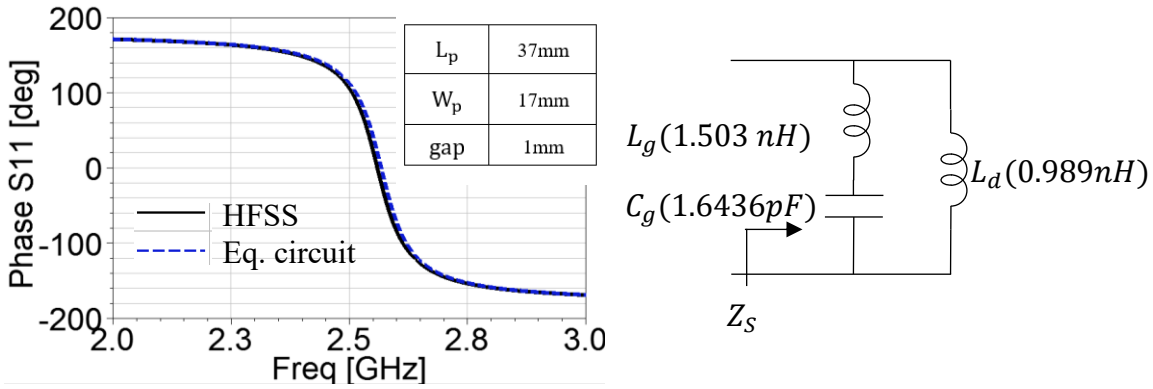

Figure 2-8: S11 Phase in degrees compared to the equivalent circuit model for Rectangular Patch AMC for the dimensions shown.

2.1.2. Rectangular Ring (AMC2)

Rectangular Ring AMC is similar to rectangular patch. The only difference is the AMC inductance that varies when compared to rectangular patch. The concept is very similar to that of the rectangular patch. Cutting patch in the center has helped the AMC resonate at the same frequency with size reduction. Increasing the width of the ring size R increases the inductance of the surface shifting to a higher frequency as seen in Figure 2-10. Similarly as the gaps between the unit cell is increased, the total circuit becomes less capacitive, making the resonant frequency to move to the right. Additionally the increasing the dimensions L_{r1} *and* W_{r1} moves the resonance to lower frequency making their contribution to the capacitance of the circuit. The equivalent circuit was designed by modifying the circuit model derived in [96].

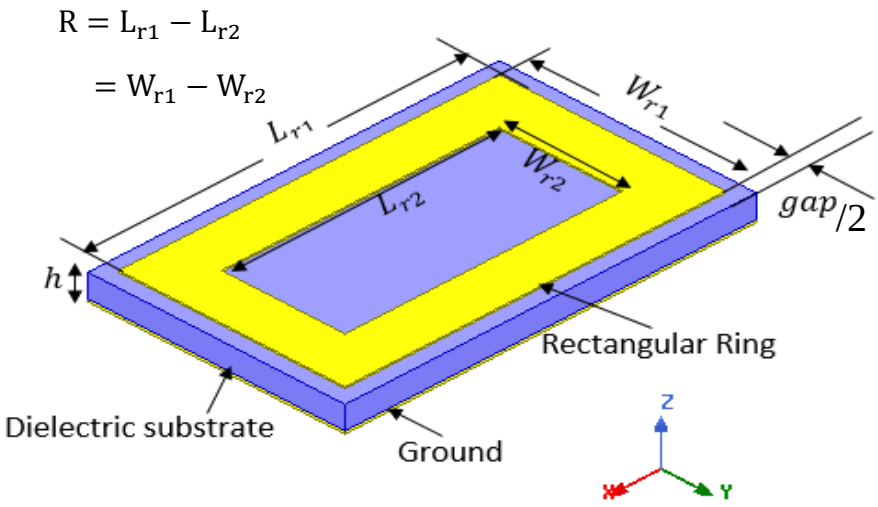

Figure 2-9: Rectangular ring type AMC unit cell and equivalent circuit

Now in order to calculate the parameters for the equivalent circuit, from the design we observe that the ring has an extra capacitance when compared to the rectangular patch. To solve the inductance L_g, the l in Eq. (2.11), is L_{r1} and the width for calculating Z_0 is R, the inductance L_g

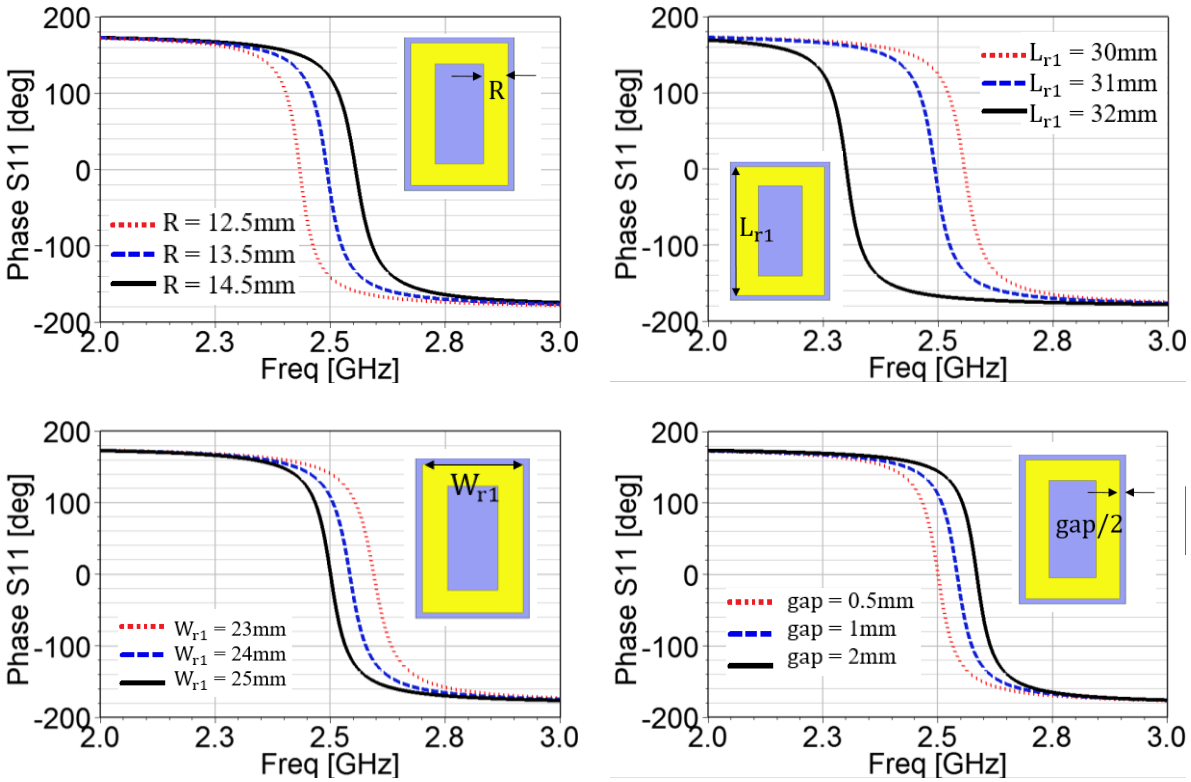

L_{r1}	31mm
W_{r1}	24mm
R	13.5mm
gap	0.5mm

Figure 2-10: S11 Phase in degrees with varying dimensions for Rectangular Ring AMC when keeping the other dimensions constant as listed in the table.

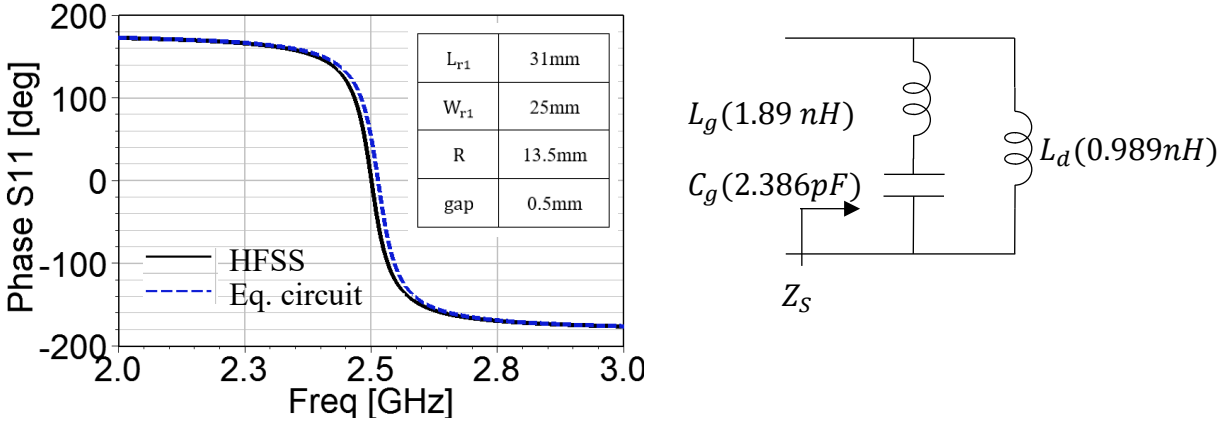

Figure 2-11: S11 Phase in degrees compared to the equivalent circuit model for Rectangular Ring AMC for the dimensions shown.

turns out to be 1.89nH. For the gap capacitance C_{ga}, we use Eq. (2.5), here the d is W_{r1} and the width for Z_0 is R. Substituting these values in Eq. (2.5) we get the value of C_{ga} as 1.43pF. Similarly the fringing capacitance C_f and the capacitance due to the conducting materials (AMC trace and the ground) C_{gd} can be calculated using Eq. (2.8) and Eq. (2.10), whose values are 0.28pF and 0.2pF respectively. The extra capacitance C_x can be calculated the same as solved for C_f where d is W_{r2} and width for Z_0 is R. The value of C_x turns out to 0.6pF. Now adding all these capacitances gives the overall value of C_g as 2.386pF. Now once we have all the values to the circuit. The resonant frequency where zero phase occurs can be calculated from Eq. (2.18) as 2.512GHz. Figure 2-8 shows that equivalent circuit model agrees with the HFSS simulation for a given dimensions of the unit cell.

2.1.3. I shaped design (AMC3)

The next unit cell designed is the I shaped unit cell similar to the one in [88]. This unit cell is the smallest of all the unit cell discussed in this thesis when compared to a single resonant frequency. Modifying the equivalent circuit design [96] agrees to the HFSS simulation. The dimension W_{i1} is the grid inductance L_g for the AMC. Whereas L_{i1}, L_{i2} and gap/2 adds to the total capacitance in parallel of the grid giving rise to capacitance C_g. As discussed earlier L_d remains constant for a given substrate. The dimensions and results are discussed in Figure 2-13. As it is well known that the resonance shift to a lower frequency is due an increase or addition in overall capacitance. The graphs agrees to the discussion that increasing L_{i1}, L_{i2} and decreasing the gap increases the capacitance and increasing W_{i1} increases overall grid inductance. Increasing the gap after a certain point doesn't affect the resonance. However the periodicity increases with increasing gap [103].

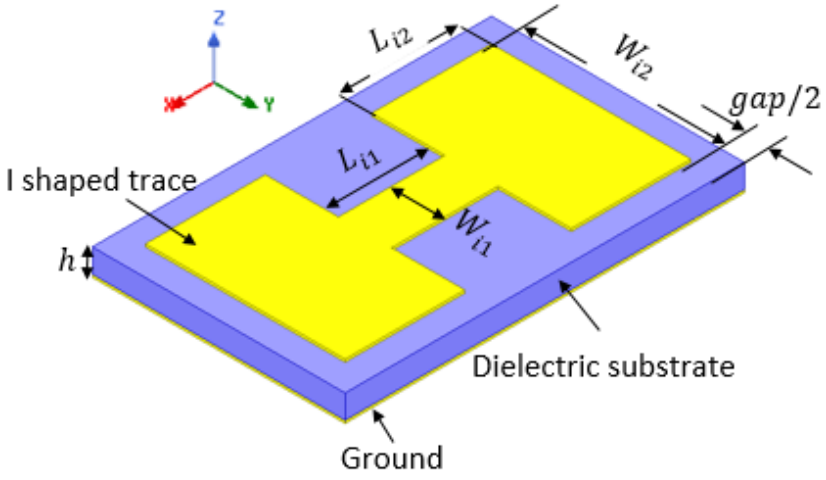

L_{i1}	8mm
W_{i1}	4mm
L_{i2}	9mm
W_{i2}	14mm
gap	0.5mm

Figure 2-12: I shaped AMC unit cell and its dimensions

Now in order to calculate the parameters for the equivalent circuit, from the design we observe that the I-shape has inductance that is contributed by L_{i1} and W_{i1} and dimensions L_{i2} and W_{i2} and gap contributes to capacitance. To solve the inductance L_g, the l in Eq. (2.11), is L_{i1} and the width for calculating Z_0 is W_{i1}, the inductance L_g turns out to be 1.2nH. For the gap capacitance C_{ga}, we use Eq. (2.5), here the d is W_{i2} and the width for Z_0 is L_{i2}. Substituting these values in Eq. (2.5) we get the value of C_{ga} as 1.25pF. Similarly the fringing capacitance C_f and the capacitance due to the conducting materials (AMC trace and the ground) C_{gd} can be calculated using Eq. (2.8) and Eq. (2.10), whose values are 0.25pF and 0.31pF respectively. Now adding all these capacitances gives the overall value of C_g as 1.834pF. Now once we have all the values to the circuit. The resonant frequency where zero phase occurs can be calculated from Eq. (2.18) as 2.506GHz.

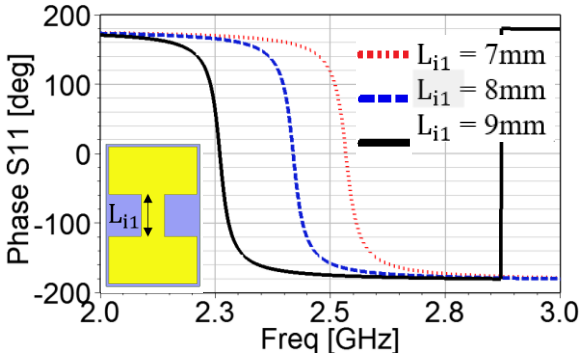

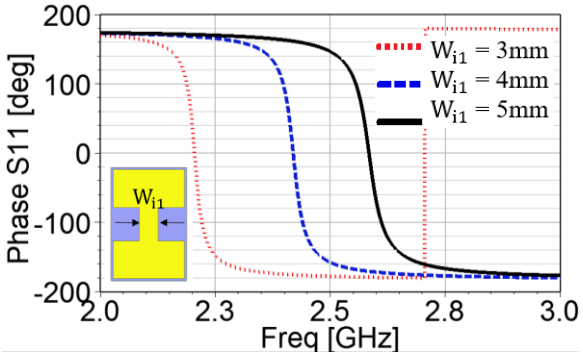

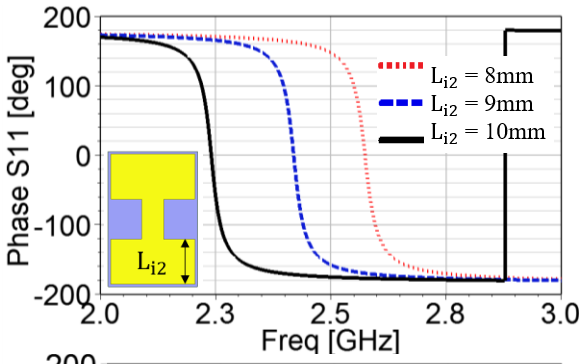

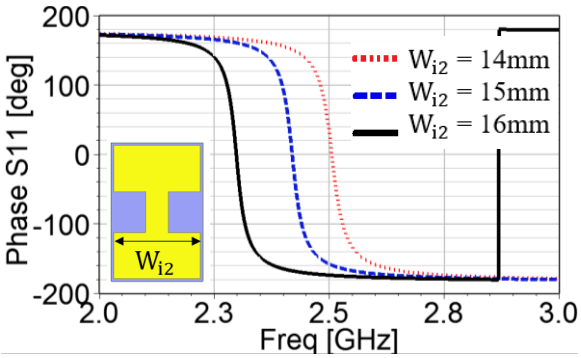

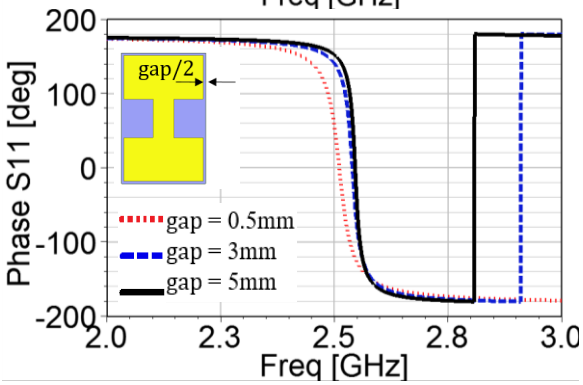

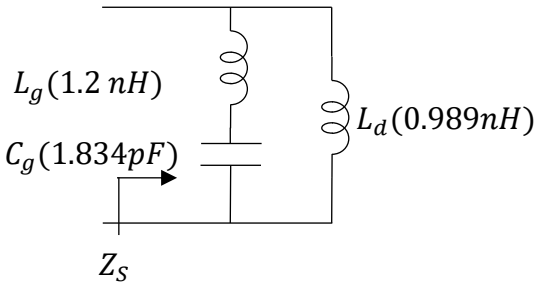

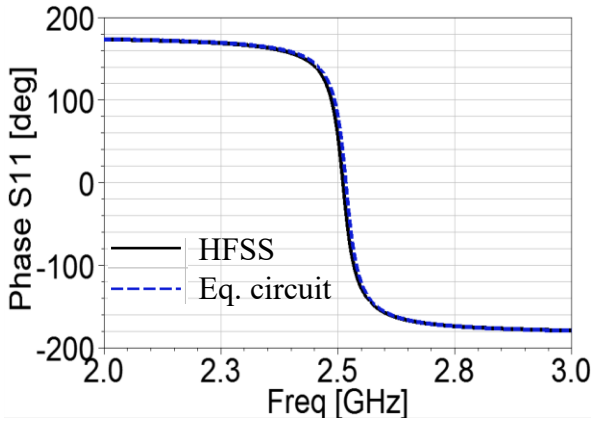

Figure 2-13: S11 Phase in degrees with varying dimensions for I shaped AMC with the equivalent circuit model for the dimensions given.

2.1.4. Jerusalem Cross

Jerusalem cross is similar to I shaped unit cell with an additional I shaped structure in the y direction. Since increasing the dimension L_{j2} or W_{j2} will cause the layers to merge and make the design alter altogether. I shaped design was achievable as the dimensions varied in one direction.

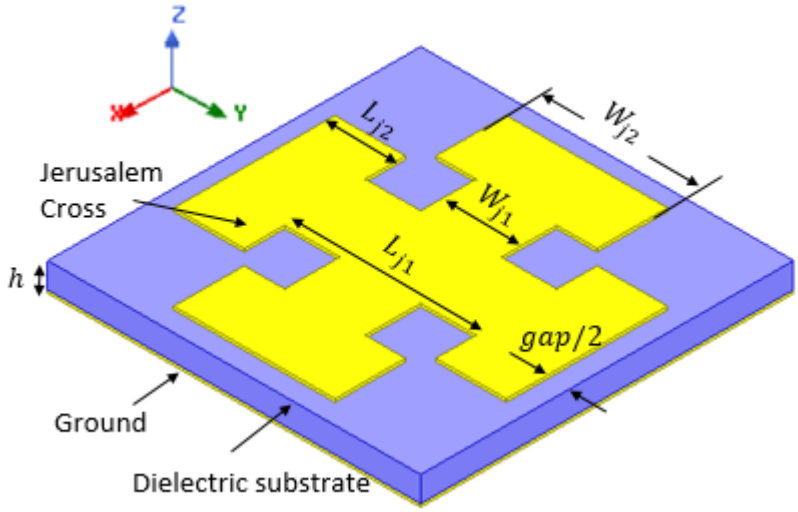

L_{j1}	19mm
W_{j1}	8mm
L_{j2}	7mm
W_{j2}	16mm
gap	0.5mm

Figure 2-14: Jerusalem Cross (JC) AMC unit cell and equivalent circuit

Hence making sure they don't merge and miniaturizing the unit cell was the challenge. The equivalent circuit again was referred from [96] which can be narrowed down to the LC resonant circuit given in Figure 1-4 and Figure 1-5. Overall the dimensions varying capacitance and inductance remain same as I shaped unit cell.

Now in order to calculate the parameters for the equivalent circuit, from the design we observe that the Jerusalem cross has inductance that is contributed by L_{j1} and W_{j1} and dimensions L_{j2} , W_{j2} and gap contributes to capacitance. To solve the inductance L_g, the l in Eq. (2.11), is L_{j1} and the width for calculating Z_0 is W_{j1}, the inductance L_g turns out to be 1.704nH. For the gap capacitance C_{ga}, we use Eq. (2.5) , here the d is W_{j2} and the width for Z_0 is L_{j2}.

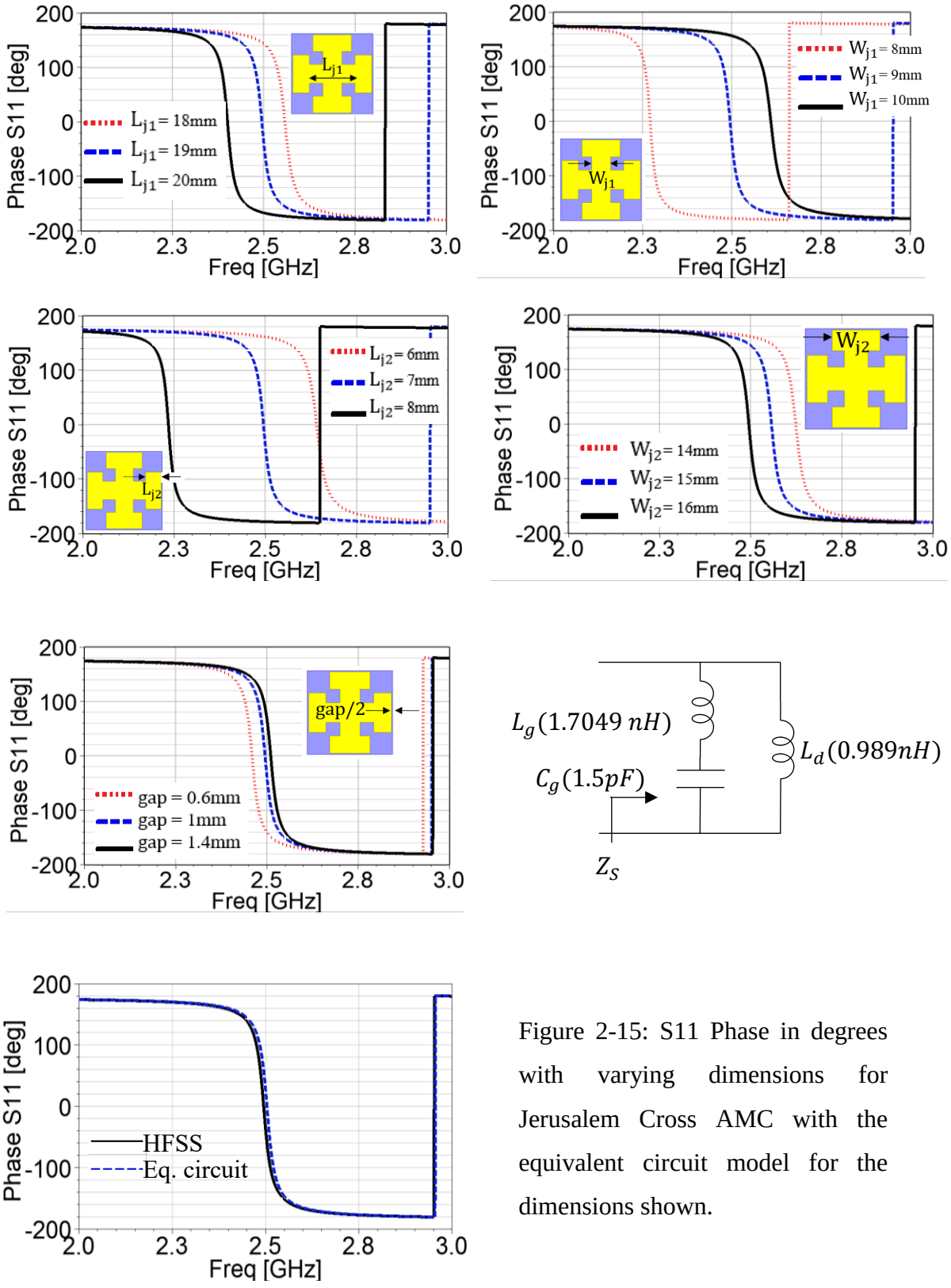

Figure 2-15: S11 Phase in degrees with varying dimensions for Jerusalem Cross AMC with the equivalent circuit model for the dimensions shown.

Substituting these values in Eq. (2.5) we get the value of C_{ga} as 0.9863pF. Similarly the fringing capacitance C_f and the capacitance due to the conducting materials (AMC trace and the ground) C_{gd} can be calculated using Eq. (2.8) and Eq. (2.10), whose values are 0.245pF and 0.2694pF respectively. Now adding all these capacitances gives the overall value of C_g as 1.5pF. Now once we have all the values to the circuit. The resonant frequency where zero phase occurs can be calculated from Eq. (2.18) as 2.5028GHz.

2.2. Linear Monopole Antenna

Various printed monopole antennas are reported in literature [88], [104]–[107]. Monopole antennas are usually designed to be operated as wideband antennas. Thorough research is still going on to make the antenna's bandwidth as wide as possible for the demand in growing cellular and wireless data, as mainly the printed monopole antennas work in wireless communication.

The antenna is to be designed on Rogers RT/duroid 5880™ with a dielectric constant of 2.2 and tanδ of 0.0009. The first step is to see whether the height of the substrate will give rise to surface waves in the operating frequency band.[104]

$$f_c = \frac{c}{4h\sqrt{\epsilon_r - 1}} \qquad \text{Eq. (2.17)}$$

where f_c is the cut off frequency for the surface waves to occur. The height (h) of 31 mils used in the thesis gives rise to the cutoff frequency of 86.95 GHz, which far beyond the operating frequency band of 2.4-2.5GHz.

The antenna dimensions can be found from [104], [105], [108] where the lower operating frequency f_l is defined as,

$$f_l = \frac{0.24c}{L + r} \qquad \text{Eq. (2.18)}$$

where L is the length of the radiator and r is the radius of an equivalent cylindrical monopole antenna. To calculate the equivalent radius r for a planar monopole antenna, its area is considered to be equal to the area of the side of a cylindrical monopole of radius r. If the width of the radiator is W then,

$$2\pi rL = WL \quad \text{or} \quad r = W/2\pi \qquad \text{Eq. (2.19)}$$

Due to the effect of the substrate on the monopole Eq. (2.18) now becomes

$$f_l = \frac{0.24c}{k(L + r + p)} \qquad \text{Eq. (2.20)}$$

Where p is the length which is added to increase the bandwidth and the correction factor k=1.1 for the substrate used in this thesis.

The beveling angle α is used to increase the bandwidth of the antenna as reported in [105], [108]. The bevel angle used in the in antennas throughout the thesis is in the range of $10^0 - 15^0$. This value doesn't increase the bandwidth much. However the bandwidth of the antenna will be affected depending on the bandwidth of the AMC that will be placed below it. The first monopole antenna we will be looking at has a beveling angle of 13.5^0 and the second antenna does not have any.

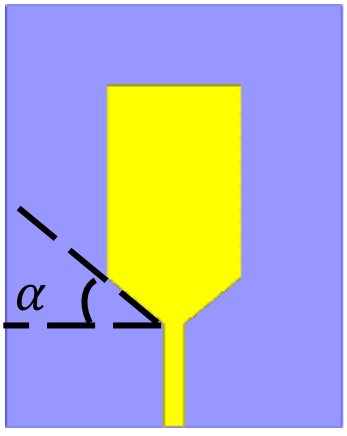

Figure 2-16: beveling angle of a monopole antenna

2.2.1. Microstrip Feed Monopole Antenna

Antenna 1:

A_y	30 mm
A_y	40mm
M_l	20.5mm
M_w	12 mm
msl	11 mm
msw	2.42 mm
t_p	1.15 mm
gnd	9.5 mm

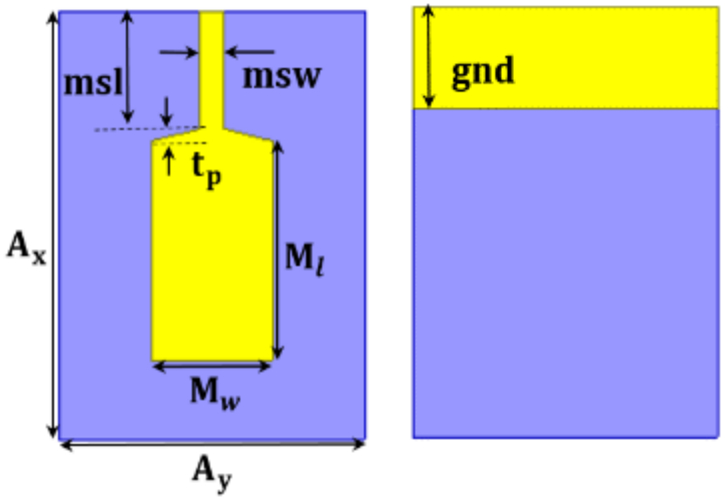

Figure 2-17: Antenna 1 parameters and dimensions

The antenna designed from Eq. (2.20) has resulted in the lower frequency of 2.73GHz. Where L in the equation is $M_l = 20.5mm$ and W in the equation is $M_w = 12mm$ and p is the difference of msl and gnd which turns out to be 1.5mm. Entering all these values in Eq. (2.20) gives us a lower frequency band of 2.73GHz, which is pretty close to the HFSS 10dB lower frequency of 2.8GHz. The above antenna was also used in paper [88]

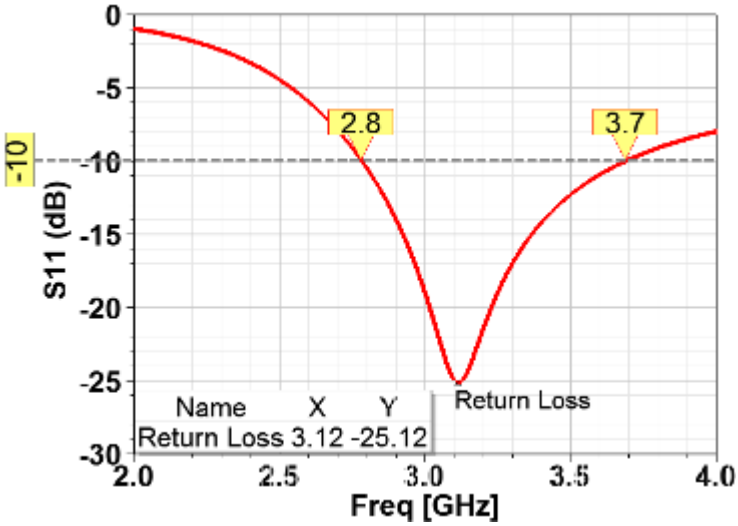

Figure 2-18: Return loss for Antenna 1

Antenna 2:

A_{y2}	30 mm
A_{x2}	40mm
M_{l2}	5mm
M_{w2}	5 mm
msl2	29 mm
msw2	2.42 mm
gnd2	14.5 mm

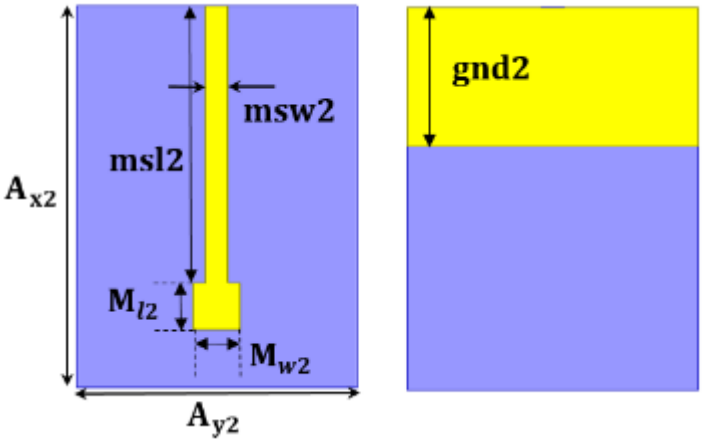

Figure 2-19: Antenna 2 parameters and dimensions

The second antenna is similar to the printed square monopole antenna without the beveling angle in antenna 1. The difference in square monopole antenna is that W is replaced with L in Eq. (2.20). Since we have not included the beveling angle, we can see the difference in the bandwidth, where Antenna 2 has a lower 10dB bandwidth compared to Antenna1. The advantage of Antenna 2 over Antenna 1 is that the smaller patch area with a longer feed can be easily tweaked and incorporated in wearables.

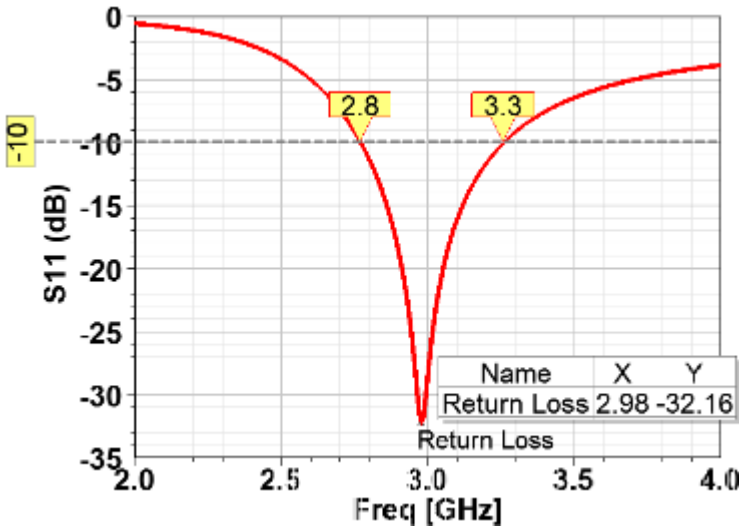

Figure 2-20: Return loss for Antenna 2

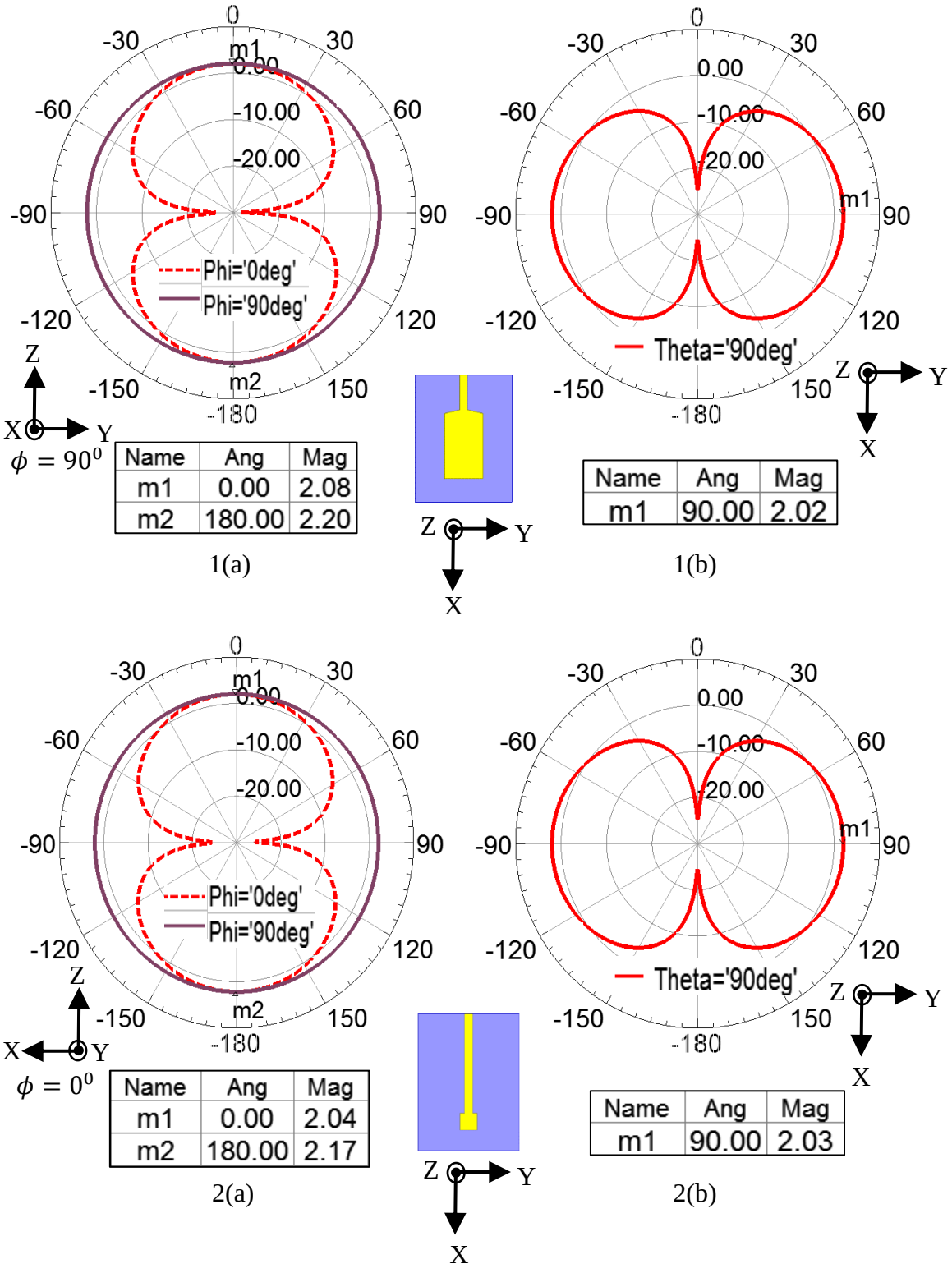

Figure 2-21: Comparing Radiation patterns for Antenna 1 and Antenna 2 at 2.45GHz; a) Elevation planes $\phi = 0^0$ (XZ plane) and $\phi = 90^0$ (YZ) plane b) Azimuth plane $\theta = 90^0$ (XY) plane

2.2.2. Antenna with Complete Ground plane

As we all know metal conductors are excellent reflectors. However the phase reversal of the waves causes the near field waves to cancel each other leading to a broadside pattern, without gain enhancement. When the monopole antennas 1 and 2 discussed above are forced to a complete ground plane, we notice that the gain in the negative z direction is reflected without enhancing the gain in the positive z direction. Antenna 1 and 2 both show similar patterns.

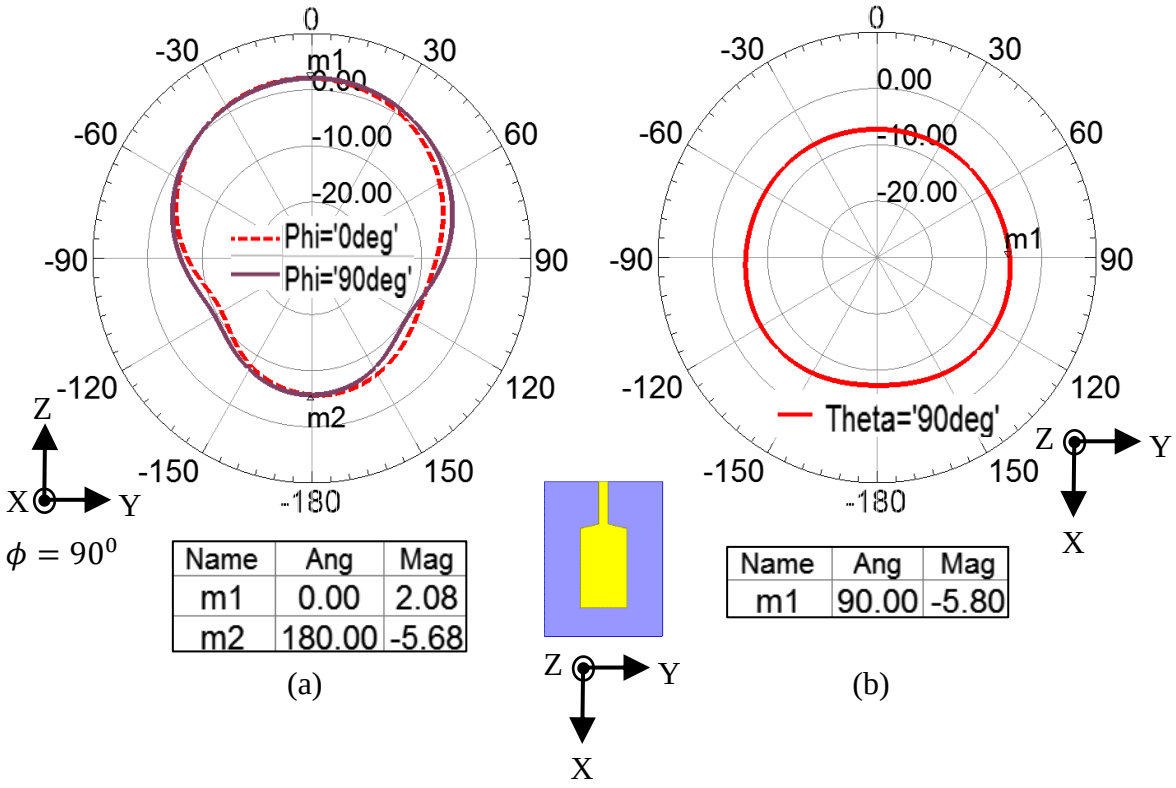

Figure 2-22: Radiation patterns for Antenna 1 with complete ground plane; a) Elevation planes $\phi = 0^0$ (XZ plane) and $\phi = 90^0$ (YZ) plane b) Azimuth plane $\theta = 90^0$ (XY) plane

Figure 2-22 and Figure 2-23 agrees to the theory of placing a complete metal conductor at the bottom. In fact, when compared to free space and complete ground plane, for Antenna 1 the front to back ratio increases from 1.027 to 5.88 and for Antenna 2 from 1.05 to 5.47. This is also one of the way of knowing that the back radiation has reduced.

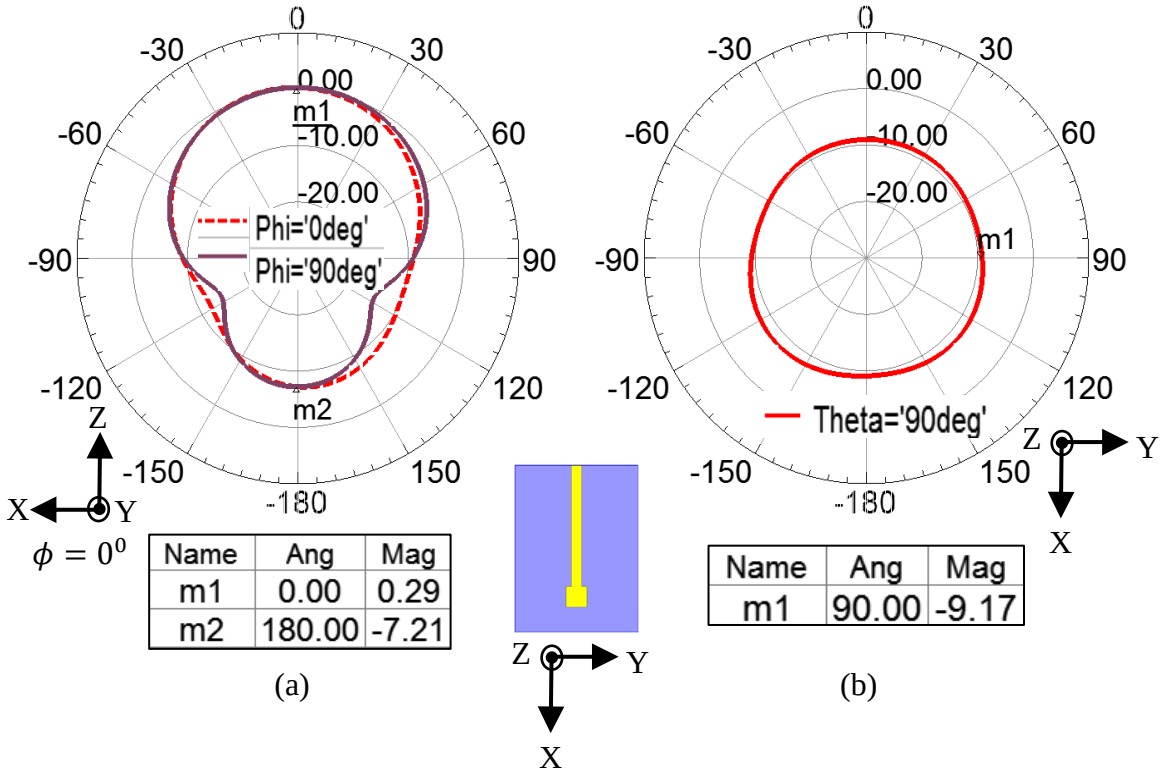

Figure 2-23: Radiation patterns for Antenna 2 with complete ground plane; a) Elevation planes $\phi = 0^0$ (XZ plane) and $\phi = 90^0$ (YZ) plane b) Azimuth plane $\theta = 90^0$ (XY) plane

These complete ground plane antennas have a very bad return losses when compared to no ground plane. The reason is as they were not designed for complete ground plane, the same antenna in free space was forced with ground plane to observe the radiation patterns. However when these antennas were to be designed for complete ground plane, the size of the antenna will increase making it non- feasible when our aim is to achieve a small sized antenna. Moreover, the purpose of designing the antennas higher that the operating frequency range is to achieve a good impedance match with the inductive ground planes, as these antennas will present themselves with a capacitive property. Maximum coupling occurs when the antennas are placed at the center of the AMC. The process of designing the integrated antenna is discussed in detail in the following section for one particular AMC and a summary of different AMC on the same antenna.

3. Analysis of Integrated Antennas

3.1. Linear Monopole Antenna with AMC1 as the Ground

Overview: Initially Antenna 1 is simulated on AMC1 (rectangular patch 2x2 array), where a step by step modelling of the integrated antenna is discussed. All other configurations follow the same procedure, therefore only the final on arm analysis has been discussed for them.

3.1.1. Free Space: Case 1

Case 1: This case is the first step of analyzing the antenna and AMC together that were designed earlier. The dimension and the type of Antenna and AMC used is shown in Figure 3-1. The antenna is placed on top of the AMC with the air gap of 31mils and the position of the antenna in the x-axis with respect to the AMC is D_x= 10mm. As discussed earlier, antenna has the strongest radiating slot located at the center of the AMC. Hence the antenna is moved along the x direction to locate the exact resonance.

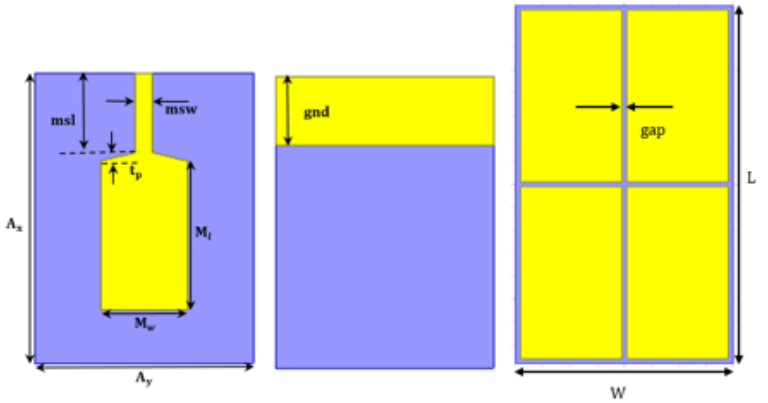

M_w	12 mm
M_l	21.8 mm
msw	2.42 mm
msl	11.4 mm
tp	1.15 mm
gnd	10 mm
A_x	39 mm
A_y	30 mm
L	78mm
W	40 mm
gap	1 mm

Figure 3-1: Dimensions of the antenna and the Rectangular Patch 2x2 array AMC

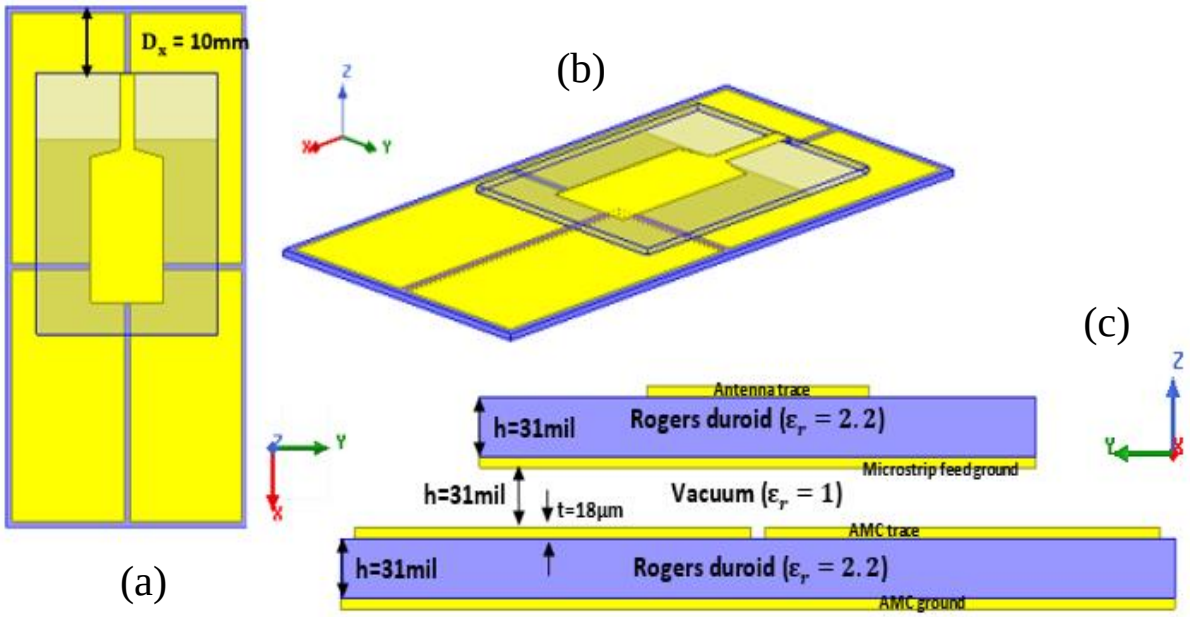

Figure 3-2: (a) Top view with D_x=10mm (b) 3D view (c) Case 1: Stack-up (Front view)

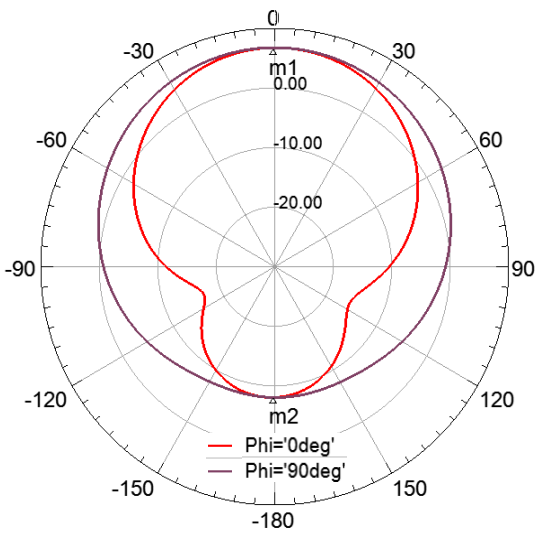

Name	Theta	Ang	Mag
m1	0.00	0.00	6.76
m2	180.00	180.00	-8.05

(a)

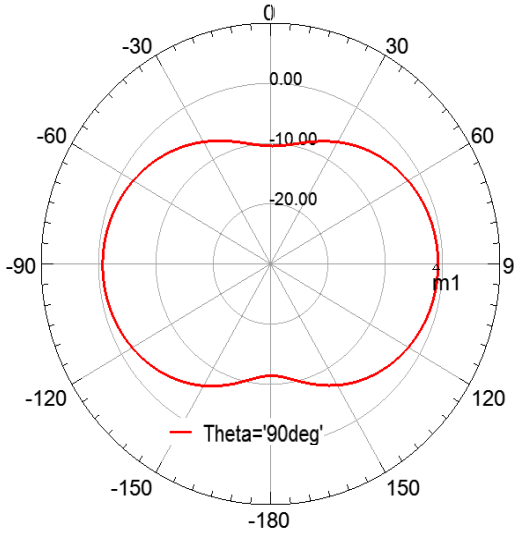

Name	Phi	Ang	Mag
m1	90.00	90.00	-0.80

(b)

Figure 3-3: Case 1: Gain in (a) Elevation plane (b) Azimuth plane

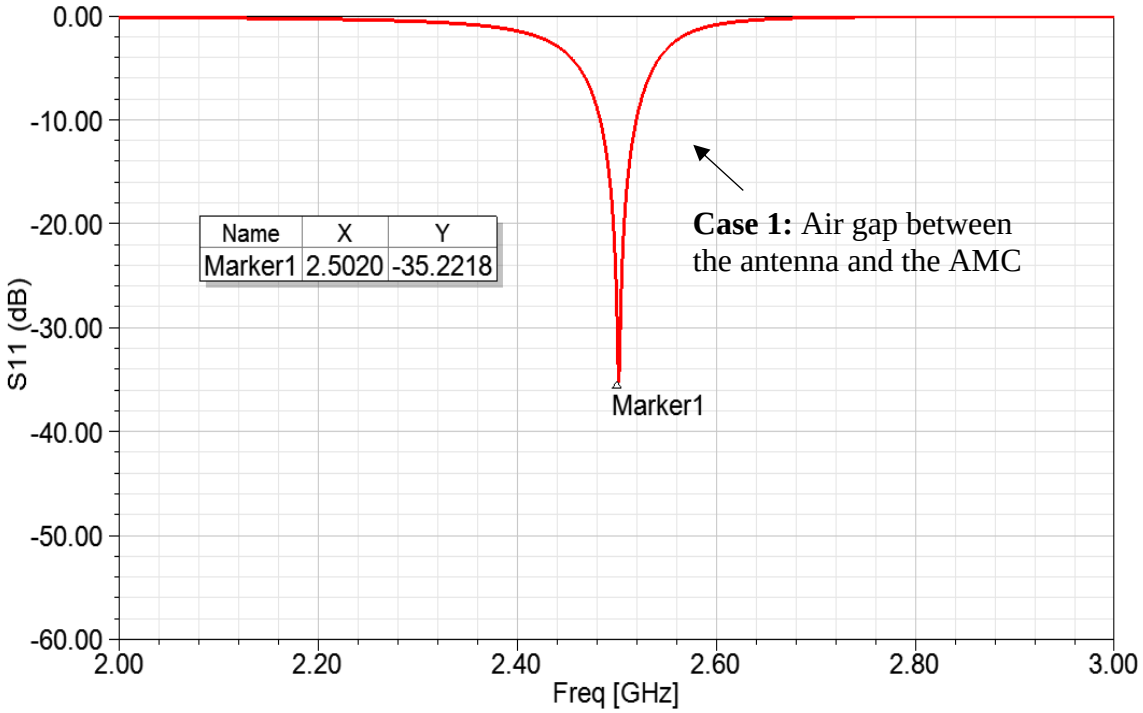

Figure 3-4: Return Loss in dB for Case 1, Model 1

The results of the proposed setup was run in HFSS and the results are discussed. The return loss was achieved as -35.22dB at 2.502GHz which was achieved by adjusting D_x. The broadside gain achieved was 6.76dB which has definitely enhanced the front radiation when compared to the complete ground plane of the antenna used. This setup also achieved a better front to back (FB) ratio of 30.17 at 2.45GHz with the radiation efficiency of 91.16%.

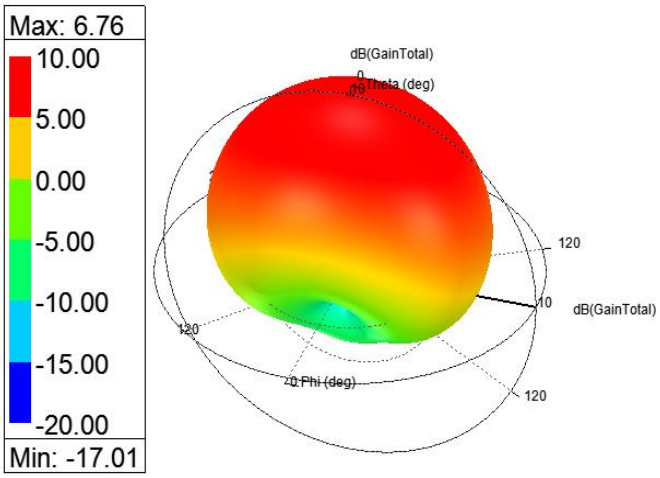

Figure 3-5: 3D Gain pattern in dB (Case 1-Model 1)

3.1.2. Radome and Substrate loading: Case 2-5

Case 2: Since it is difficult or rather impossible to keep the air gap between the antenna and the AMC in reality and have them tested. Hence the same substrate that was used in the antenna was loaded between the antenna and the AMC to keep the integrated antenna in place. The setup is shown in Figure 3-6. In Case 2 nothing was tuned and all the dimensions are same as is in Case 1. The dimension of the substrate loaded is the same as that of the antenna and is placed exactly below the antenna. This setup also aids in isolation between the feed ground and the AMC metal traces.

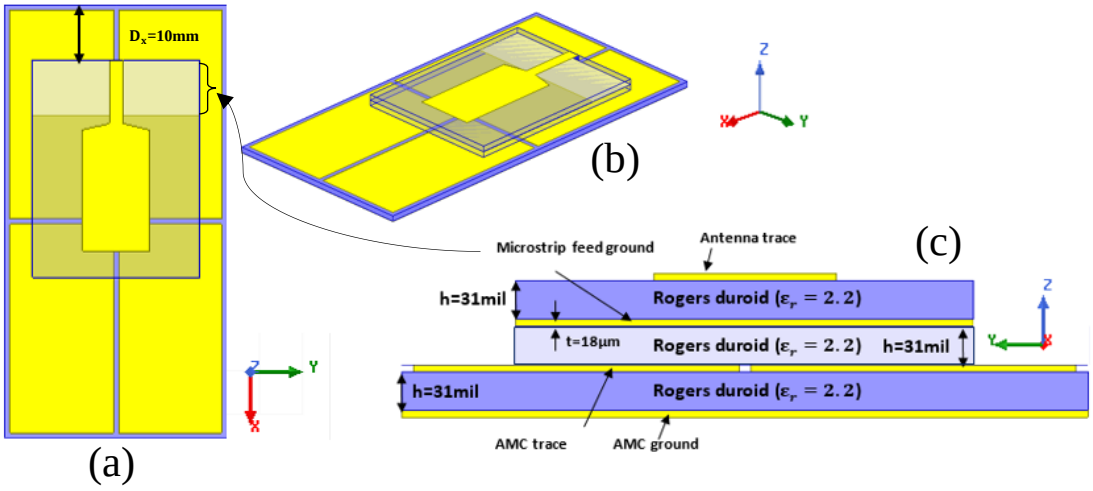

Figure 3-6: (a) Top view with D_x=10mm (b) 3D view (c) Case 2: Stack-up (Front view)

Loading the gap with substrate has affected the impedance matching which gave a return loss of -16.8dB and the frequency dropped from 2.502GHz to 2.407GHz. This accounts to a frequency difference of 95MHz. The shift in frequency assures that we are in the right path, as the antenna is responding or is rather sensitive to capacitive loading.

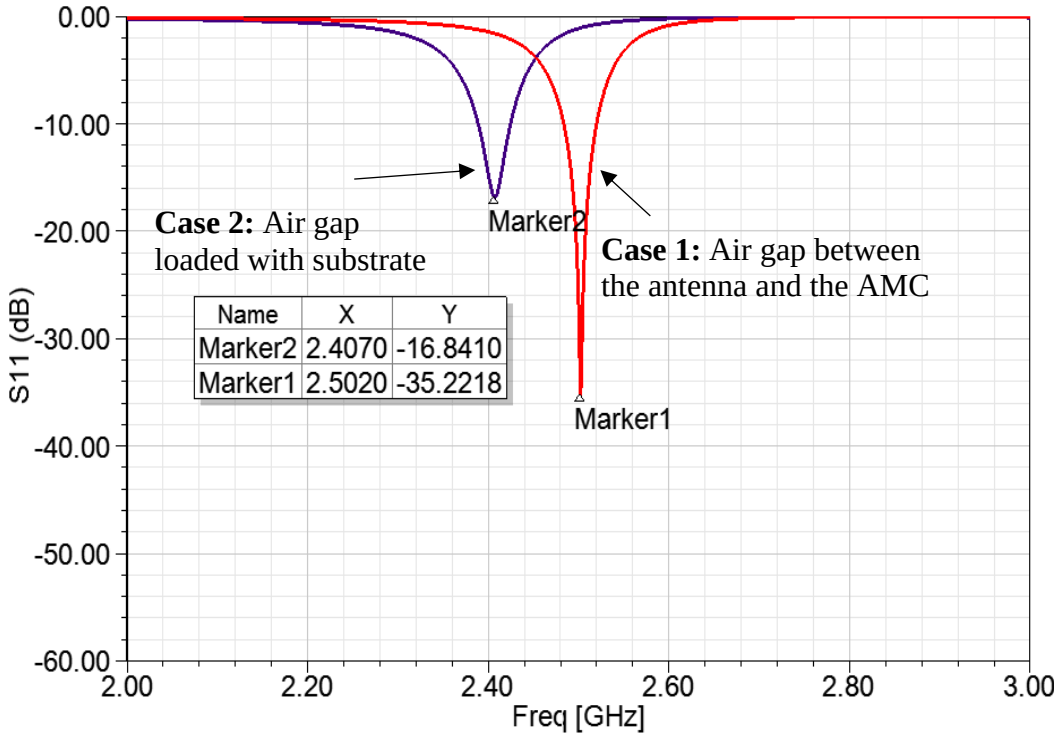

Figure 3-7: Comparison of Return Loss in dB for Case 1 and 2, Model 1

Additionally, FB ratio drops to 20.3 and also the radiation efficiency has reduced to 80.88%, this is because the setup has a poor return loss compared to Case1. Figure 3-7 presents the how return loss is related in Case 1 and 2. The figure clearly shows that the resonant frequency has shifted to a lower frequency.

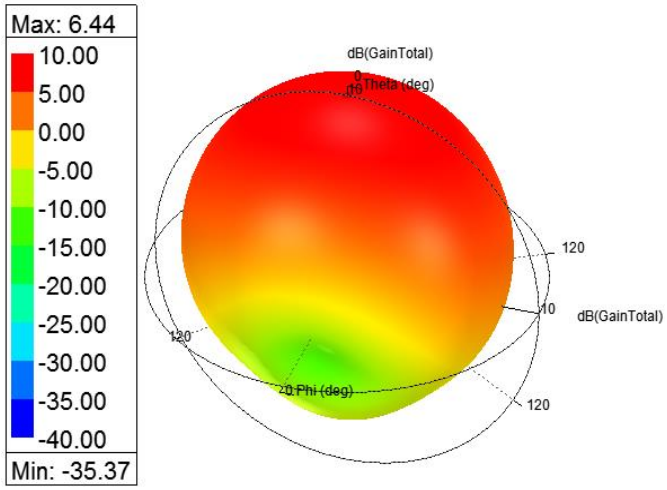

Figure 3-8: 3D Gain pattern in dB (Case 2-Model 1)

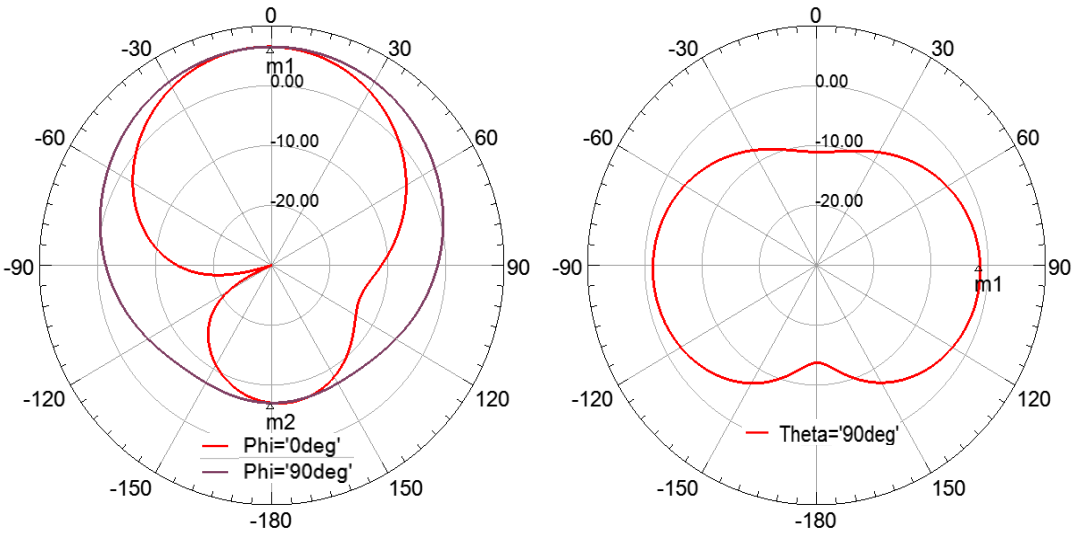

Name	Theta	Ang	Mag
m1	0.00	0.00	6.44
m2	180.00	180.00	-6.70

Name	Phi	Ang	Mag
m1	90.00	90.00	-1.47

(a) (b)

Figure 3-9: Case 2: Gain in (a) Elevation plane (b) Azimuth plane

Case 3: In this case we aim to match the integrated antenna to achieve a better return loss. Again the in order to obtain a good match the antenna along with the substrate below it, was moved along the x-axis to D_x= 9mm keeping the rest of the dimensions of the antenna and the AMC as is. No dimensions were touched except D_x was changed to attain a return loss of -48.17dB with the broadside gain showing no change. The results are shown in Figure 3-10, Figure 3-11 and Figure 3-12.

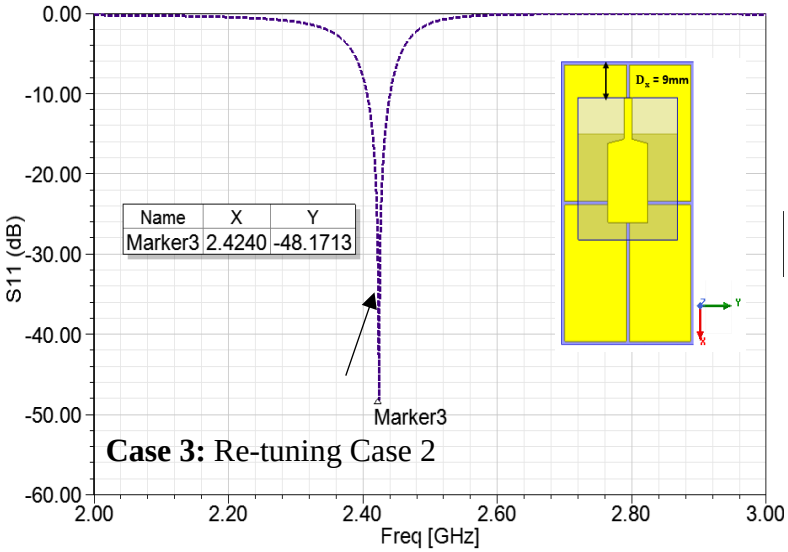

Figure 3-10: Return Loss in dB for Case 3, Model 1

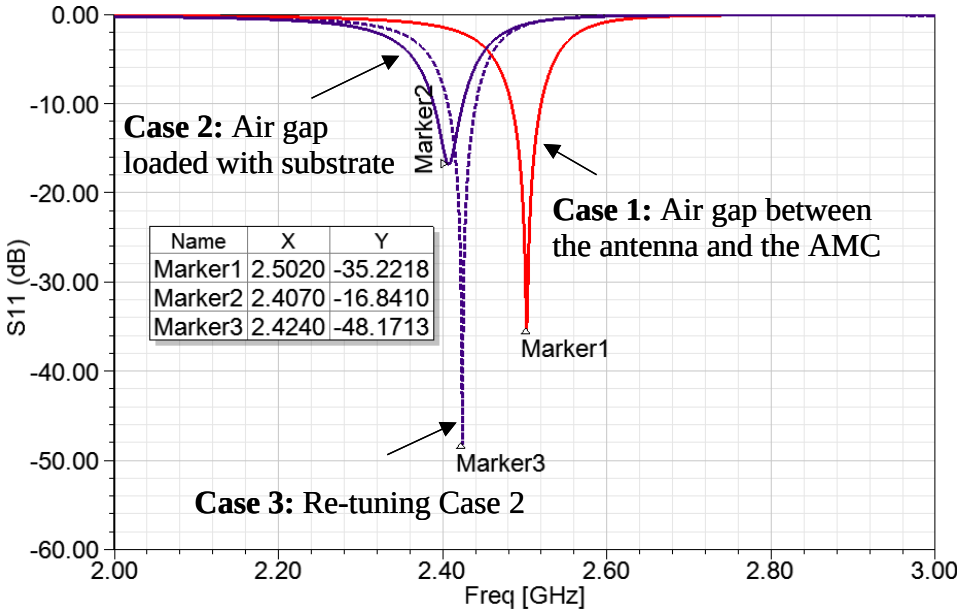

Figure 3-11: Comparison of Return Loss in dB for Case 1-3, Model 1

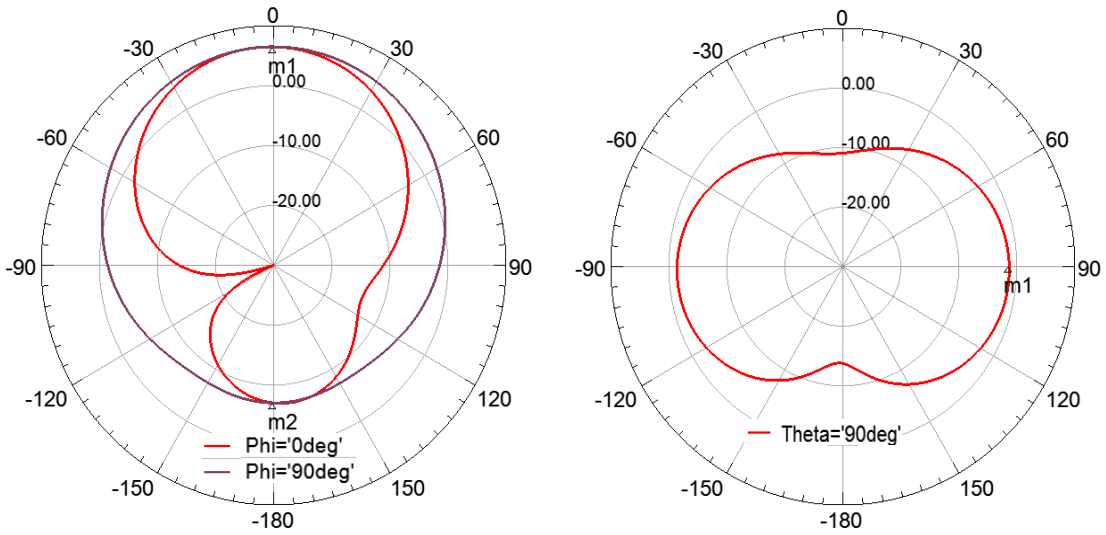

(a) (b)

Figure 3-12: Case 3: Gain in (a) Elevation plane (b) Azimuth plane

Case 4: Before we place the antenna with the AMC loaded with substrate on the arm to test it, we must isolate the antenna trace from touching the skin of the arm. Since our body is highly conductive and lossy, placing the antenna trace over the arm will cause the model to lose most of its power at the surface resulting in mismatch. For this reason, we use another layer of substrate (also known as a radome) that will help isolate the arm and the integrated antenna. The setup is shown in Figure 3-13

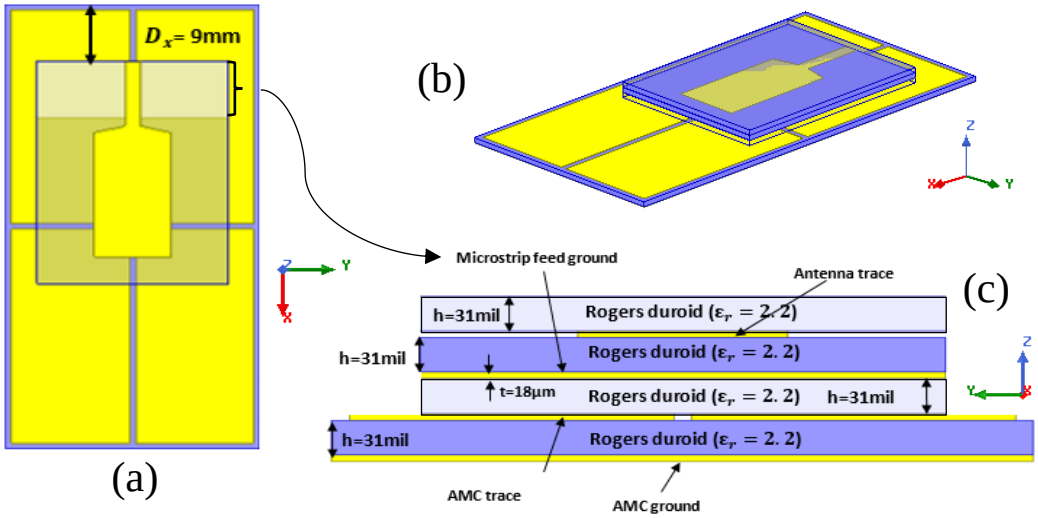

Figure 3-13: (a) Top view with D_x= 9mm (b) 3D view (c) Case 4: Stack-up (Front view)

From Figure 3-16, we can interpret that the resonance has shifted to the lower frequency from 2.424GHz to 2.4030GHz. This difference (21MHz) is less when compared to the difference (95MHz) caused in Case2. This is due to the change in effective permittivity, which is less in this case when compared to Case2.

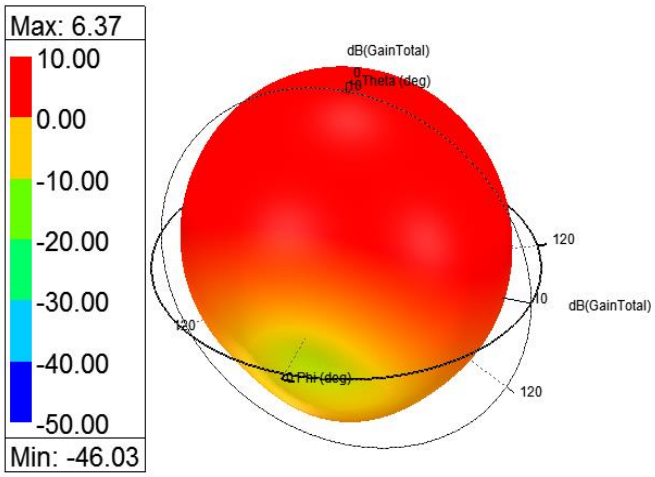

Figure 3-14: 3D Gain pattern in dB (Case 4-Model 1)

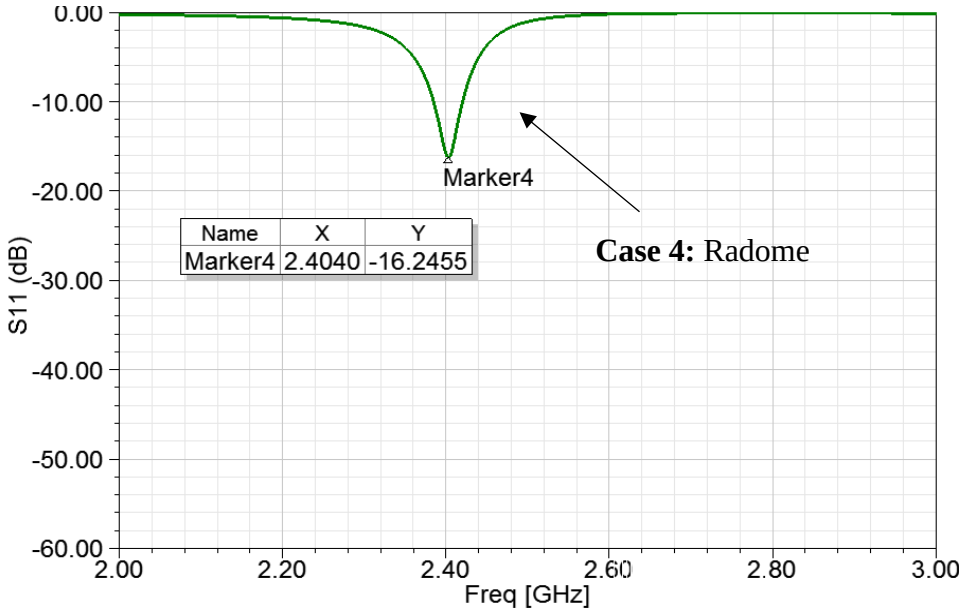

Figure 3-15: Return Loss in dB for Case 4, Model 1

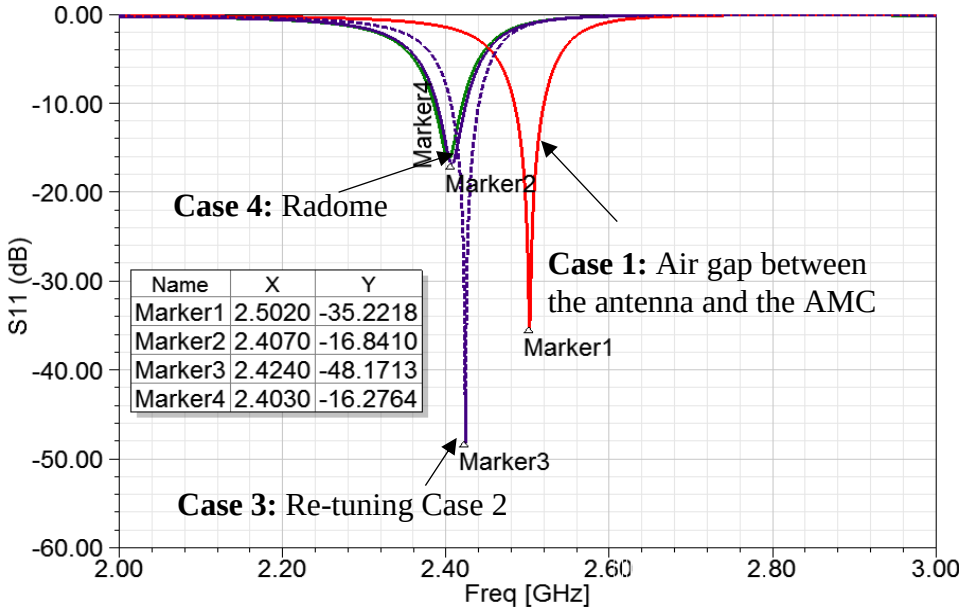

Figure 3-16: Comparison of Return Loss in dB for Case 1-4, Model 1

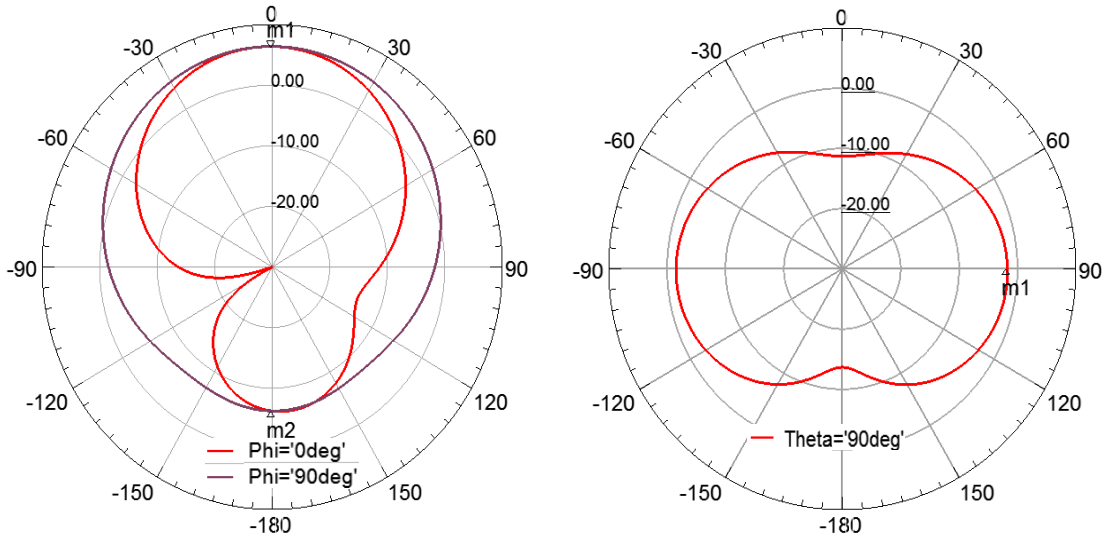

Name	Theta	Ang	Mag
m1	0.00	0.00	6.37
m2	180.00	180.00	-6.25

Name	Phi	Ang	Mag
m1	90.00	90.00	-1.72

(a) (b)

Figure 3-17: Case 4: Gain in (a) Elevation plane (b) Azimuth plane

Case 5: In this case the antenna is matched again by changing D_x and keeping the rest of the parameters as is. The return loss achieved in this case is -33.9dB

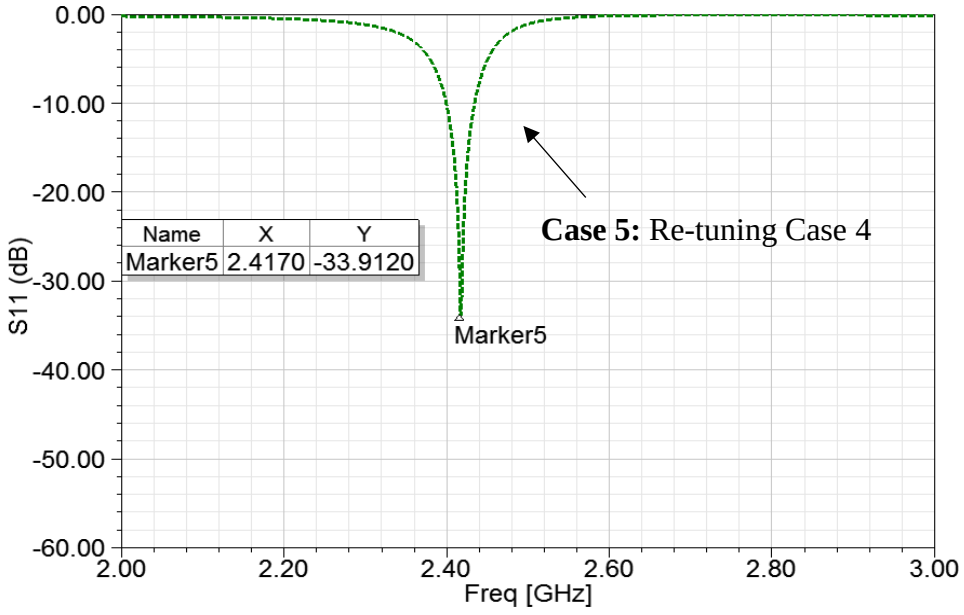

Figure 3-18: Return Loss in dB for Case 5, Model 1

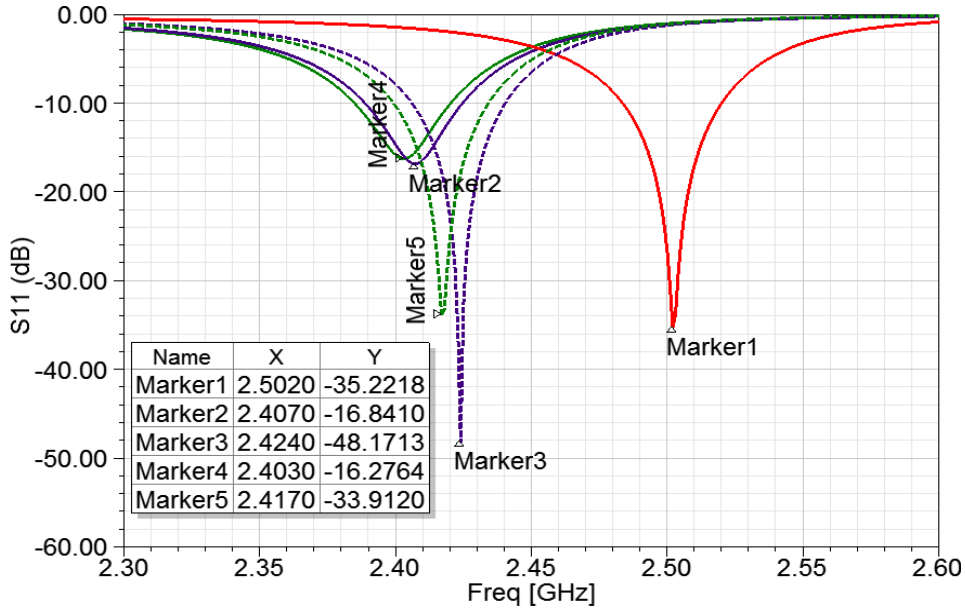

Figure 3-19: Comparison of Return Loss in dB for Case 1-5, Model 1 (Zoomed in)

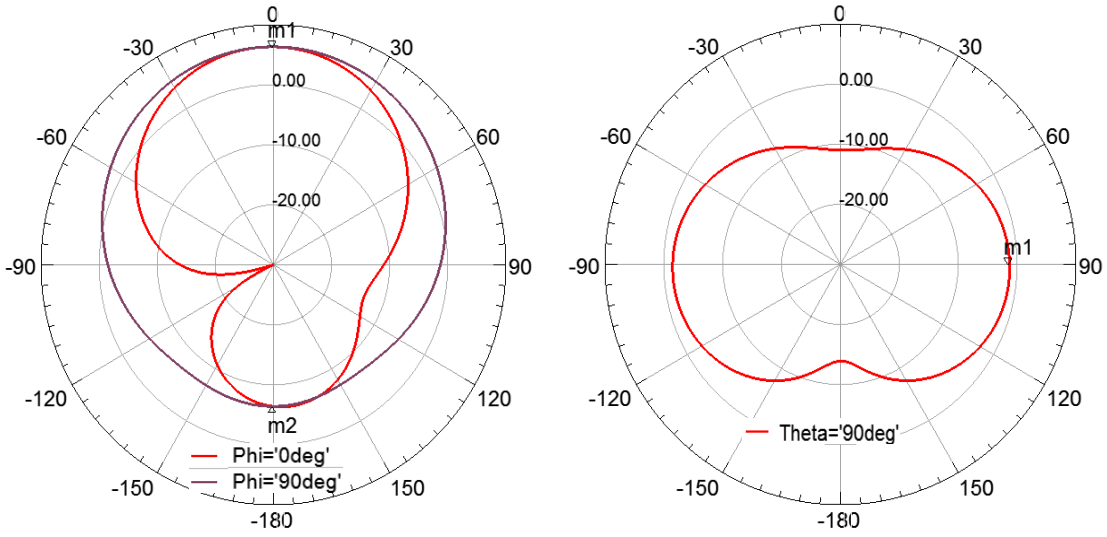

Name	Theta	Ang	Mag
m1	0.00	0.00	6.33
m2	180.00	180.00	-6.40

Name	Phi	Ang	Mag
m1	90.00	90.00	-1.26

(a) (b)

Figure 3-20: Case 5: Gain in (a) Elevation plane (b) Azimuth plane

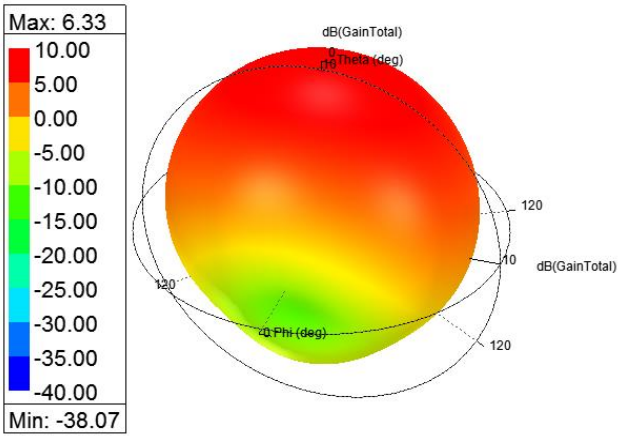

Figure 3-21: 3D Gain pattern in dB
(Case 5-Model 1)

Before moving to setup the integrated antenna used in Case 5, on arm, let us compare gain of antenna on its own, antenna with complete ground plane and the Integrated antenna designed in Case 5. Figure 3-22 and Figure 3-23 explains the radiation patterns in the E and H plane respectively. The results clearly shows that the back radiation is less when the antenna is placed over a metal conductor when compared to using the antenna on its own. The drawback is that due to the phase reversal of the ground plane, the radiation at the back is completely cut off also reducing the front gain, giving rise to destructive interference. Placing the antenna over the AMC layer not only reduced the back radiation but also enhanced the broadside radiation, giving a FB ratio of 18.6 with an efficiency of 80%. In comparison, the front to back ratio is 1.027 and 5.88 of antenna alone and antenna over a conducting metal respectively. This is the reason the antenna with the AMC layer was chosen over the electric conductor, and also as we wanted almost zero reflection at the back to avoid unnecessary fluctuations when monitoring blood glucose.

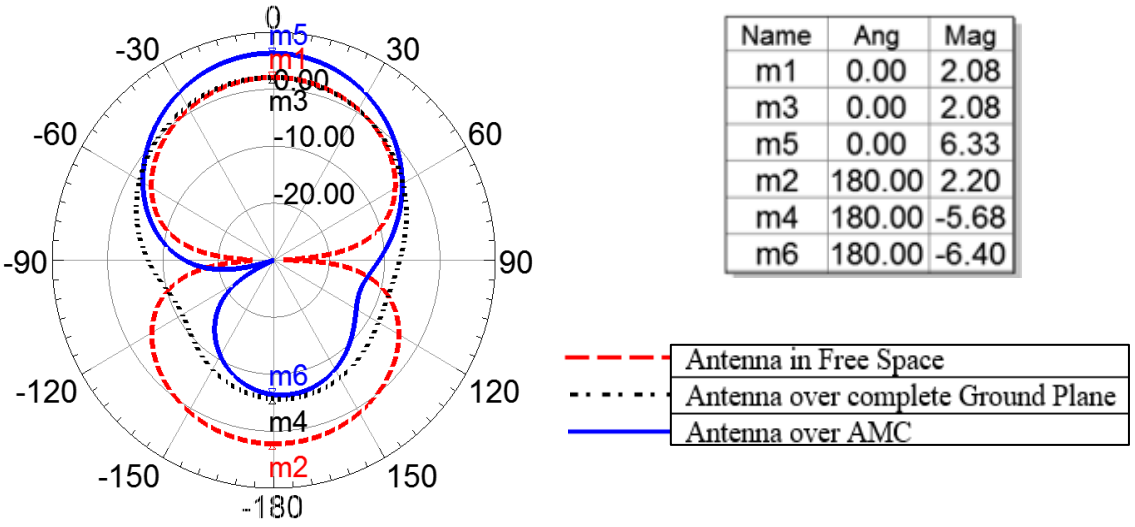

Figure 3-22: (Model-1): Gain in the E plane for Antenna alone, Antenna over PEC plane and Antenna over AMC

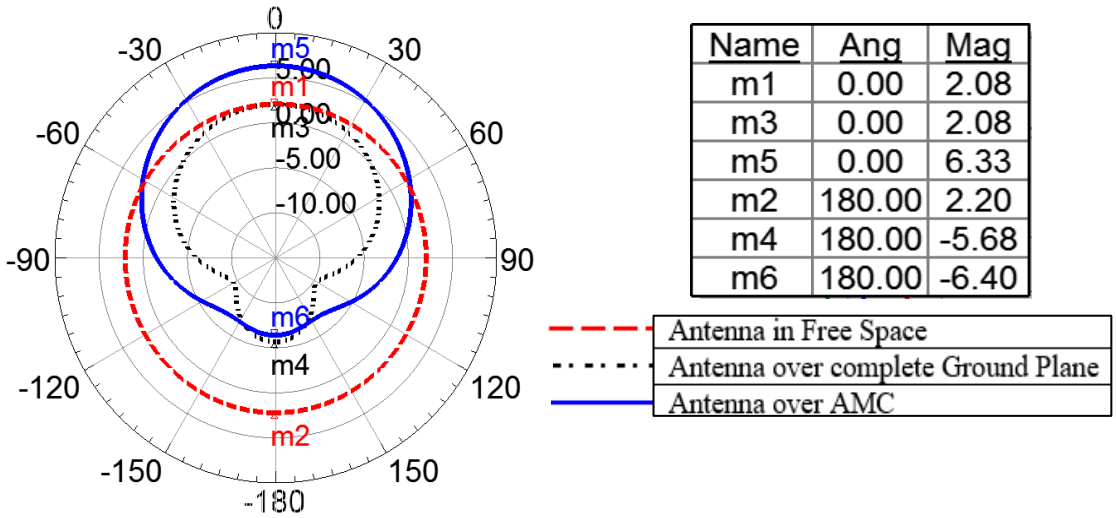

Figure 3-23: (Model-1): Gain in the H plane for Antenna alone, Antenna over PEC plane and Antenna over AMC

3.1.3. On Square Arm model: Case 6-7

Case 6: In this case we will be testing the integrated antennas on arm model that takes shape of a cuboid to be able to simulate the integrated antenna on a flat surface. The setup and the model specifications are shown in Figure 3-24 and Table 3-1.

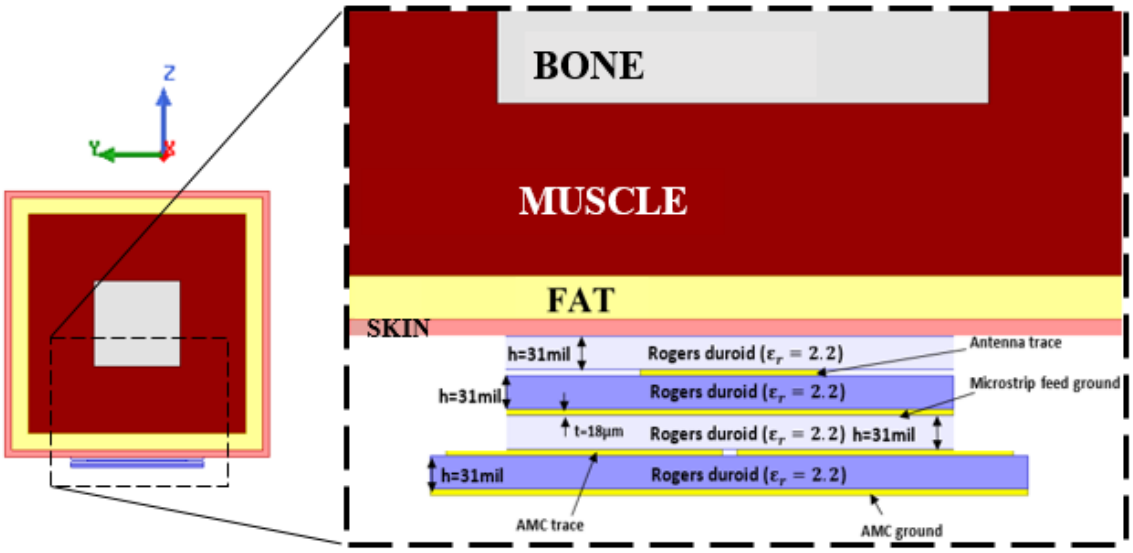

Figure 3-24: Integrated Antenna on Arm (Flat model) Case 6 and 7

Layers / Parameters	Skin	Fat	Muscle	Bone	Blood
Thickness (mm)	2	5	20	26	-
Relative Permittivity (ϵ_r)	38	5.28	52.7	18.5	58.3
Conductivity (σ)	1.47	0.105	1.74	0.807	2.55
tan (δ)	0.283	0.145	0.242	0.319	0.32
Penetration depth (mm)	22.5	117	22.3	28.7	16.1

Table 3-1: Dimensions and Electrical Properties of arm model at 2.45GHz [80]–[82]

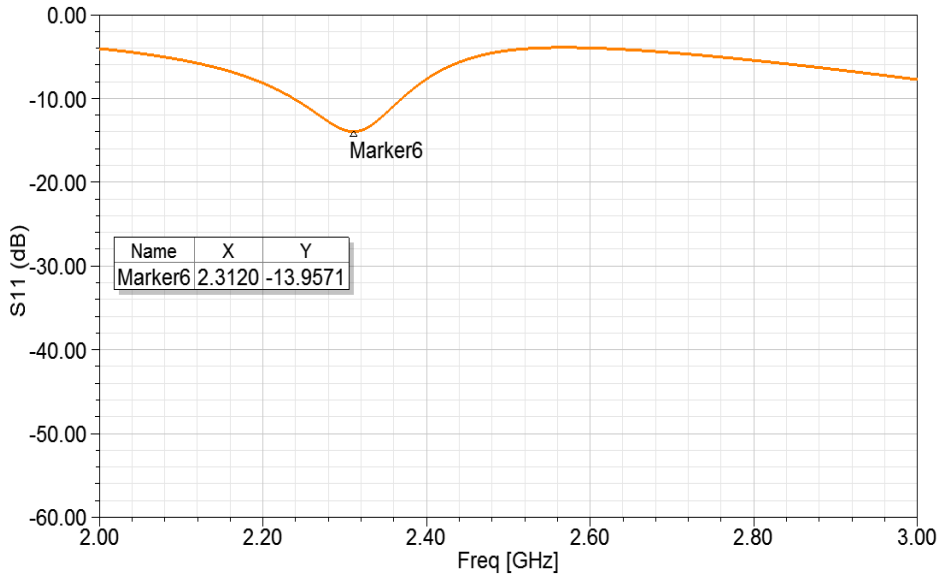

Figure 3-25: Return Loss in dB for Case 6, Model 1

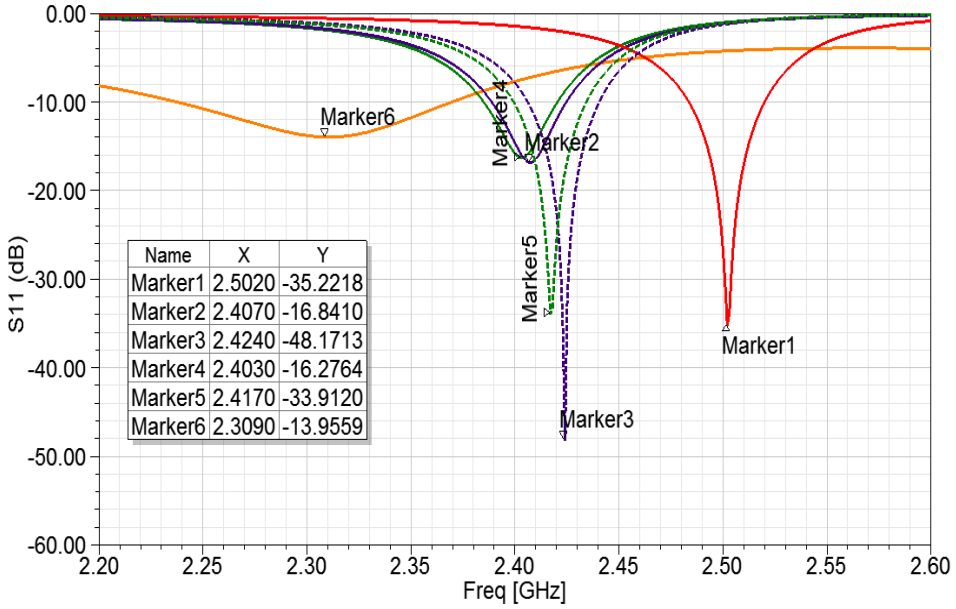

Figure 3-26: Comparison of Return Loss in dB for Case 1-6, Model 1 (Zoomed in)

The analysis shows that the frequency has shifted with a drop in return loss as well. The reason is because the body is lossy and conductive in nature. Once the antenna is placed on the arm the substrate causes the gap between the antenna trace and the arm causing it to be capacitive.

Capacitive, because the trace and the arm are conducting in nature. As the return loss has dropped tremendously. Let us tune the antenna in case7.

Case 7: In this case we will be retuning the integrated antenna simulated in case 6. Since the return loss achieved in case is very low and the integrated antenna resonates below the selected frequency band, the setup is tuned by varying the sized of the AMC and the position of the antenna over the AMC. From Figure 3-1 and Figure 3-2, the only dimensions that have changed are L=70mm and D_x= 8mm. The rest of the dimensions remain the same.

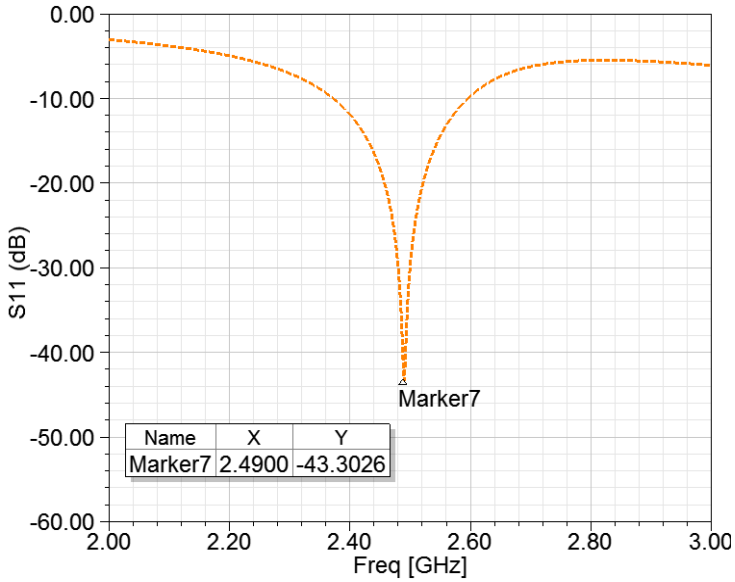

Figure 3-27: Return Loss in dB for Case 7, Model 1

E Field overlay has been shown in Figure 3-28, denoting that there is very less back radiation and most of the power is absorbed by the muscle (1/5th to 1/3rd of the power). From this result we can conclude that, there is E-field penetration in to the muscle. Since muscle has permittivity and conductivity very close to that of the blood (Table 3-1), and since blood is also contained in the muscle, antenna will respond to changes in the blood. In fact, the conductivity of blood being the highest it is most likely to absorb most of the power.

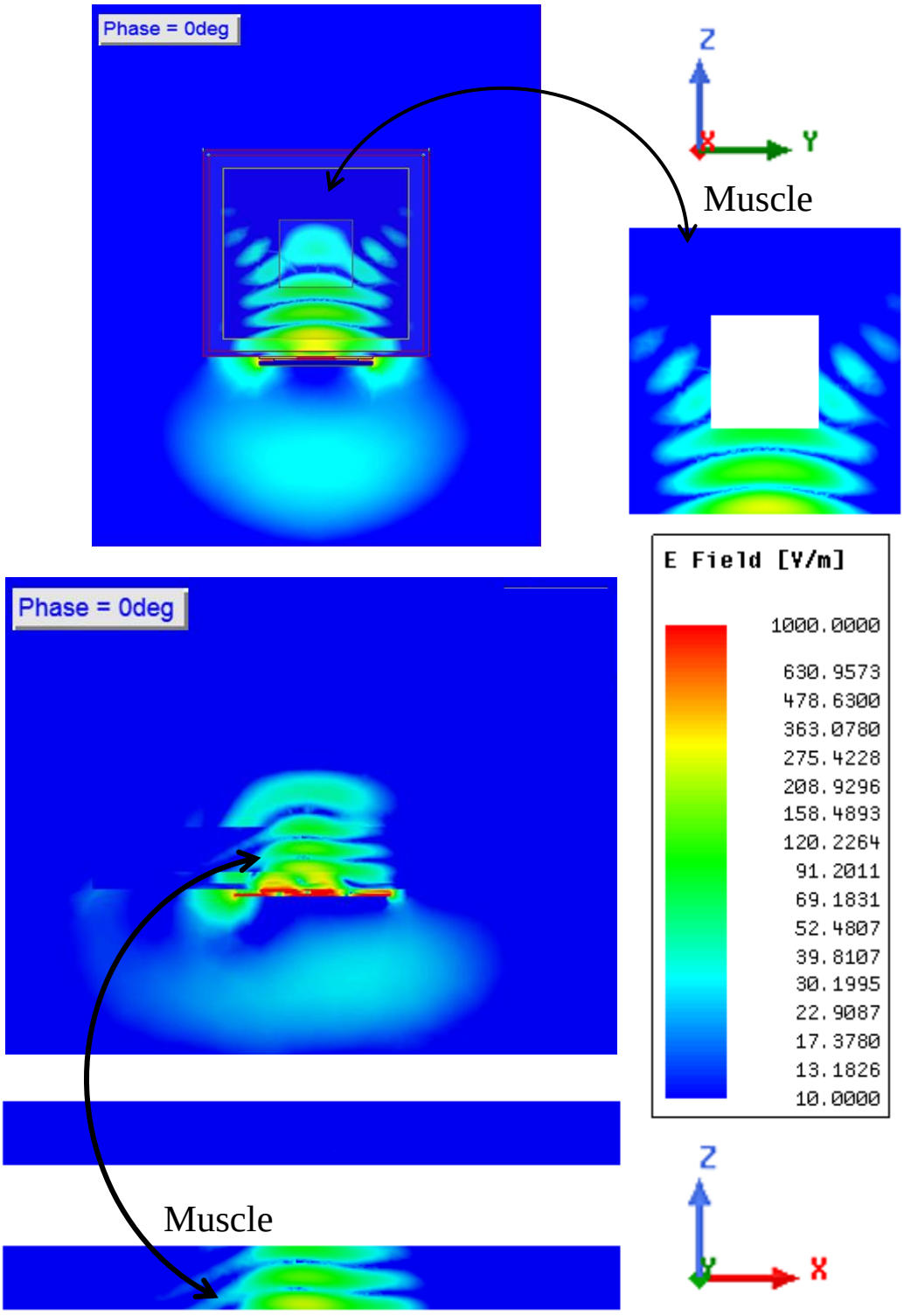

Figure 3-28: E Field overlay in YZ plane and XZ plane (Integrated antenna over cuboid arm)

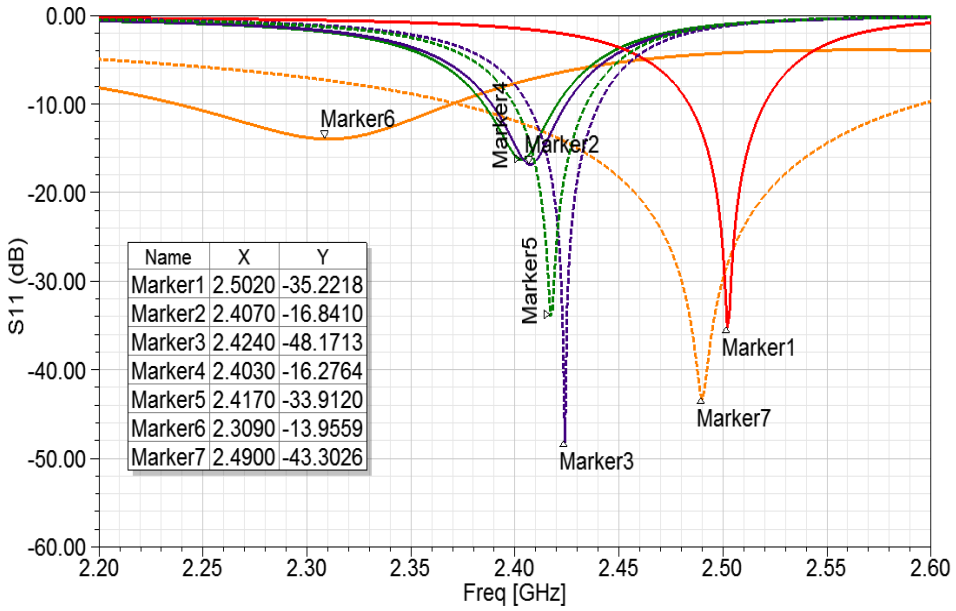

Figure 3-29: Comparison of Return Loss in dB for Case 1-7, Model 1 (Zoomed in)

3.1.4. Bending Effects on Arm

We already looked in to the antenna's response over the arm. In reality, since the arm's structure is not cuboid in shape, the antenna will be deformed to take the arm's shape. One of the major challenge is that restrict the antenna from being sensitive to bending. In order to observe the changes from flat surface to bend surface, the cuboidal arm model that was shown earlier is now modeled for a cylindrical shape, with the thickness of each layer same as in Figure 3-24. The return losses were compared between the flat arm and the cylindrical arm and we observe from Figure 3-30 that the bend had very minimal effect on return loss and no effect on resonance.

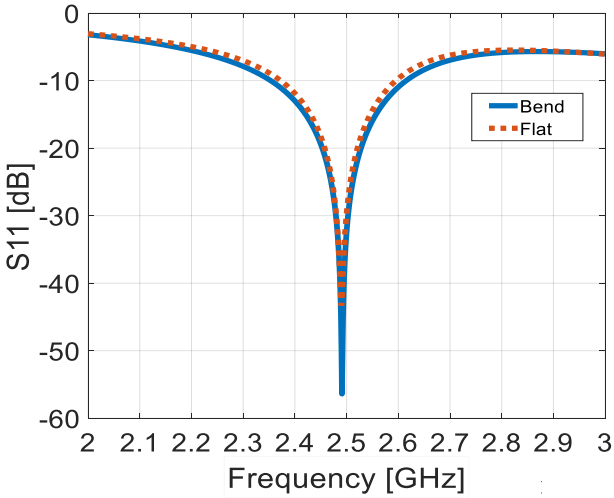

Figure 3-30: Bending analysis for Rectangular patch AMC.

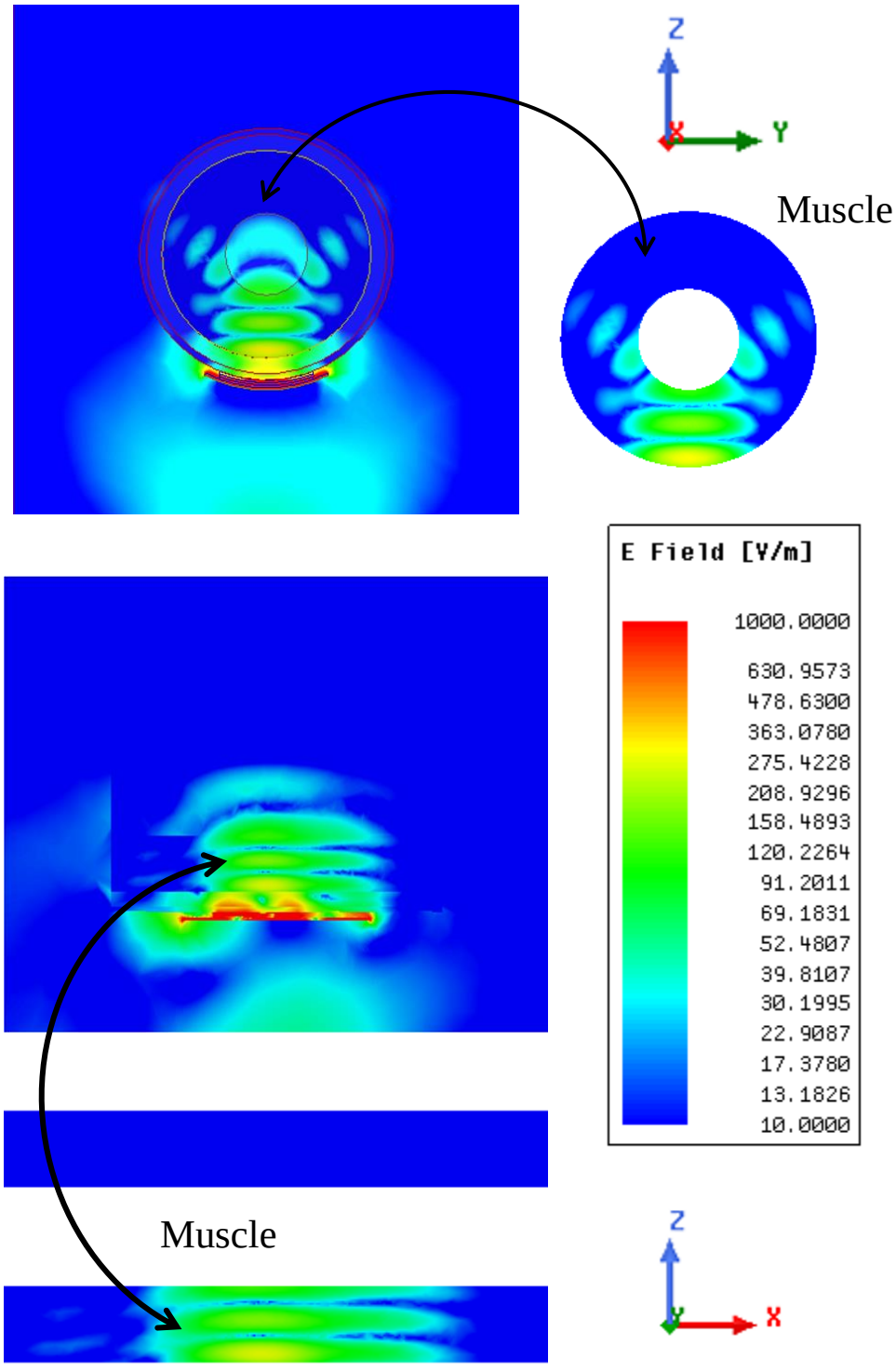

Figure 3-31: E Field overlay in YZ plane and XZ plane (Integrated antenna over cylindrical arm)

Now that we saw the step by step analysis of antenna with the rectangular patch AMC. Let us look at other AMCs. Placing the substrate between the AMC and the antenna and including the radome has made the design more compact that can be easily tested without placing an insulation between the arm and the antenna. Before placing the integrated antenna on arm, it has an enhanced free space gain just like the antenna did with the rectangular patch. Therefore the results discussed in this section is free space gain and on arm analysis.

3.2. Rectangular Ring (AMC2)

Free Space:

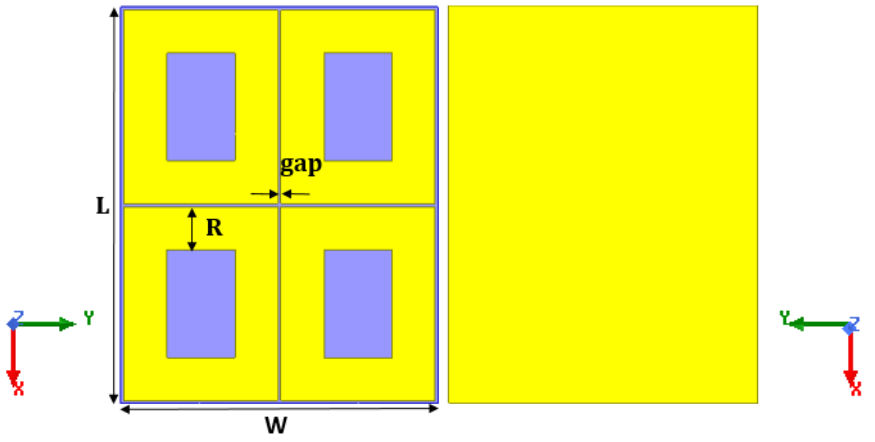

L	60mm
W	48mm
R	13.5mm
gap	0.5mm

Figure 3-32: Dimension of the Rectangular ring 2x2 AMC

An array of unit cell shows a reflection phase as that of a unit cell. The antenna (dimensions same as shown in Figure 3-1) on the rectangular ring 2x2 array is analyzed in the same way as that the rectangular patch. The important results that needs to be discussed are the gain of free space integrated antenna and on arm analysis. The difference between the Rectangular ring AMC and

the Rectangular patch AMC is the size. The dimensions in the E field direction is smaller and wider in the y direction which makes it small and ease to wrap around the arm.

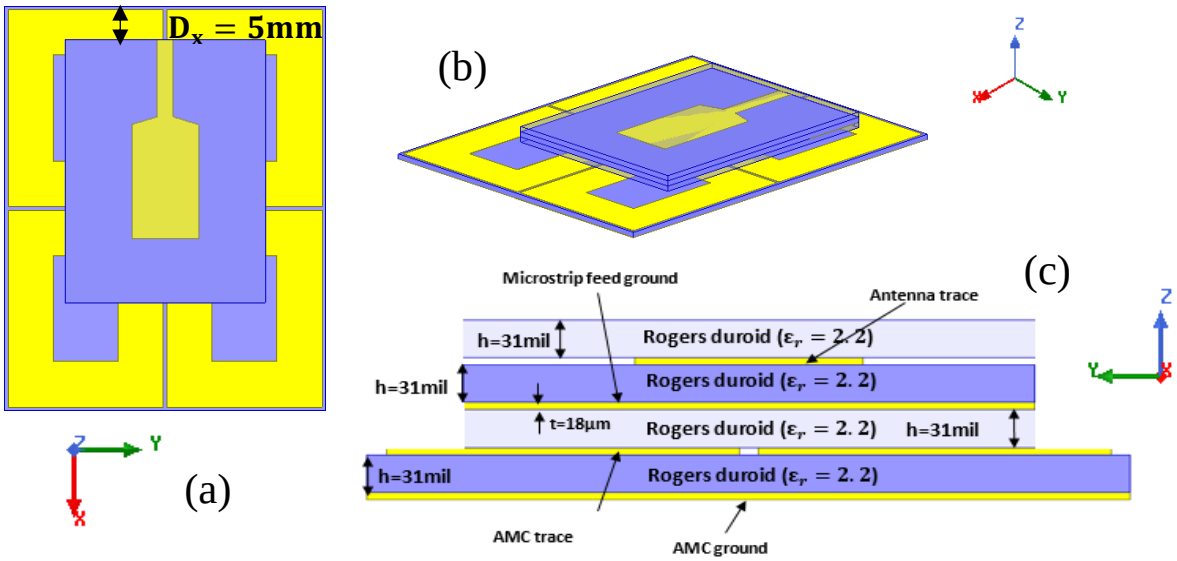

Figure 3-33: (a) Top view with D_x= 5mm (b) 3D view (c) Stack-up (Front view)

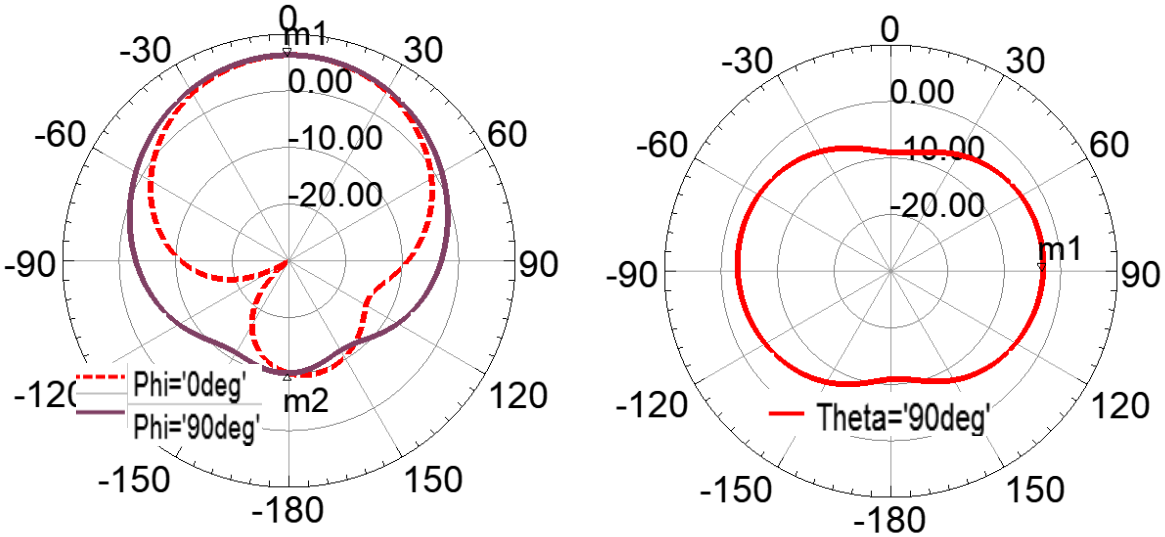

Name	Ang	Mag
m1	0.00	6.31
m2	180.00	-10.15

(a)

Name	Ang	Mag
m1	90.00	-3.09

(b)

Figure 3-34: Radiation patterns for Rectangular ring AMC (a) Elevation Plane (b) Azimuth Plane

On arm and Bend Analysis:

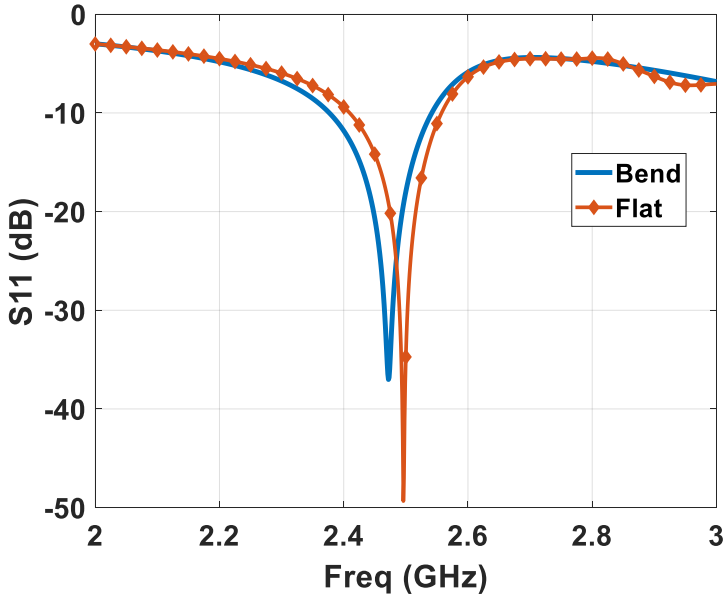

Figure 3-35: Comparison of return loss of flat and bend version of AMC Ring with antenna

When the integrated antenna was placed on arm model, the results were observed on both flat and curved arm model. Hence the bend analysis is view simultaneously by flexing the antenna on curved model. Bending the integrated antenna did affect the resonant frequency and the return loss, but not a drastic change. The change due to the bend has to be considered because it may affect real time measurements.

3.3. I-shaped (AMC3)

Free Space:

Similar to the analysis done for Rectangular ring AMC, I-shaped AMC was tested too for radiation patterns in free space. I shaped is the smallest of all the AMC designed in this thesis. The Jerusalem Cross AMC was not fabricated for its property of its size and dual band resonance, when the antenna was placed over the AMC. I-Shaped reduces the Jerusalem cross by almost half of its size.

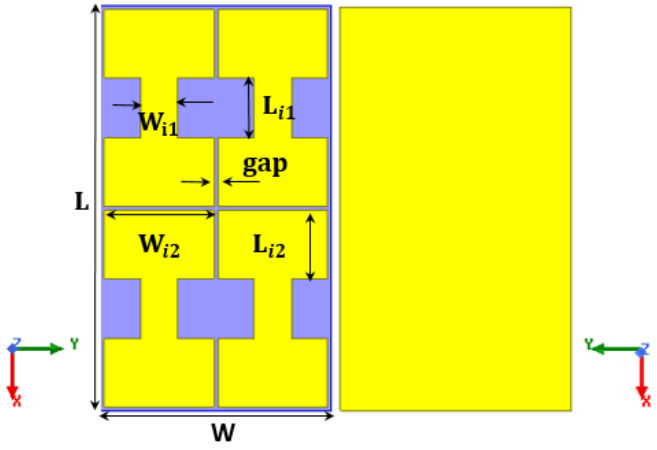

L_{i1}	7mm
W_{i1}	5mm
L_{i2}	9mm
W_{i2}	14.5mm
L	51mm
W	30mm
gap	0.5mm

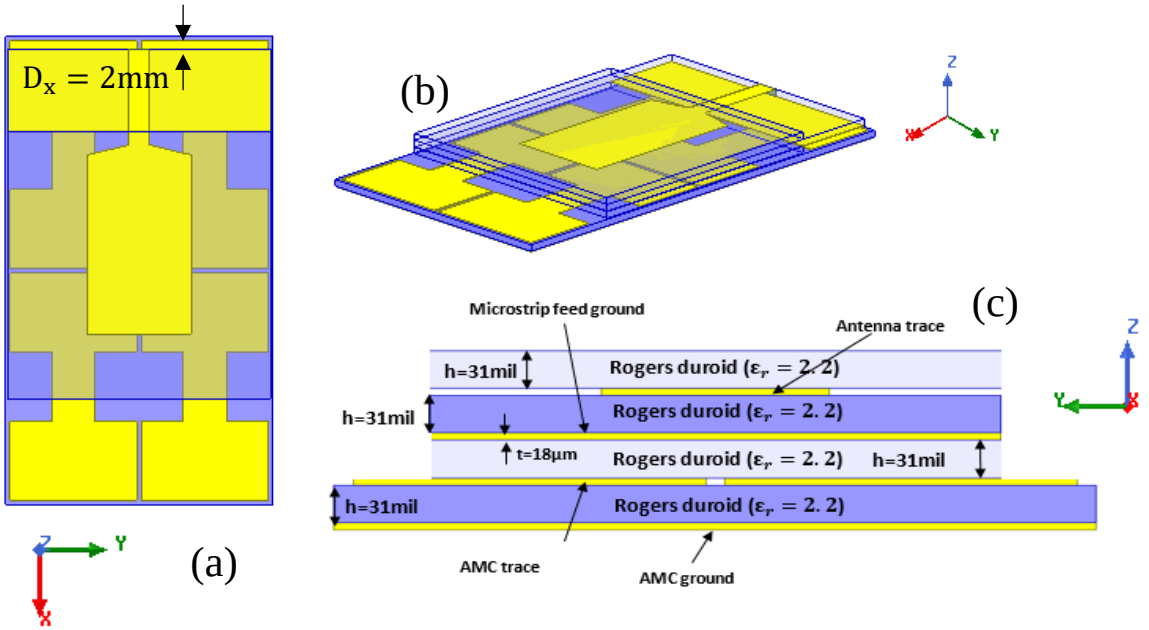

Figure 3-36: Dimension of the I-Shaped 2x2 AMC and (a) Top view with D_x= 2mm (b) 3D view (c) Stack-up (Front view)

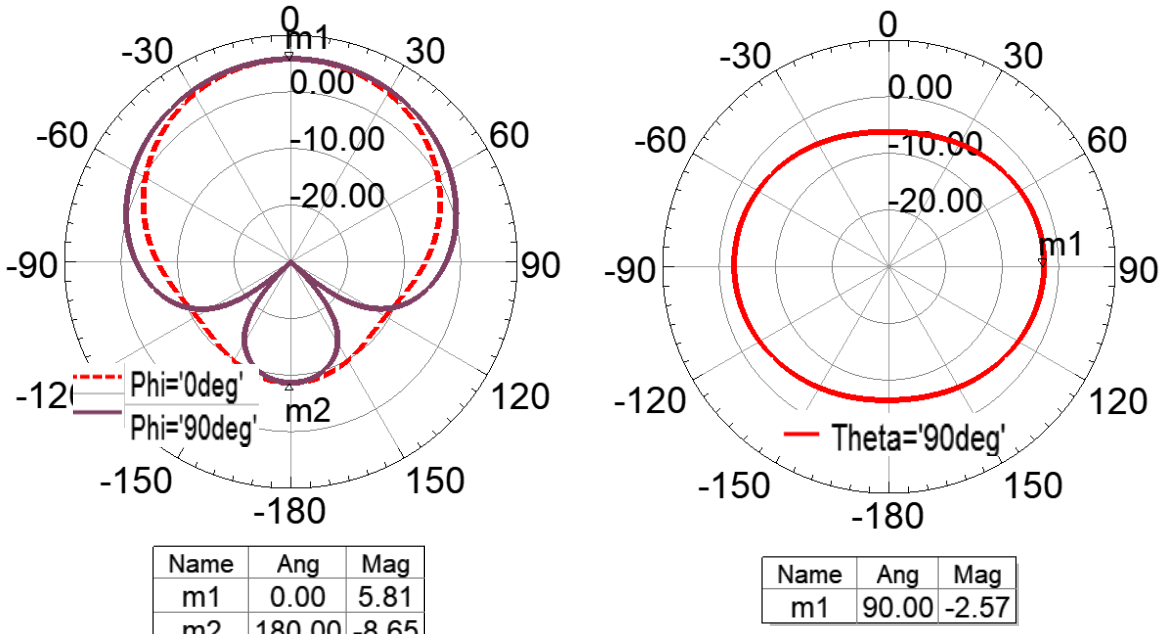

Name	Ang	Mag
m1	0.00	5.81
m2	180.00	-8.65

(a)

Name	Ang	Mag
m1	90.00	-2.57

(b)

Figure 3-37: Radiation patterns for Antenna with I-shaped AMC (a) Elevation Plane (b) Azimuth Plane

On arm and Bend Analysis:

When the integrated antenna was placed on arm model, the results were observed on both flat and curved arm model. Hence the bend analysis is viewed by simultaneously flexing the antenna on curved model. Bending the integrated antenna did affect the resonant frequency and the return loss, but not a drastic change is seen. The change due to the bend has to be considered because it may affect real time measurements. In Figure 3-38, the bend analysis is shown for version1 (L_{i1} =7mm) and version 2 (L_{i1} =8mm).

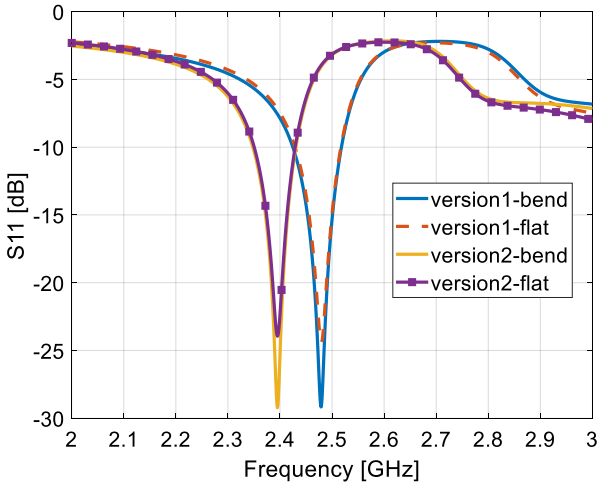

Figure 3-38: Bending analysis for I-shaped AMC

3.4. Input power and SAR

Since the antenna's power is completely focused on the body, SAR is one of the factor we definitely cannot ignore. Let's discuss the factors affecting the SAR. From Eq. (1.6) we interpret that the SAR is directly proportional to the power that is the magnitude of electric field squared. The ratio of Conductivity and mass density of the material σ/ρ ; remains constant for the material used. More the conductance, more will the power be absorbed by the material. For example, the peak SAR for different power input is given in Table 3-2 for the integrated antenna with rectangular patch AMC. As the input power to the antenna is reduced, the peak SAR reduces for every tissue. The default input power in HFSS is 1W or 30dBm. From Table 3-2 it is observed that input of 10mW or 10dBm will be safe to operate on arm as shown in Table 1-3. Therefore SAR can be controlled by the input power given to the antenna

Layer / Input power	Skin	Fat	Muscle	Bone
1W	73.90	59.90	23.2	2.56
0.1W	7.390	5.990	2.32	0.256
0.01W	0.739	0.599	0.232	0.0256
0.001W	0.0739	0.0599	0.0232	0.00256

Table 3-2: Peak SAR values over 1g of tissue at different input power levels in W/kg

4. Fabrication, Experimental validation and Comparison with Simulated Results

The simulated antennas and the AMC were fabricated and tested in Dr. Venkataraman's research group in the ETA lab at RIT. First all the antennas were tested in free space, and the return loss was recorded. The next step is to fix the antenna with the radome and the substrate in place, and finally place that setup on the arm to check the return loss when different AMC layers are placed over the antenna. The antennas discussed in this thesis were fabricated in Rogers RT/duroid 5880™ with the dielectric permittivity, ϵ_r = 2.2 and $\tan(\delta)$ = 0.0009, with a thickness, h = 31 mils (or 0.7874 mm). Additionally half ounce copper is used (thickness of 18μm).

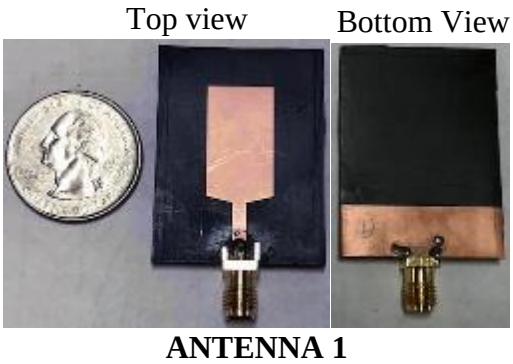

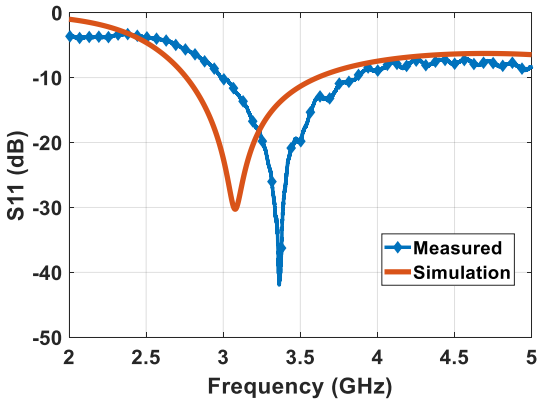

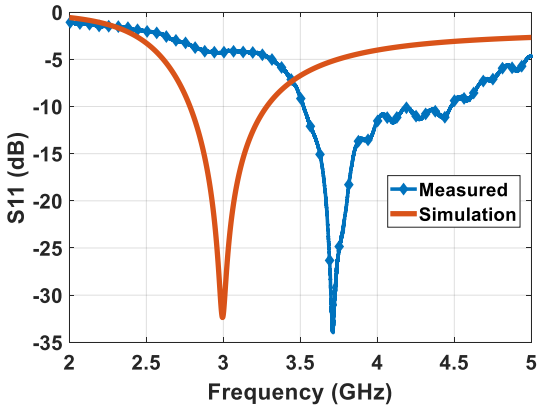

(a) (b)

Figure 4-1: (a) Antennas Fabricated (b) comparison of simulated and measured return loss

Return loss was tested using the Agilent E8363B PNA series network analyzer (10MHz-40GHz). The return loss for the antenna shown in Figure 4-1 is the antenna tested in free space. For antenna 1, the resonance has shifted to the right, resonating at a higher frequency than the simulated results. The most common reason for the frequency shift can be due to the fabrication losses, cable losses and the environment it has been tested at. The change in frequency is about 400MHz, whereas the frequency change for antenna 2 is about 700MHz which has shifted more when compared to antenna 1. For antenna 2, when AMCs were used as a ground plane, good resonance was not attained as it was getting difficult to attain the spot where maximum coupling occurs by moving the dimension D_x along the antenna as discussed earlier. For this reason all the AMC layers were test on Antenna1

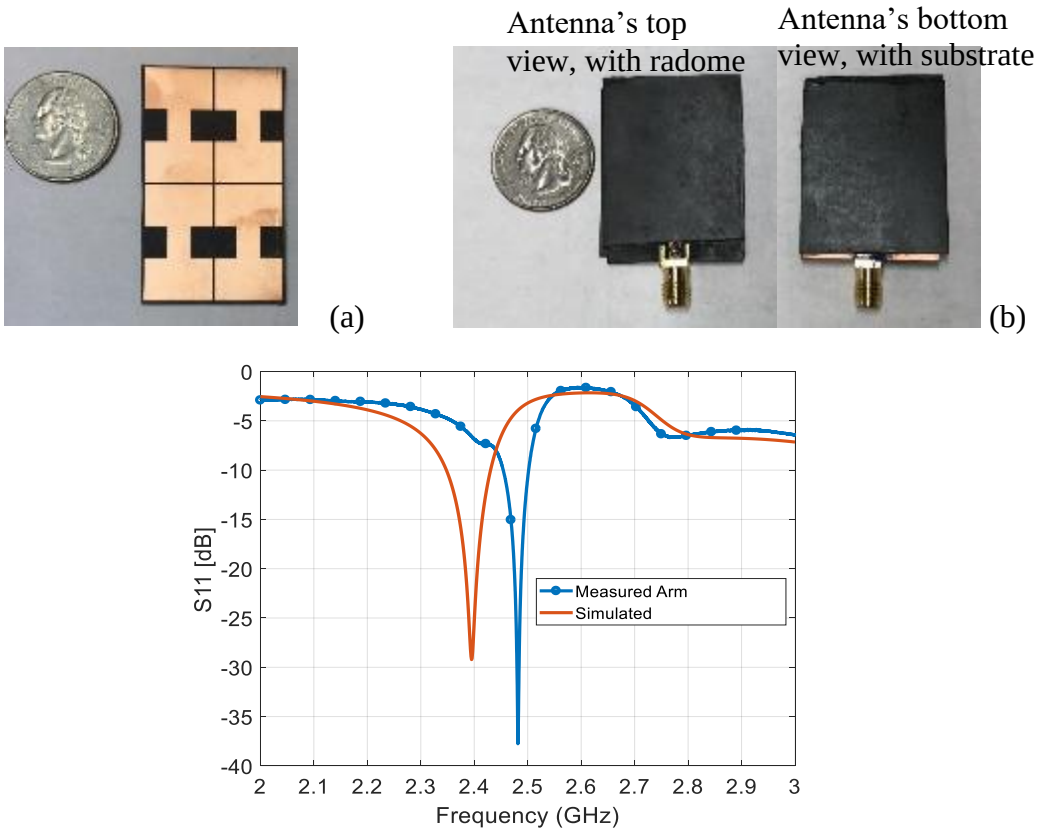

(c)

Figure 4-2: (a) I shaped AMC (b) Antenna with radome on the top and substrate below it (c) Measured and simulated return loss

Once the monopole antennas were tested, they we covered with a radome on the antenna trace side and a substrate on the antenna ground side. As you can see in Figure 4-2 (b), the antenna 1 from Figure 4-1, has been covered with the same material substrate without the copper cladding on both the sides of the antenna. The antenna was then placed on the arm with radome touching the skin. I-shaped AMC layer (Figure 4-2 (a)) was then placed over the antenna with the normal of the ground plane away from the antenna. This I-shaped AMC was fabricated with 2 dimension, one with L_{i1} = 7mm and other with L_{i1} = 8mm. The one shown in Figure 4-2 is for the dimensions L_{i1} = 8mm, because the measured return loss resonates as the frequency band of our interest (2.4-2.5GHz). The same antenna setup (radome and the substrate) used on other AMCs.

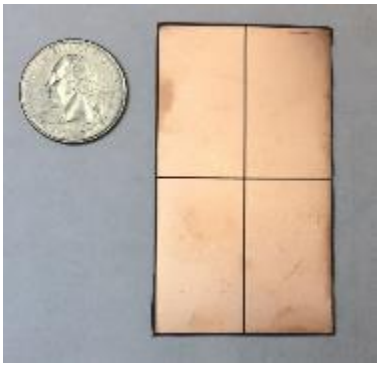

(a)

(b)

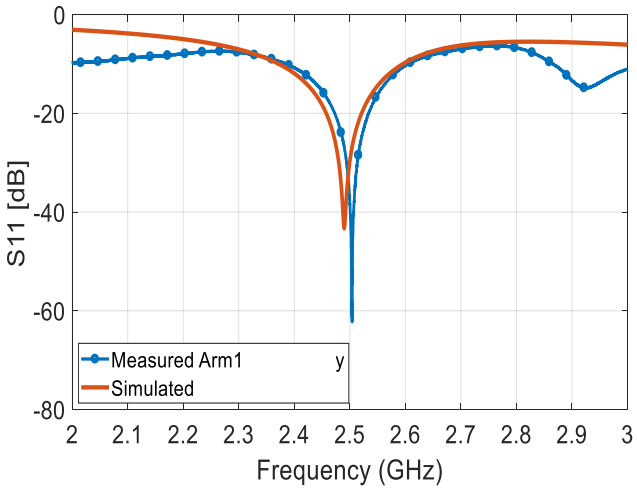

(c)

Figure 4-3: (a) Rectangular patch AMC (b) Antenna with radome on the top and substrate below it (c) Measured and simulated return loss

For rectangualar patch AMC shown in Figure 4-3, when placed over the antenna which is placed over the arm, the return loss has been better compared to the simulated results. However the 10 dB bandwidth, is beyond the frequency band (2.4-2.5GHz).

Ring AMC is the next AMC that was tested, with the same setup as that of the Rectangular patch AMC and I-shaped AMC. Maximum coupling occurs when the antenna is placed at the center of the AMC. Here is when the dimension D_x comes into play. Since the distance like to 2mm and 1mm is very difficult to attain, the AMC is moved along the x axis over the antenna to attain the resonance. The return loss for the rectangular ring shown in Figure 4-4, fits exactly in the 10db band of (2.4-2.5GHz) with the resonant frequency of 2.43GHz.

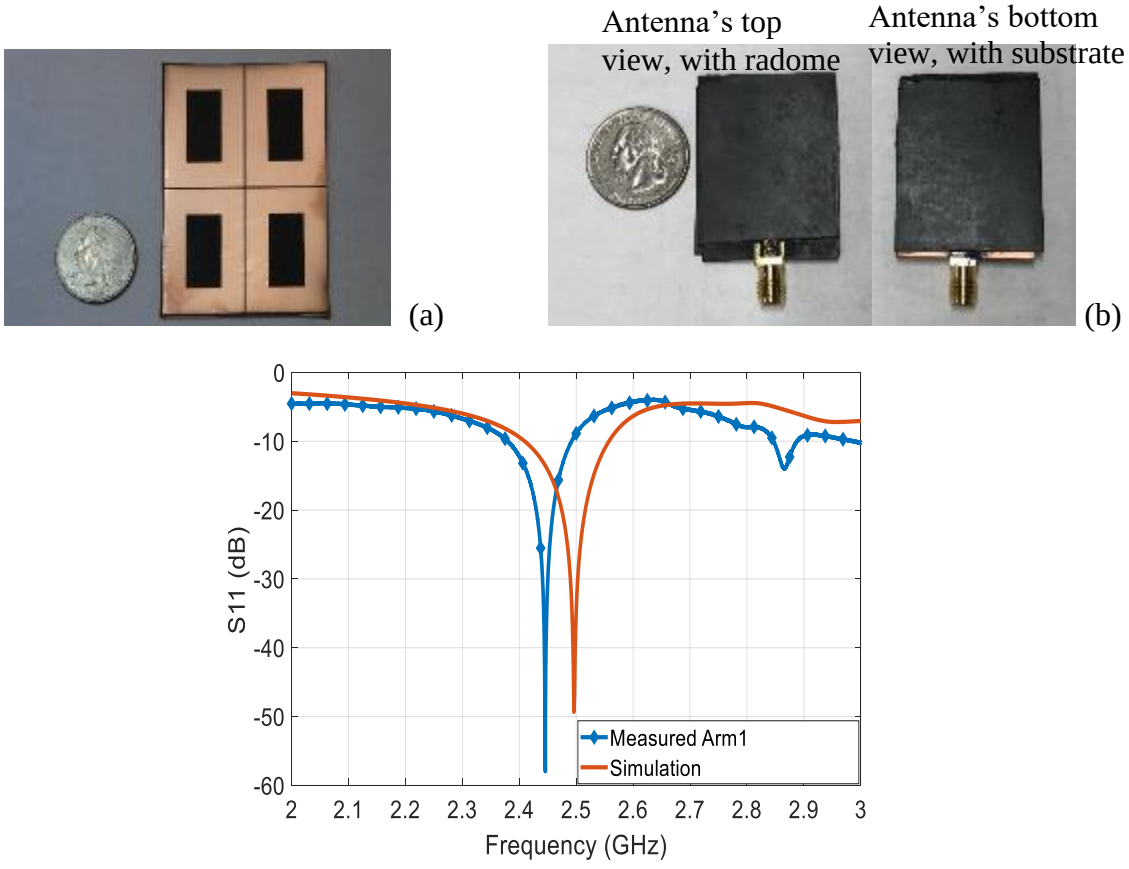

Figure 4-4: (a) Rectangular ring AMC (b) Antenna with radome on the top and substrate below it (c) Measured and simulated return loss

Now the next step is to select one particular AMC and antenna and test for whether the antennas actually responds to the changes in blood glucose in the body. I-shaped AMC is the smallest of all the AMC that we used. For this reason, it was picked to be tested for the continuous blood glucose measurement.

4.1. Glucose Monitoring Test Procedure

The primary purpose of this thesis is to overcome the challenges that were seen in the previously designed antenna. One of which was back radiation which was caused by the omnidirectional property of the antenna, which had the radiation both going into the and away from the arm (back radiation). In order to prove that this thesis has proposed antenna designed that gets rid of the back radiation, both previously designed antenna and the proposed antenna with AMC layers were subjected to arm movements and were also tested by placing the other free hand over the setup. Also, to cover all the requirements, the proposed antenna was also tested for creeping waves when the antenna was placed over the arm. Once all the antennas were tested, and compared with the simulated results, continuous glucose measurements were carried out. Since the I-shaped AMC is the smallest in size, it was chosen to be tested on a non-diabetic subject. Portable network analyzer was used in the test was Keysight Field fox Microwave Analyzer N9952A 50GHz. The input power to the antenna was -10dBm.

Step 1: Calibration of the cable to attain 0^0 phase at the end of the cable.

Step 2: Place the antenna on arm. To keep the antenna in place cable was taped on the arm.

Step 3: Place the AMC over the antenna and position to see the return loss at the required frequency and fix the AMC in place, again by taping it on the arm (see Figure 4-5, a) The setup is now ready to be tested.

Step 4: The resonant frequency was recorded using the Network Analyzer Program which tracks the results after any number of seconds we wish to see the output.

Step 5: Export the data and smoothen the curve using MATLAB to see a clear trend in the resonant shift with respect to time.

Step 6: Compare the proposed antenna with I-shaped AMC layer and the previously designed antenna with arm movement

Step 7: Measure the proposed antenna with I-shaped AMC layer with no arm movement

Step 8: Compare the effect of back radiation for both proposed antenna with Rectangular patch AMC layer and the previously designed antenna.

4.2. Tracking the shift in Antenna's resonant frequency with respect to time

In this setup, the AUT on arm was seen for a steady arm and the antenna's frequency resonance was recorded. The antenna with I-shaped AMC was used on arm to see the shift in antenna's resonant frequency with respect to time. The initial return loss was recorded as shown in (Figure4-5, b) which is resonating at 2.468GHz with a return loss of -62dB. The cable was calibrated for the frequency band 1450MHz-3450MHz for 10001 number of points. This makes a resolution of 0.2MHz and the sweep time take by the network analyzer was 6.14secs. Therefore the frequency shift was tracked every 6.2 secs. The measurements were taken just after dinner for 115 minutes on Subject 1. As it is well known that food is broken down to soluble sugars in the process of digestion, the only change in the body is the blood glucose level. The increasing trend in resonant frequency change can be related to real time changing blood glucose. The insulin is our body fights the rise the sugar level, in other words for a healthy non-diabetic subject the glucose must drop

after sometime (approx. 45mins). This measurements lasted for about 115 minutes to see if at all the antenna also tracks the drop in blood glucose. For this drop to happen it took around 80 minutes (Figure4-5, d). Also the resonance frequency drops after its maximum at 2483MHz. This experiment shows that the antenna responds to the change in glucose level in the body. A good model is required that relates the antenna's resonant frequency to the actual glucose level.

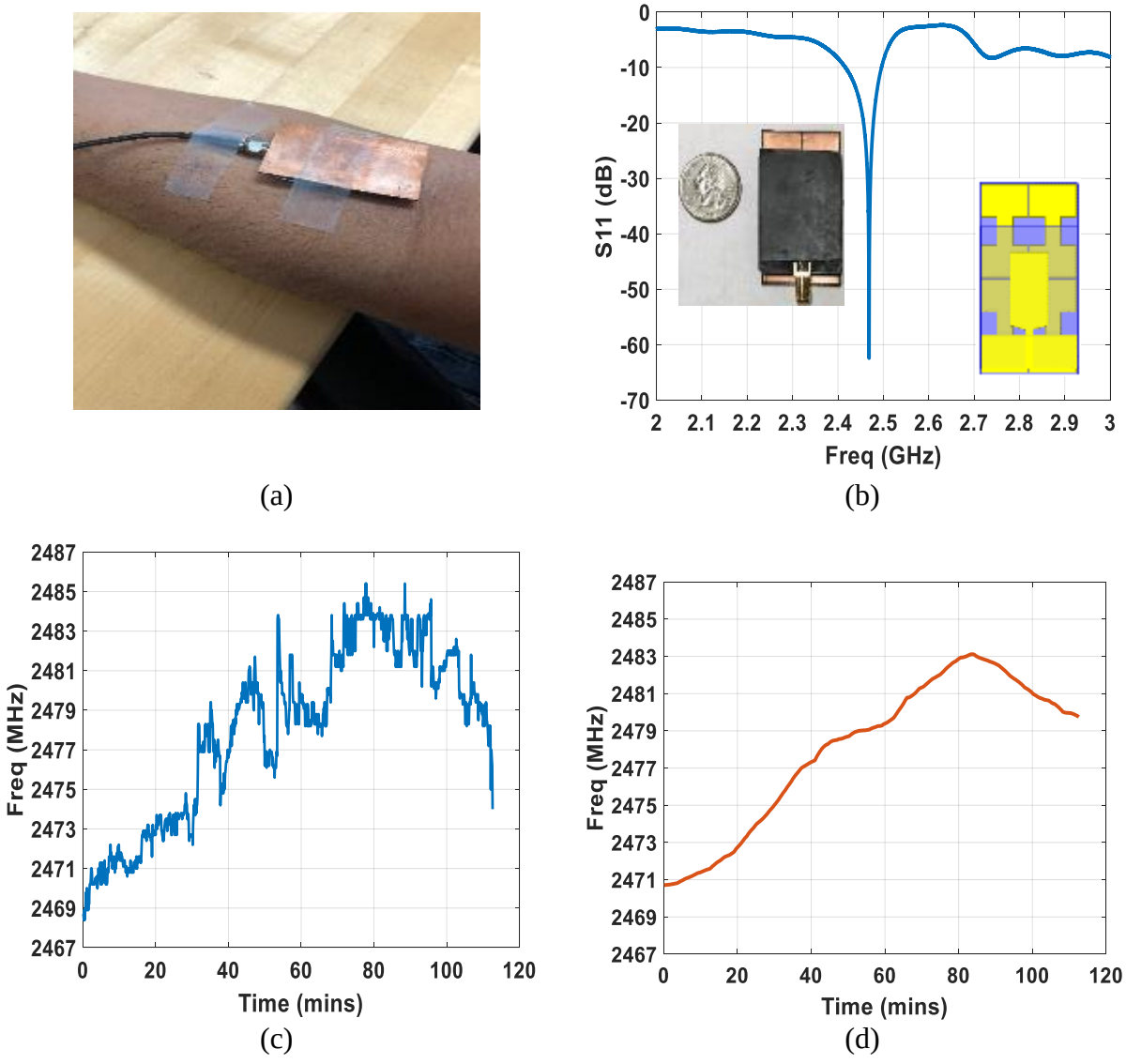

(a) (b) (c) (d)

Figure 4-5: Tracking Antenna's resonant frequency with steady arm on Subject 1 using proposed antenna with I shaped AMC layer (a) On arm setup (b) Initial return loss of antenna on arm (c) Shift of Antenna's resonant frequecy with respect to time (d) Smooth curve for (c).

4.3. Comparing the effect of Arm movement for previous and proposed antenna

In this setup, the AUT (antenna under test) on arm was subjected to movement and the antenna's frequency resonance was recorded. The shift in resonant frequency for previously designed antenna was compared to the antenna with I-shaped AMC. The initial return loss was recorded for proposed antenna, (see Figure 4-6, b) resonating at 2.468GHz with a return loss of -62dB. Whereas the initial return loss recorded for previously designed antenna, (see Figure 4-7) resonates at 1.2GHz with a return loss of -51dB. The cable was calibrated for the frequency band 1GHz-3GHz for 10001 number of points. This makes a resolution of 0.2MHz and the sweep time take by the network analyzer was 6.14secs. Therefore the frequency shift was tracked every 6.2 secs. The measurements were taken just after dinner for 70 minutes on Subject 2. Figure 4-6 (c) shows that the resonant frequency of the proposed antenna shifts to higher frequency in small time intervals resulting in a rising trend. Whereas for the previously designed antenna, the arm movement cause the antenna's resonant frequency to shift drastically causing sharp peaks in the graph (see Figure 4-7 (c)). Even if we ignore or remove the sharp change, the graph doesn't show a rising trend ((see Figure 4-7 (d)). Therefore when the previous antenna is subjected to movement is doesn't track the shift in resonant frequency quite well, which will later cause distortion in tracking the exact glucose level in our body. It can also be concluded that the proposed antenna responds very well to the movement in the arm overcoming the challenge seen in the previously designed antenna.

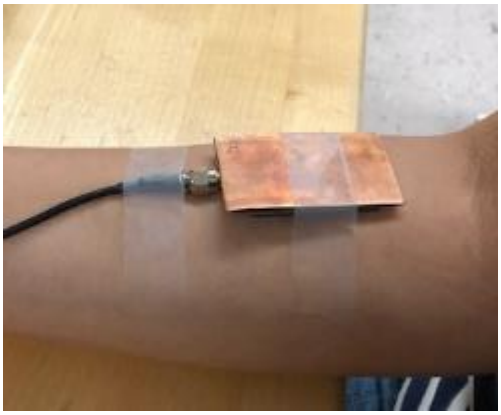

(a)

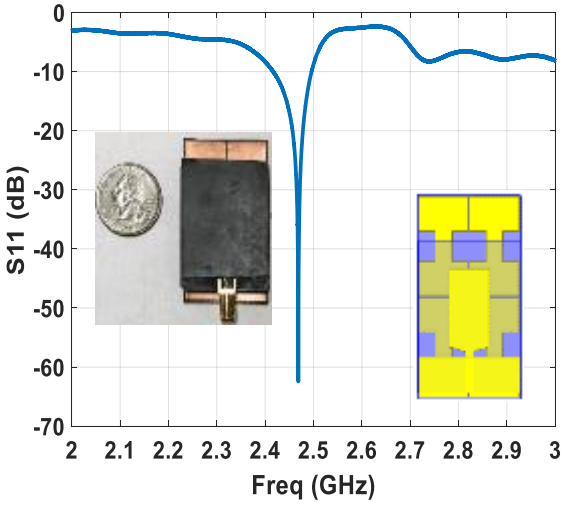

(b)

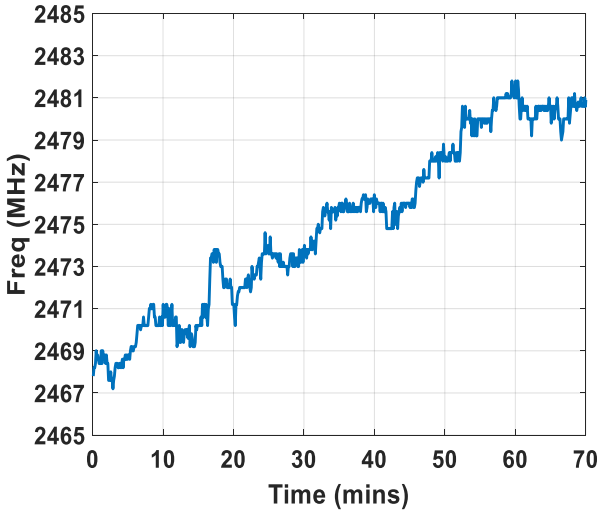

(c)

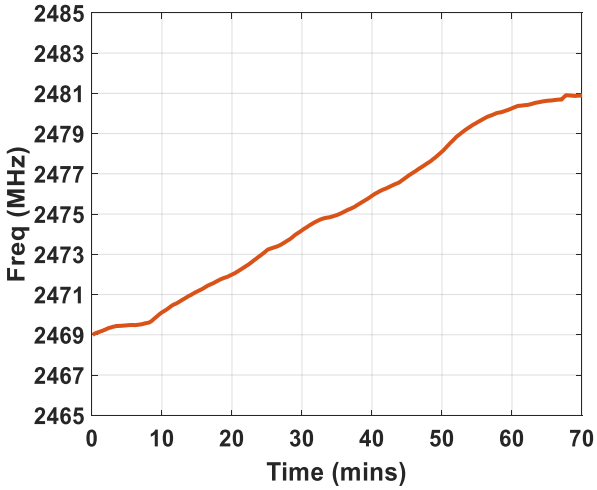

(d)

Figure 4-6: Tracking Antenna's resonant frequency with moving arm on Subject 2 using proposed antenna with I shaped AMC layer (a) On arm setup (b) Initial return loss of antenna on arm (c) Shift of Antenna's resonant frequecy with respect to time (d) Smooth curve for (c).

(a)

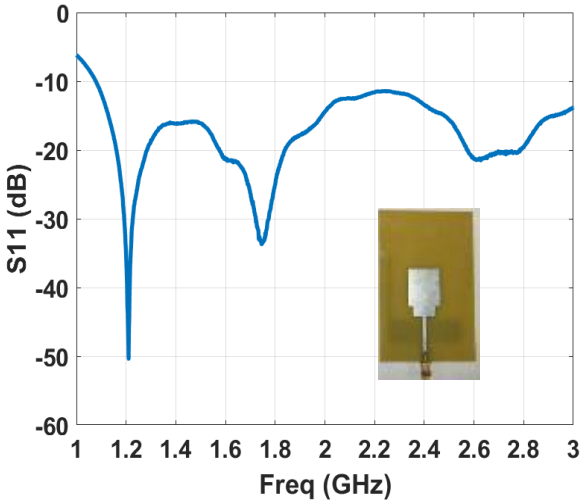

(b)

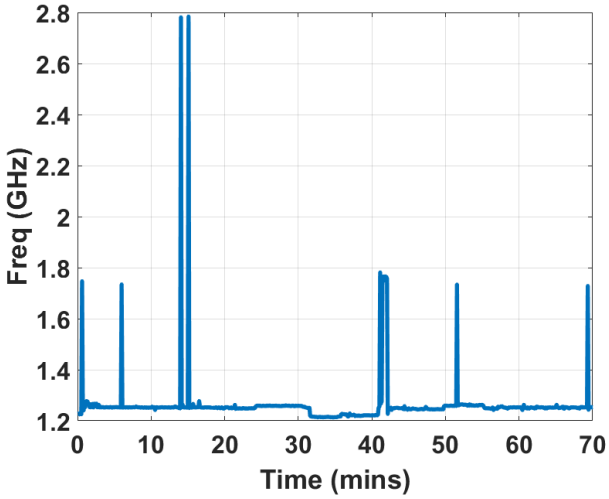

(c)

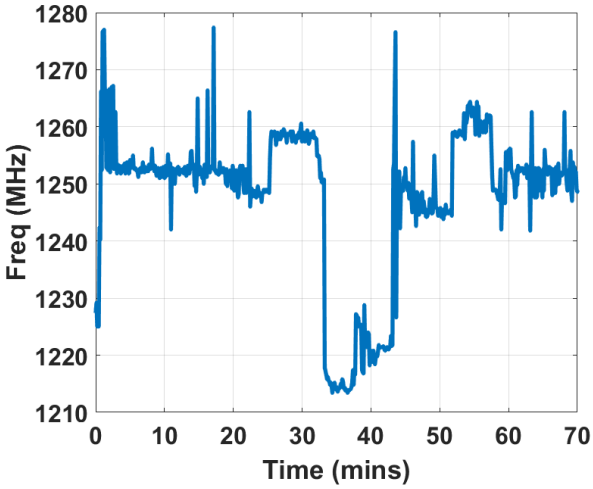

(d)

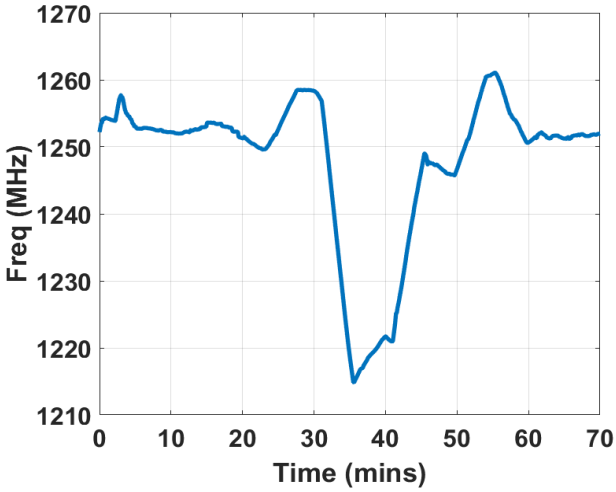

(e)

Figure 4-7: Tracking Antenna's resonant frequency with moving arm on Subject 2 using previously designed antenna. (a) On arm setup (b) Initial return loss of antenna on arm (c) Shift of Antenna's resonant frequecy with respect to time (d) Removing the sudden peaks in -(c) (e) Smooth curve for (d).

4.4. Comparing the effect of Back radiation for previous and proposed antenna

In this setup, the AUT (antenna under test) on arm was tested for back radiation and the antenna's frequency resonance was recorded. The effect of back radiation was tested using the other free arm on the AUT to check if placing the arm effect the antenna's resonant frequency. The effect of back radiation was tested for previously designed antenna which was compared to the antenna with Rectangular patch AMC. As shown in Figure 4-8, placing the hand over the proposed antenna with Rectangular AMC does not affect the return loss, this proves that there is no back radiation for the proposed antenna. Whereas the back radiation exist for the previously designed antenna, as the return loss has shifted (Figure 4-8 (d)). This will lead to error in tracking the antenna's resonant frequency with respect to time when measuring for blood glucose.

Factors observed during the test:

1) **Back radiation:** Moving/waving the free arm very close to the antenna did not change the return loss for proposed antenna with rectangular patch AMC. Whereas for the previously designed antenna, the resonant frequency shifts causing inefficient results when testing for real time shift in antenna's resonant frequency. Hence we can conclude that the proposed antenna was successful in getting rid of back radiation which existed in the previously designed antenna.
2) **Creeping waves:** When the antenna is made to radiate into the arm, some amount of radiation travels along the arm causing creeping wave. Creeping wave does occur in the proposed antenna setup. The free hand was made to rest just besides the antenna to see if that affects the results. Placing the hand next to the antenna did effect the return loss by a very small amount.

(a)

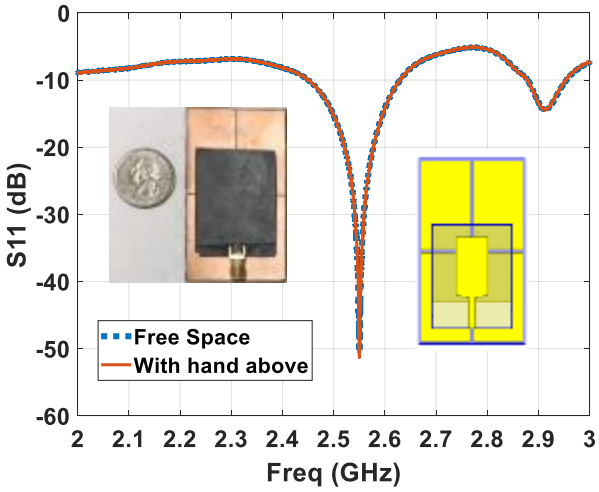

(b)

(c)

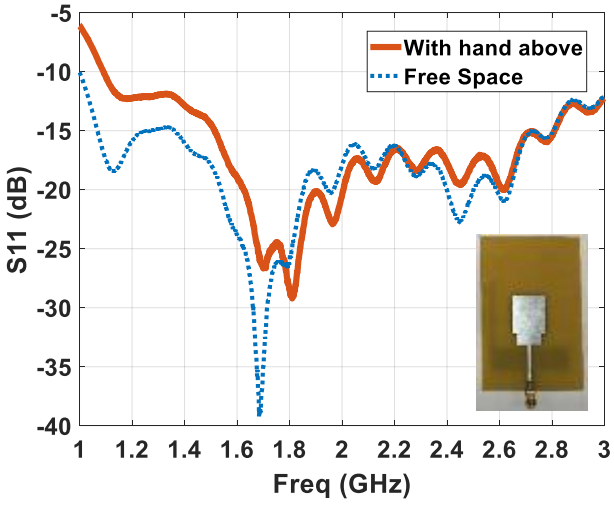

(d)

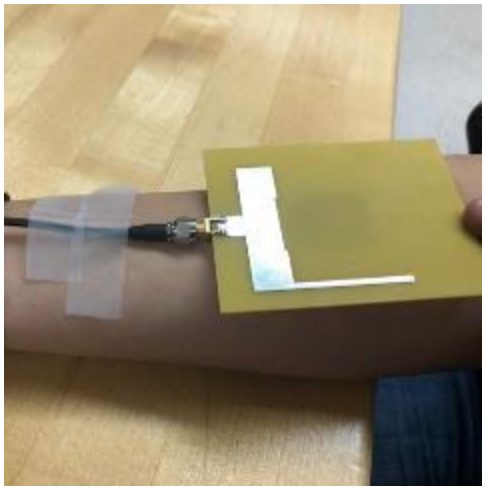

(e)

Figure 4-8: Effect of Back radiation on Antenna's resonant frequency (a) Placing the free hand on AUT (b) & (d) Return loss for both the antennas in (c) & (e) for both free space and with hand above the AUT

5. Conclusion

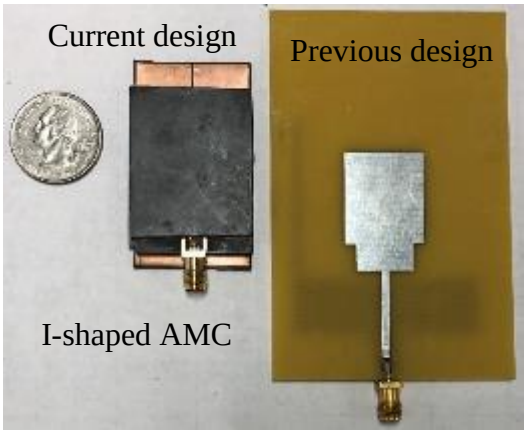

Figure 5-1: Comparison of the antenna used in this thesis to previously fabricated antenna

Antennas with AMC as a ground plane has proven to be one of the most favorable and feasible technique in getting rid of back radiation. Overall I-shaped AMC over the antenna is the smallest of the all the AMCs discussed in this thesis. The integrated antenna has drastically dropped in size when compared to the previously designed antenna (see Figure 5-1) Continuous glucose measurement proves that the integrated antenna is sensitive to the changing properties of the blood. The return loss of the antenna was tested for creeping waves, back radiation, continuous arm movements when the antenna with the AMC layer was placed on arm. This thesis also discusses the results when the antenna is made to bend. Since the substrate used for the antenna is flexible, when placed on arm it will take the subjected to deformation. The results also show that bending doesn't change the return loss. Talking about the peak SAR, the output power to the antenna was -15dBm which is well within the threshold limit listed in Table3-2, where we stated that maximum power that can be given to the antenna is 10mW or 10dBm. We can also conclude that the antenna responds to the changes in the blood glucose changes with a low input power.

5.1. Future Work

1) Final bonding of the antenna and the AMC and collecting multiple data by testing on multiple diabetic and non-diabetic patients for the antennas designed in this thesis. Once the antenna and the AMC is well bonded, the tests can be carried out for rigorous arm movements to check whether it affects the return loss
2) The creeping waves exists and can used as an advantage by designing multiple antennas around the arm. If getting rid of the creeping wave is the only key, the antenna can be wrapped around a tight lossy material to keep the antenna in place and also prevent the creeping wave to travel along the arm.
3) Develop a better understanding of what causes the permittivity of blood to change with a changing blood glucose concentration and develop a feedback loop. Naturally, in non-diabetic patients, the human body has a feedback system that balances glucose levels with insulin. Adding a feedback loop and better understanding the changes in glucose levels could build a better circuit model.
4) The equations for equivalent circuits if the unit cells above were performed in the analysis mode. It will be good if a model is derived for the synthesis mode. For a known or required resonant frequency, the ground inductance (L_d) will remain constant for a given height of dielectric material that will be used. Assuming an impedance Z_0 value for the grid inductance (L_g), the width and length for the grid inductance can be calculated. Using the effective inductance the effective grid capacitance (C_g), can be found. This will be a good design approach for unit cell when you want to design it for a given frequency and not the other way round that is used in this thesis.

References

[1] Khalid Imam, *Management and Treatment of Diabetes Mellitus*. 2013.

[2] "An Overview of Diabetes." [Online]. Available: https://www.webmd.com/diabetes/guide/diabetes-basics#1.

[3] C. for Disease Control, "National Diabetes Statistics Report, 2017 Estimates of Diabetes and Its Burden in the United States Background," 2017.

[4] D. D. Cunningham and J. A. Stenken, Eds., *In Vivo Glucose Sensing*. Hoboken, NJ, USA: John Wiley & Sons, Inc., 2009.

[5] "Diabetes Overview | Joslin Diabetes Center." [Online]. Available: http://www.joslin.org/info/an_overview_of_diabetes.html.

[6] K. Takei *et al.*, "Nanowire active-matrix circuitry for low-voltage macroscale artificial skin," *Nat. Mater.*, vol. 9, no. 10, pp. 821–826, 2010.

[7] W. Gao *et al.*, "Fully integrated wearable sensor arrays for multiplexed in situ perspiration analysis," *Nature*, vol. 529, no. 7587, pp. 509–514, 2016.

[8] M. Kaltenbrunner *et al.*, "An ultra-lightweight design for imperceptible plastic electronics," *Nature*, vol. 499, no. 7459, pp. 458–463, 2013.

[9] S. Xu *et al.*, "Soft microfluidic assemblies of sensors, circuits, and radios for the skin.," *Science*, vol. 344, no. 6179, pp. 70–4, Apr. 2014.

[10] M. C. Mcalpine, H. Ahmad, D. Wang, and J. R. Heath, "Highly ordered nanowire arrays on plastic substrates for ultrasensitive flexible chemical sensors," *Nat. Mater.*, vol. 6, no. 5, pp. 379–384, 2007.

[11] D.-H. Kim *et al.*, "Epidermal Electronics," *Science (80-.).*, vol. 333, no. 6044, pp. 838–843, Aug. 2011.

[12] D. J. Lipomi *et al.*, "Skin-like pressure and strain sensors based on transparent elastic films of carbon nanotubes," *Nat. Nanotechnol.*, vol. 6, no. 12, pp. 788–792, Dec. 2011.

[13] H. Lee *et al.*, "Wearable/disposable sweat-based glucose monitoring device with multistage transdermal drug delivery module," *Sci. Adv.*, vol. 3, no. 3, p. e1601314, Mar. 2017.

[14] A. J. Bandodkar and J. Wang, "Non-invasive wearable electrochemical sensors: a review," *Trends Biotechnol.*, vol. 32, no. 7, pp. 363–371, Jul. 2014.

[15] W. A. Fisher, T. Kohut, H. Schachner, and P. Stenger, "Understanding Self-Monitoring of

Blood Glucose Among Individuals With Type 1 and Type 2 Diabetes," *Diabetes Educ.*, vol. 37, no. 1, pp. 85–94, 2011.

[16] M. Sidley, "Calibration for Real-Time Non-Invasive Blood Glucose Monitoring." Order No. 1540160, Rochester Institute of Technology, Ann Arbor, 2013.

[17] A. Adhyapak, M. Sidley, and J. Venkataraman, "Analytical model for real time, noninvasive estimation of blood glucose level," in *2014 36th Annual International Conference of the IEEE Engineering in Medicine and Biology Society*, 2014, pp. 5020–5023.

[18] J. Venkataraman and B. Freer, "Feasibility of non-invasive blood glucose monitoring: In-vitro measurements and phantom models," in *2011 IEEE International Symposium on Antennas and Propagation (APSURSI)*, 2011, pp. 603–606.

[19] "Checking Your Blood Glucose (Blood Sugar): American Diabetes Association®." [Online]. Available: http://www.diabetes.org/living-with-diabetes/treatment-and-care/blood-glucose-control/checking-your-blood-glucose.html.

[20] S. F. Clarke and J. R. Foster, "A history of blood glucose meters and their role in self-monitoring of diabetes mellitus," *Br. J. Biomed. Sci.*, vol. 69, no. 2, pp. 83–93, 2012.

[21] J. Kirsch, C. Siltanen, Q. Zhou, A. Revzin, and A. Simonian, "Biosensor technology: recent advances in threat agent detection and medicine," *Chem. Soc. Rev.*, vol. 42, no. 22, p. 8733, 2013.

[22] V. R. Kondepati and H. M. Heise, "Recent progress in analytical instrumentation for glycemic control in diabetic and critically ill patients," *Anal. Bioanal. Chem.*, vol. 388, no. 3, pp. 545–563, 2007.

[23] V. Scognamiglio, "Nanotechnology in glucose monitoring: Advances and challenges in the last 10 years," *Biosens. Bioelectron.*, vol. 47, pp. 12–25, 2013.

[24] T. M. H. Lee, "Over-the-counter biosensors: Past, present, and future," *Sensors*, vol. 8, no. 9, pp. 5535–5559, 2008.

[25] "Treatment & Care for Diabetes." [Online]. Available: http://www.diabetes.org/living-with-diabetes/treatment-and-care/.

[26] D. Desalvo and B. Buckingham, "Continuous glucose monitoring: Current use and future directions," *Curr. Diab. Rep.*, vol. 13, no. 5, pp. 657–662, 2013.

[27] B. Grosman *et al.*, "Combining Technology with Treatment," no. April, pp. 53–62, 2010.

[28] W. T. Cefalu and W. V Tamborlane, "The artificial pancreas: are we there yet?," *Diabetes*

Care, vol. 37, no. 5, pp. 1182–3, Jan. 2014.

[29] G. I. Sidorenko, E. I. Zborovskiĭ, and D. I. Levina, "[Surface-active properties of the exhaled air condensate (a new method of studying lung function)].," *Ter. Arkh.*, vol. 52, no. 3, pp. 65–8, 1980.

[30] I. Horváth, J. Hunt, P. J. Barnes, and K. Alving, "Exhaled breath condensate: methodological recommendations and unresolved questions," *Eur. Respir. J.*, vol. 26, no. 3, pp. 523–548, Sep. 2005.

[31] K. Roberts, A. Jaffe, C. Verge, and P. S. Thomas, "Noninvasive Monitoring of Glucose Levels: Is Exhaled Breath the Answer?," *J. Diabetes Sci. Technol.*, vol. 6, no. 3, pp. 659–664, May 2012.

[32] P. Montuschi, "Analysis of exhaled breath condensate in respiratory medicine: methodological aspects and potential clinical applications.," *Ther. Adv. Respir. Dis.*, vol. 1, no. 1, pp. 5–23, Oct. 2007.

[33] M. J. HENDERSON, B. A. KARGER, and G. A. WREN SHALL, "Acetone in the breath; a study of acetone exhalation in diabetic and nondiabetic human subjects.," *Diabetes*, vol. 1, no. 3, p. 188–93; passim, May 1952.

[34] C. N. Tassopoulos, D. Barnett, and T. Russell Fraser, "BREATH-ACETONE AND BLOOD-SUGAR MEASUREMENTS IN DIABETES," *Lancet*, vol. 293, no. 7609, pp. 1282–1286, Jun. 1969.

[35] E. H. Baker *et al.*, "Hyperglycemia and cystic fibrosis alter respiratory fluid glucose concentrations estimated by breath condensate analysis," *J Appl Physiol*, vol. 102, pp. 1969–1975, 2007.

[36] "New England Breath Technologies, Inc. - Diabetes Screener & Monitor | ILLUME SCREENER." [Online]. Available: https://www.newenglandbreath.com/illume-screener.

[37] P. Makaram, D. Owens, and J. Aceros, "Trends in Nanomaterial-Based Non-Invasive Diabetes Sensing Technologies," *Diagnostics*, vol. 4, pp. 27–46, 2014.

[38] C. Liao, M. Zhang, M. Y. Yao, T. Hua, L. Li, and F. Yan, "Flexible Organic Electronics in Biology: Materials and Devices," *Adv. Mater.*, vol. 27, no. 46, pp. 7493–7527, Dec. 2015.

[39] O. Veiseh, B. C. Tang, K. A. Whitehead, D. G. Anderson, and R. Langer, "Managing diabetes with nanomedicine: challenges and opportunities.," *Nat. Rev. Drug Discov.*, vol. 14, no. 1, pp. 45–57, Jan. 2015.

[40] O. Olarte, J. Chilo, J. Pelegri-Sebastia, K. Barbé, and W. Van Moer, “Glucose detection in human sweat using an electronic nose.,” *Conf. Proc. ... Annu. Int. Conf. IEEE Eng. Med. Biol. Soc. IEEE Eng. Med. Biol. Soc. Annu. Conf.*, vol. 2013, pp. 1462–5, Jan. 2013.

[41] Q. Yan, B. Peng, G. Su, B. E. Cohan, T. C. Major, and M. E. Meyerhoff, “Measurement of Tear Glucose Levels with Amperometric Glucose Biosensor/Capillary Tube Configuration,” *Anal. Chem.*, vol. 83, no. 21, pp. 8341–8346, Nov. 2011.

[42] S. K. Vashist, “Non-invasive glucose monitoring technology in diabetes management: a review.,” *Anal. Chim. Acta*, vol. 750, pp. 16–27, Oct. 2012.

[43] M. J. Tierney, H. L. Kim, M. D. Burns, J. A. Tamada, and R. O. Potts, “Electroanalysis of Glucose in Transcutaneously Extracted Samples,” *Electroanalysis*, vol. 12, no. 9, pp. 666–671, May 2000.

[44] J. Moyer, D. Wilson, I. Finkelshtein, B. Wong, and R. Potts, “Correlation Between Sweat Glucose and Blood Glucose in Subjects with Diabetes,” *Diabetes Technol. Ther.*, vol. 14, no. 5, pp. 398–402, May 2012.

[45] N. S. Oliver, C. Toumazou, A. E. G. Cass, and D. G. Johnston, “Glucose sensors: a review of current and emerging technology,” *Diabet. Med.*, vol. 26, no. 3, pp. 197–210, Mar. 2009.

[46] C.-F. So, K.-S. Choi, T. K. Wong, and J. W. Chung, “Recent advances in noninvasive glucose monitoring.,” *Med. Devices (Auckl).*, vol. 5, pp. 45–52, 2012.

[47] D. C. Klonoff, “Continuous glucose monitoring: roadmap for 21st century diabetes therapy.,” *Diabetes Care*, vol. 28, no. 5, pp. 1231–9, May 2005.

[48] E. Cengiz and W. V. Tamborlane, “A Tale of Two Compartments: Interstitial Versus Blood Glucose Monitoring,” *Diabetes Technol. Ther.*, vol. 11, no. s1, p. S-11-S-16, Jun. 2009.

[49] A. J. Berger, T.-W. Koo, I. Itzkan, G. Horowitz, and M. S. Feld, “Multicomponent blood analysis by near-infrared Raman spectroscopy.”

[50] E. Hanlon, “Physics in Medicine & Biology Prospects for in vivo Raman spectroscopy,” *Phys. Med. Biol*, vol. 45, 2000.

[51] M. Sidley and J. Venkataraman, "Non-invasive estimation of blood glucose a feasibility study," *2013 IEEE Applied Electromagnetics Conference (AEMC)*, Bhubaneswar, 2013, pp.1-2. doi: 10.1109/AEMC.2013.7045069.

[52] W. Liu, F. Yeh, and M. Ghavami, “Miniaturized implantable broadband antenna for biotelemetry communication,” *Microw. Opt. Technol. Lett.*, vol. 50, no. 9, pp. 2407–2409,

Sep. 2008.

[53] A. Kiourti and K. S. Nikita, “Miniature scalp-implantable antennas for telemetry in the MICS and ISM bands: Design, safety considerations and link budget analysis,” *IEEE Trans. Antennas Propag.*, 2012.

[54] C.-M. Lee, T.-C. Yo, C.-H. Luo, C.-H. Tu, and Y.-Z. Juang, “Compact broadband stacked implantable antenna for biotelemetry with medical devices,” *Electron. Lett.*, vol. 43, no. 12, p. 660, 2007.

[55] C.-M. Lee, T.-C. Yo, F.-J. Huang, and C.-H. Luo, “Bandwidth enhancement of planar inverted-F antenna for implantable biotelemetry,” *Microw. Opt. Technol. Lett.*, vol. 51, no. 3, pp. 749–752, Mar. 2009.

[56] Y. Feldman, A. Puzenko, and Y. Ryabov, “DIELECTRIC RELAXATION PHENOMENA IN COMPLEX MATERIALS,” John Wiley & Sons, Inc., 2005, p. 125.

[57] Itu, “LIST OF ITU-R RECOMMENDATIONS AND REPORTS,” 2007.

[58] W. G. Scanlon, J. Brian Burns, and N. E. Evans, “Radiowave propagation from a tissue-implanted source at 418 MHz and 916.5 MHz,” *IEEE Trans. Biomed. Eng.*, vol. 47, no. 4, pp. 527–534, 2000.

[59] A. Sani, A. Alomainy, and Y. Hao, “Numerical characterization and link budget evaluation of wireless implants considering different digital human phantoms,” *IEEE Trans. Microw. Theory Tech.*, vol. 57, no. 10, pp. 2605–2613, 2009.

[60] J. Kim and Y. Rahmat-Samii, “Implanted antennas inside a human body: Simulations, designs, and characterizations,” *IEEE Trans. Microw. Theory Tech.*, vol. 52, no. 8 II, pp. 1934–1943, 2004.

[61] P. Soontornpipit, C. M. Furse, and Y. C. Chung, “Design of implantable microstrip antenna for communication with medical implants,” *IEEE Trans. Microw. Theory Tech.*, vol. 52, no. 8 II, pp. 1944–1951, 2004.

[62] P. Soontornpipit, “Miniaturized biocompatible microstrip antenna using genetic algorithm,” *IEEE Trans. Antennas Propag.*, vol. 64, no. 240, pp. 69\\-1945, 2005.

[63] Z. N. Chen, G. C. Liu, and T. S. P. See, “Transmission of RF signals between MICS loop antennas in free space and implanted in the human head,” *IEEE Trans. Antennas Propag.*, vol. 57, no. 6, pp. 1850–1854, 2009.

[64] T. Karacolak, R. Cooper, and E. Topsakal, “Electrical properties of rat skin and design of

implantable antennas for medical wireless telemetry," *IEEE Trans. Antennas Propag.*, vol. 57, no. 9, pp. 2806–2812, 2009.

[65] C. J. Sánchez-Fernández, O. Quevedo-Teruel, J. Requena-Carrión, L. Inclán-Sánchez, and E. Rajo-Iglesias, "Dual-band microstrip patch antenna based on short-circuited ring and spiral resonators for implantable medical devices," *IET Microwaves, Antennas Propag.*, vol. 4, no. 8, p. 1048, 2010.

[66] F. J. Huang, C. M. Lee, C. L. Chang, L. K. Chen, T. C. Yo, and C. H. Luo, "Rectenna application of miniaturized implantable antenna design for triple-band biotelemetry communication," *IEEE Trans. Antennas Propag.*, 2011.

[67] J. Gemio, J. Parrón, and J. Soler, "HUMAN BODY EFFECTS ON IMPLANTABLE ANTEN- NAS FOR ISM BANDS APPLICATIONS: MODELS COM- PARISON AND PROPAGATION LOSSES STUDY," *Prog. Electromagn. Res.*, vol. 110, pp. 437–452, 2010.

[68] N. Vidal, S. Curto, J. M. Lopez-Villegas, J. Sieiro, and F. M. Ramos, "Detuning effects on implantable antenna at various human positions," *Proc. 6th Eur. Conf. Antennas Propagation, EuCAP 2012*, pp. 1231–1234, 2012.

[69] A. Kiourti and K. S. Nikita, "A Review of Implantable Patch Antennas for Biomedical Telemetry: Challenges and Solutions," *IEEE Antennas and Propagation Magazine*, pp. 210–228, 2012.

[70] M. D. Weiss, J. L. Smith, and J. Bach, "RF coupling in a 433-MHz biotelemetry system for an artificial hip," *IEEE Antennas Wirel. Propag. Lett.*, vol. 8, pp. 916–919, 2009.

[71] M. Z. Azad and M. Ali, "A miniature implanted inverted-F antenna for GPS application," *IEEE Trans. Antennas Propag.*, vol. 57, no. 6, pp. 1854–1858, 2009.

[72] W. Xia, K. Saito, M. Takahashi, and K. Ito, "Performances of an implanted cavity slot antenna embedded in the human arm," *IEEE Trans. Antennas Propag.*, vol. 57, no. 4 PART. 1, pp. 894–899, 2009.

[73] M. L. Scarpello *et al.*, "Design of an Implantable Slot Dipole Conformal Flexible Antenna for Biomedical Applications," *IEEE Trans. Antennas Propag.*, vol. 59, no. 10, pp. 3556–3564, 2011.

[74] Y. Ahmed, Y. Hao, and C. Parini, "A 31.5GHz Patch Antenna Design for Medical Implants," *Int. J. Antennas Propag.*, p. 6, 2008.

[75] F. C. Commission, O. O. F. Engineering, and R. Division, “FCC ONLINE TABLE OF FREQUENCY ALLOCATIONS,” *Antenna*, 2017.

[76] A. F. Robert Cleveland and J. M. David Sylvar Jerry L Ulcek, “Evaluating Compliance with FCC Guidelines for Human Exposure to Radiofrequency Electromagnetic Fields,” 1997.

[77] K. Chan, “Overview of RF Exposure.”

[78] Kwok, “Title: General RF Exposure Policies for Equipment Authorization,” 2012.

[79] D. A. Sánchez-Hernández, *High frequency electromagnetic dosimetry*. Artech House, 2009.

[80] C. Gabriel, S. Gabriel, and E. Corthout, “The dielectric properties of biological tissues: I. Literature survey,” *... Med. Biol.*, 1996.

[81] S. Gabriel, R. W. Lau, and C. Gabriel, “The dielectric properties of biological tissues: II. Measurements in the frequency range 10 Hz to 20 GHz,” *Physiol. Med. Biol.*, vol. 41, pp. 2251–2269, 1996.

[82] S. Gabriel, R. W. Lau, and C. Gabriel, “Physics in Medicine & Biology The dielectric properties of biological tissues: III. Parametric models for the dielectric spectrum of tissues The dielectric properties of biological tissues: II. Measurements in the frequency range 10 Hz to 20 GHz,” *Phys. Med. Biol. Phys. Med. Biol*, vol. 41, no. 41, pp. 2251–2269, 1996.

[83] A. Kiourti, M. Christopoulou, and K. S. Nikita, “Performance of a novel miniature antenna implanted in the human head for wireless biotelemetry,” *IEEE Antennas Propag. Soc. AP-S Int. Symp.*, pp. 392–395, 2011.

[84] A. Kiourti and K. S. Nikita, “Meandered versus Spiral Novel Miniature PIFAs Implanted in the Human Head: Tuning and Performance,” Springer, Berlin, Heidelberg, 2012, pp. 80–87.

[85] W.-C. Liu, S.-H. Chen, and C.-M. Wu, “Implantable Broadband Circular Stacked Pifa Antenna for Biotelemetry Communication,” *J. Electromagn. Waves Appl.*, vol. 22, no. 13, pp. 1791–1800, Jan. 2008.

[86] D. Sievenpiper, “High-Impedance Electromagnetic Surfaces,” 1999.

[87] A. Vallecchi, J. R. De Luis, F. Capolino, and F. De Flaviis, “Low Profile Fully Planar Folded Dipole Antenna on a High Impedance Surface,” *IEEE Trans. Antennas Propag.*, vol. 60, no. 1, pp. 51–62, Jan. 2012.

[88] Z. H. Jiang, D. E. Brocker, S. Member, P. E. Sieber, S. Member, and D. H. Werner, “A Compact, Low-Profile Metasurface-Enabled Antenna for Wearable Medical Body-Area

Network Devices," *IEEE Trans. Antennas Propag.*, vol. 62, no. 8, pp. 4021–4030, 2014.

[89] H. R. Raad, A. I. Abbosh, H. M. Al-Rizzo, and D. G. Rucker, "Flexible and Compact AMC Based Antenna for Telemedicine Applications," *IEEE Trans. Antennas Propag.*, vol. 61, no. 2, pp. 524–531, 2013.

[90] M. E. de Cos, Y. Alvarez, and F. Las-Heras, "Novel Broadband Artificial Magnetic Conductor With Hexagonal Unit Cell," *IEEE Antennas Wirel. Propag. Lett.*, vol. 10, pp. 615–618, 2011.

[91] A. Arriola, J. I. Sancho, S. Brebels, M. Gonzalez, and W. De Raedt, "Stretchable dipole antenna for body area networks at 2.45 GHz," *IET Microwaves, Antennas Propag.*, vol. 5, no. 7, p. 852, 2011.

[92] S. [Kamya and Y. Yazdandoost, "Channel Model for Body Area Network (BAN)," 2009.

[93] M. Chen, S. Gonzalez, A. Vasilakos, H. Cao, and V. C. M. Leung, "Body Area Networks: A Survey," *Mob. Networks Appl.*, vol. 16, no. 2, pp. 171–193, Apr. 2011.

[94] M. R. Kamarudin, Y. I. Nechayev, and P. S. Hall, "Performance of Antennas in the On-Body Environment," in *2005 IEEE Antennas and Propagation Society International Symposium*, vol. 3A, pp. 475–478.

[95] Z. H. Hu, M. Gallo, Q. Bai, Y. I. Nechayev, P. S. Hall, and M. Bozzettit, "Measurements and simulations for on-body antenna design and propagation studies," in *2nd European Conference on Antennas and Propagation (EuCAP 2007)*, 2007, pp. 540–540.

[96] M. Hosseinipanah and Q. Wu, "Equivalent Circuit Model for Designing of Jerusalem Cross-Based Artificial Magnetic Conductors."

[97] F. Costa, A. Monorchio, and G. Manara, "Efficient analysis of frequency-selective surfaces by a simple equivalent-circuit model," *IEEE Antennas Propag. Mag.*, 2012.

[98] L. Olivia Nur, A. Kurniawan, and A. Munir, "Theoretical Analysis of Resonant Frequency for AMC-based Absorber Composed of Square Patch Array," *Int. J. Electr. Eng. Informatics -*, vol. 7, no. 2, 2015.

[99] A. Foroozesh and L. Shafai, "Investigation into the application of artificial magnetic conductors to bandwidth broadening, gain enhancement and beam shaping of low profile and conventional monopole antennas," *IEEE Trans. Antennas Propag.*, vol. 59, no. 1, pp. 4–20, 2011.

[100] D. Sievenpiper, "High-Impedance Electromagnetic Surfaces," *PhD Thesis*, p. 150, 1999.

[101] M. Hosseini and M. Hakkak, “Characteristics Estimation for Jerusalem Cross-Based Artificial Magnetic Conductors,” *IEEE Antennas Wirel. Propag. Lett.*, vol. 7, pp. 58–61, 2008.

[102] H. Mosallaei and K. Sarabandi, “Antenna Miniaturization and Bandwidth Enhancement Using a Reactive Impedance Subsrate,” *IEEE Trans. Antennas Propag.*, vol. 52, no. 9, pp. 2403–2414, 2004.

[103] G. Goussetis, A. P. Feresidis, and J. C. Vardaxoglou, “Tailoring the AMC and EBG characteristics of periodic metallic arrays printed on grounded dielectric substrate,” *IEEE Trans. Antennas Propag.*, vol. 54, no. 1, pp. 82–89, 2006.

[104] A. Seyfollahi and J. Bornemann, “Printed-Circuit Monopole Antenna for Super- Wideband Applications.”

[105] K. P. Ray, “Design Aspects of Printed Monopole Antennas for Ultra-Wide Band Applications,” *Int. J. Antennas Propag.*, vol. 2008, pp. 1–8, 2008.

[106] M. John and M. J. Ammann, “Optimization of impedance bandwidth for the printed rectangular monopole antenna,” *Microw. Opt. Technol. Lett.*, vol. 47, no. 2, pp. 153–154, 2005.

[107] A. Agrawal, D. Vakula, and N. V. S. N. Sarma, “Design of Elliptical Microstrip Patch Antenna Using ANN.”

[108] M. J. Ammann and Z. N. Chen, “A wide-band shorted planar monopole with bevel,” *IEEE Trans. Antennas Propag.*, vol. 51, no. 4, pp. 901–903, 2003.

Appendix A

Unit cell HFSS simulation

An overview of simulating a unit cell is given below. Before boundaries are assigned, a unit cell with required dimensions is drawn. The unit cell used is I shaped, discussed in the thesis, with the trace at the top of the substrate with complete ground plane at the bottom. The metal traces have a thickness of 18μm and a substrate height of 31mils. Copper was assigned to the metal traces and the Substrate used was Rogers Duroid 5880™ which has a permittivity of 2.2 and tanδ of 0.009. Once we have the layout set, the total height of the cell is now (31mils+18μm*2).

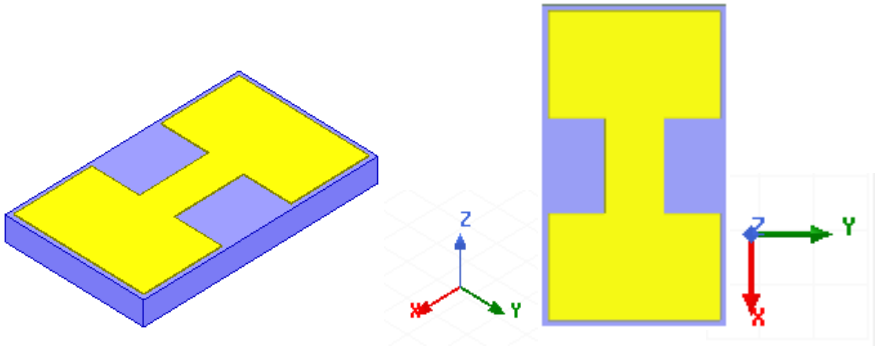

Step 1

Draw a box around the unit cell which shares the dimensions of the unit cell and the position of the ground plane. The only difference is the height of the box, which has an additional height in the Z direction of operating free space wavelength. Therefore the total height of the box is now (31mils+18μm*2+wavelength)

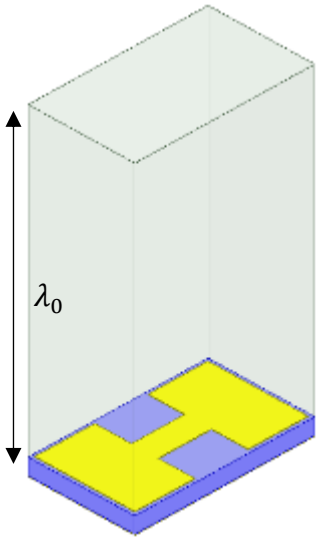

Step 2

Next step is assigning boundary to the box. Select the faces of the box shown right click as assign the faces as Perfect E boundary and Perfect H boundary. Assigning boundaries may vary with respect to the wave that will impinge on the surface.

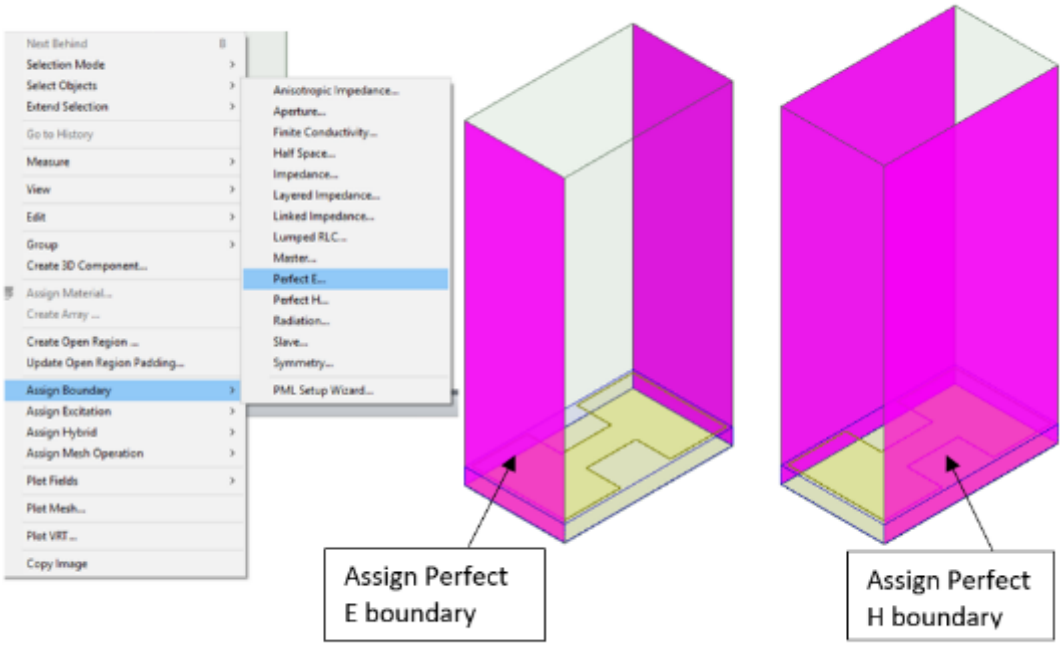

Step 3

Assigning wave port. Select the top face of the air box, right click and the select assign boundaries and then select waveport. As show in the figure, the port will ask you to assign the integration line. This line is drawn in the direction of the E field on the top face of the box shown.

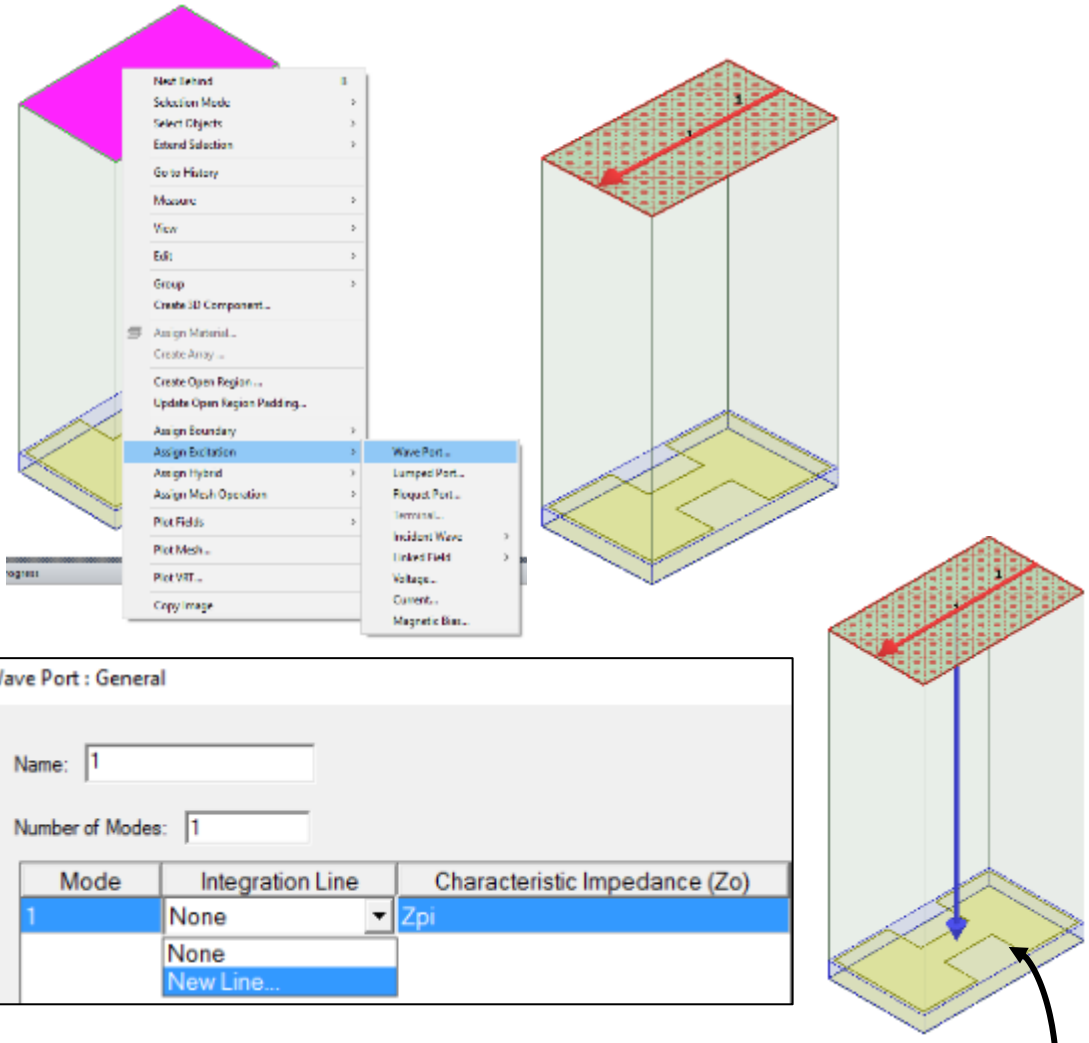

Now click next and in Post Processing, check the Deembed box and assign a distance of the operating free space wavelength. The reason for assigning the height of the box above the stackup as λ_0 is because the wave that will incident on the surface will not be out of phase.